IMPROVEMENTS TO THE COMPUTATIONAL PIPELINE IN CRYSTAL PLASTICITY ESTIMATES OF HIGH CYCLE FATIGUE OF MICROSTRUCTURES

A Thesis
Presented to
The Academic Faculty

by

Paul Calvin Kern

In Partial Fulfillment
of the Requirements for the Degree
Master of Science in the
School of Mechanical Engineering

Georgia Institute of Technology
May 2016

IMPROVEMENTS TO THE COMPUTATIONAL PIPELINE IN CRYSTAL PLASTICITY ESTIMATES OF HIGH CYCLE FATIGUE OF MICROSTRUCTURES

Approved by:

Dr. David L. McDowell, Advisor
School of Mechanical Engineering
Georgia Institute of Technology

Dr. Laurent Capolungo
School of Mechanical Engineering
Georgia Institute of Technology

Dr. Richard W. Neu
School of Mechanical Engineering
Georgia Institute of Technology

Date Approved: April 26, 2016

“Little by little, one travels far.”

-J.R.R. Tolkien

ACKNOWLEDGEMENTS

I would like to thank my advisor, Dr. David L. McDowell, for his impact on my continuing education. This thesis would not be possible without his knowledge and feedback. I would also like to thank the members of my thesis reading committee, Dr. Laurent Capolungo for inspiring me to pursue a greater understanding of material deformation and its impact on engineering design, and Dr. Richard W. Neu for being an excellent teacher and providing feedback on this thesis.

The availability of financial support throughout the duration of my time at Tech has been invaluable in allowing me to continue my work without distraction. I would like to thank Dassault Systèmes for providing funding to begin the work on an automated crystal plasticity pipeline and understanding of fatigue sensitivities. I would also like to thank the Naval Air Systems Command (NAVAIR) for providing funding to research the fatigue properties of Al 7075-T6. Finally, I would like to thank The Boeing Company for providing support via an additional project, which is not included in this work. None of this would be possible without Dr. David L. McDowell's dedication to securing funding throughout my time here, for which I am grateful. In addition, I am thankful for the Carter N. Paden, Jr. Distinguished Chair in Metals Processing, held by Dr. David L. McDowell, for providing additional support in between projects.

I would also like to thank those previous students of the McDowell lab whose work I have adapted or built upon, particularly Dr. Gustavo Castelluccio, Conor Hennessey, Dr. William Musinski, and Dr. Brett Ellis. Much of what I have done would not be possible without the foundation they have built and I greatly appreciate their contributions to the McDowell lab and the scientific community as a whole.

I am particularly indebted to my fellow compatriots in MRDC 3338. Having friendly banter, engaging conversations, and scientific prowess surrounding me on a daily basis made my pursuits more enjoyable and more productive. I would especially like to thank Matthew Priddy for becoming a great friend and mentor for all things related to my time as a graduate student.

Finally, I want to thank my family. Thank you for being my rock and sharing in all the times, good or bad. Thank you for encouraging me to make bold decisions, embrace my passions, and explore new horizons. I am entirely who I am today thanks to your love and patience.

TABLE OF CONTENTS

Acknowledgements iv

List of Tables ix

List of Figures xi

List of Abbreviations and Symbols xvii

Summary xix

Chapter 1: Introduction 1

1.1: Introduction 1

1.2: Fatigue 1

1.2.1: Fatigue Crack Formation 3

1.2.2: Microstructurally Small Crack Growth 5

1.2.3: Damage Parameters 10

1.2.4: Long Crack Growth 15

1.3: Crystal Plasticity 15

1.4: Synthetic Microstructures and Statistical Volume Elements 20

1.5: Thesis Outline 24

Chapter 2: Automated Simulation Pipeline 27

2.1: Motivation 27

2.2: Simulation Modules 28

2.2.1: Microstructure 29

2.2.2: Meshing 31

2.2.3: Simulation 35

2.2.4: Post-Process 38

2.2.5: Pipeline 38

2.3: Material Repositories 40

2.4: Summary of Features and Parameters 41

2.5: Conclusions 45

Chapter 3: Sensitivity Analysis of Fatigue in Crystal plasticity models 46

3.1: High Cycle Fatigue as an Extreme Value Problem 46

3.2: Sensitivity Analysis Procedure 48

3.3: Ti64 Case Study 54

3.4: IN100 Case Study 63

3.5: Conclusions 66

Chapter 4: Mesh Insensitive Method for Applying Extreme Value Fatigue Life Estimates 68

4.1: Convergence of FIP Distribution 68

4.2: Tail Behavior of FIP Distributions 76

4.3: Proposed Mesh Insensitive Fatigue Comparison 86

4.4: Comparison of Fatigue Performance for Textured Ti64 88

4.5: Conclusions 93

Chapter 5: Point Propagation Fatigue Model 95

5.1: Introduction 95

5.2: Crack Formation: Incubation and Nucleation 99

5.3: Crack Propagation 107

5.4: Conclusions 121

Chapter 6: Microstructurally Small Fatigue Crack Growth Modeling in AL 7075-T6 122

6.1: Synthetic Microstructure Representation 122

6.2: FIP Intensification under Varied Load Conditions Due to Stringer Distribution 123

6.3: Fatigue Calibration 128
6.4: Fatigue Life Sensitivities 131
6.5: Stage II Propagation Analysis 137
6.6: Multiaxial Fatigue: Gamma Plane Case Study 142
6.7: Conclusions 151
Chapter 7: Conclusions and Directions for Future Research 153
7.1: Summary 153
7.2: Directions for Future Research 155
APPENDIX A 159
APPENDIX B 162
APPENDIX C 166
REFERENCES 168

LIST OF TABLES

Page

Table 1. KS test statistics for “nominally same” and “uniquely generated” microstructure batches compared to the highest fidelity reconstruction (Configuration 9). 51

Table 2. List of configurations for the Ti64 sensitivity DOE. 55

Table 3. Number of grains observed in nominally same and uniquely generated microstructures. 60

Table 4. List of configurations for the IN100 sensitivity DOE. 64

Table 5. List of configurations for the Al 7075-T6 FIP comparison. 84

Table 6. Crack propagation metrics in crystal plasticity, crystal plasticity with elastic padding, and a smaller crystal plasticity volume for two crack sizes. Cracks modeled with the elastic stiffness degradation method. 136

Table 7. Ti64 responses for nine configurations at $\boldsymbol{\varepsilon a = 0.35 \varepsilon y}$. 162

Table 8. Ti64 responses for nine configurations at $\boldsymbol{\varepsilon a = 0.35 \varepsilon y}$ cont. 162

Table 9. Ti64 responses for nine configurations at $\boldsymbol{\varepsilon a = 0.7 \varepsilon y}$. 163

Table 10. Ti64 responses for nine configurations at $\boldsymbol{\varepsilon a = 0.7 \varepsilon y}$ cont. 163

Table 11. IN100 responses for nine configurations at $\boldsymbol{\varepsilon a = 0.35 \varepsilon y}$. 164

Table 12. IN100 responses for nine configurations at $\boldsymbol{\varepsilon a = 0.35 \varepsilon y}$ cont. 164

Table 13. IN100 responses for nine configurations at $\boldsymbol{\varepsilon a = 0.7 \varepsilon y}$ 165

Table 14. IN100 responses for nine configurations at $\boldsymbol{\varepsilon a = 0.7 \varepsilon y}$ cont. 165

Table 15. Gamma distribution fits to 99.9% FIP tails for nine configurations of Ti64 at $\boldsymbol{\varepsilon a = 0.35 \varepsilon y}$. 166

Table 16. Gamma distribution fits to 99.9% FIP tails for nine configurations of Ti64 at $\boldsymbol{\varepsilon a = 0.7 \varepsilon y}$ 166

Table 17. Gamma distribution fits to 99.9% FIP tails for nine configurations of IN100 at $\boldsymbol{\varepsilon a = 0.35 \varepsilon y}$ 167

Table 18. Gamma distribution fits to 99.9% FIP tails for nine configurations of IN100 at $\boldsymbol{\varepsilon a = 0.7 \varepsilon y}$. 167

Table 19. Gamma distribution fits to 99.9% FIP tails for four textures of Ti64 at $\boldsymbol{\varepsilon a = 0.75 \varepsilon y}$..... 167

LIST OF FIGURES

Page

Figure 1. Microstructurally small (left) and short (right) cracks [5]..... 3

Figure 2. Cracked constituent particle (left) and corrosion pit (right) as crack formation sites in Al 7075-T6 [12]. 4

Figure 3. Fluctuations of crack growth rate in Al 2024-T3 (b) as a function of the surface crack position (a) as reproduced from [17]. 6

Figure 4. X-ray microtomography imaged crack surface (green) in Al 2024, with grain boundaries (gold) decorated using Ga [22]. 7

Figure 5. Surface crack growth as observed and predicted by Künkler et al. [20]. 8

Figure 6. Geometric representations of Stage I, Stage I extended, and Stage II crack growth contributions from two active slip systems adapted from [23]. 9

Figure 7. Nucleation microstructure and damage parameter averaging area as employed by Hochhalter et al. [44]..... 12

Figure 8. Mesh with highlighted slip band utilized by Castelluccio and McDowell [46] to obtain $\boldsymbol{\Delta CTD}$ to FIP relationships for a Cu single crystal. 14

Figure 9. Multiplicative decomposition of the elastic-plastic deformation gradient adapted from [64]..... 17

Figure 10. Two point spatial statistic for the cross-correlation of a two-phase microstructure function. 22

Figure 11. Overview of the Automated Simulation Pipeline modules and organization..... 29

Figure 12. 2D cross-sections of the 3D voxelated representation of a synthetic microstructure (left) and subsampled representation (right). 31

Figure 13. 2D cross section of a 3D voxelated, masked FEM mesh. 32

Figure 14. Overlay of microstructure (left) on unstructured mesh (right) as viewed from the z-axis. 33

Figure 15. Example banded mesh. Different colors indicate different layers for a single crystallographic plane. Grain boundaries may be observed where a transition in the plane orientation occurs. 34

Figure 16. Loading steps and parameters for pipeline execution. 36

Figure 17. Node sets used for applying loads and boundary conditions. 37

Figure 18. Example material repository structure with required files. 40

Figure 19. FIPs averaged over grain equivalent volumes for two representations of the same nominal microstructure. 53

Figure 20. Example meshes for nine configurations of Ti64 sensitivity DOE. 56

Figure 21. Behavior of $\boldsymbol{\mu kernel}$ from Ti64 simulations at $\boldsymbol{\varepsilon a = 0.35\varepsilon y}$. 57

Figure 22. Behavior of $\boldsymbol{\mu kernel}$ from Ti64 simulations at $\boldsymbol{\varepsilon a = 0.7\varepsilon y}$. 58

Figure 23. Behavior of $\boldsymbol{\sigma kernel}$ from Ti64 simulations at $\boldsymbol{\varepsilon a = 0.35\varepsilon y}$. 59

Figure 24. Behavior of $\boldsymbol{\mu grain}$ from Ti64 simulations at $\boldsymbol{\varepsilon a = 0.35\varepsilon y}$..... 59

Figure 25. Behavior of adjusted $\boldsymbol{\mu kernel}$ with target size of 1000 grains. Samples from nominally same Ti64 microstructures at $\boldsymbol{\varepsilon a = 0.35\varepsilon y}$..... 61

Figure 26. Behavior of adjusted $\boldsymbol{\mu kernel}$ with target size of 1000 grains. Samples from uniquely generated Ti64 microstructures at $\boldsymbol{\varepsilon a = 0.35\varepsilon y}$. 61

Figure 27. Behavior of adjusted $\boldsymbol{\mu kernel}$ with target size of 200 grains. Samples from uniquely generated Ti64 microstructures at $\boldsymbol{\varepsilon a = 0.35\varepsilon y}$. 62

Figure 28. Behavior of adjusted $\boldsymbol{c\mu kernel}$ with target size of 200 grains. Samples from uniquely generated Ti64 microstructures at $\boldsymbol{\varepsilon a = 0.35\varepsilon y}$. 63

Figure 29. Behavior of $\boldsymbol{\mu kernel}$ from IN100 simulations at $\boldsymbol{\varepsilon a = 0.35\varepsilon y}$. 65

Figure 30. Behavior of $\boldsymbol{\mu kernel}$ from IN100 simulations at $\boldsymbol{\varepsilon a = 0.7\varepsilon y}$..... 65

Figure 31. Example pole figures for the (from left to right) Basal, Transverse, Random and Actual textures utilized in this work [113]. Note that pole figure axes are labelled according to SVE axes for comparison to applied loading. 70

Figure 32. FIP distributions for 9 configurations of the same nominal microstructures of randomly textured Ti64 at $\boldsymbol{\varepsilon a = 0.35\varepsilon y}$..... 71

Figure 33. 99.9% tail of the FIP distributions for 9 configurations of the same nominal microstructures of randomly textured Ti64 at $\boldsymbol{\varepsilon a = 0.35\varepsilon y}$. 72

Figure 34. FIP distributions for 9 configurations of the same nominal microstructures of randomly textured Ti64 at $\boldsymbol{\varepsilon a = 0.7\varepsilon y}$. 72

Figure 35. 99.9% tail of the FIP distributions for 9 configurations of the same nominal microstructures of randomly textured Ti64 at $\boldsymbol{\varepsilon a = 0.7\varepsilon y}$. 73

Figure 36. FIP distributions for four textures of Ti64 with y-axis tension/compression at $\boldsymbol{\varepsilon a = 0.75\varepsilon y}$. 74

Figure 37. Convergence of FIP distributions for 12^3 15 μm (top) and 10^3 50 μm element (bottom) meshes of randomly oriented Ti64 grains as compared to 40 SVE of 49^3 8.5 μm elements. 75

Figure 38. Gamma distribution fits for 9 configurations of the same nominal microstructures of randomly textured Ti64 at $\boldsymbol{\varepsilon a = 0.35\varepsilon y}$..... 77

Figure 39. Gamma distribution fits for 9 configurations of the same nominal microstructures of randomly textured Ti64 at $\boldsymbol{\varepsilon a = 0.7\varepsilon y}$. 78

Figure 40. Gamma distribution fits for 9 configurations of the same nominal microstructures of randomly textured IN100 at $\boldsymbol{\varepsilon a = 0.35\varepsilon y}$. 78

Figure 41. Gamma distribution fits for 9 configurations of the same nominal microstructures of randomly textured IN100 at $\boldsymbol{\varepsilon a = 0.7\varepsilon y}$. 79

Figure 42. Gamma distribution fits for FIP tails of four textures of Ti64 under $\boldsymbol{\varepsilon a = 0.7\varepsilon y}$ x-axis strain. 79

Figure 43. Gamma distribution fits for 100 SVE of Small Configuration 1 and Small Configuration 2 randomly textured Ti64 at $\boldsymbol{\varepsilon a = 0.35\varepsilon y}$. 80

Figure 44. Comparison of empirical CDF of 20 SVE at Configuration 9 (blue) and the combined empirical CDF of 100 Small Configuration 2 (red) randomly textured Ti64 at $\boldsymbol{\varepsilon a = 0.35\varepsilon y}$. 82

Figure 45. 99.9% tail of the Gaussian averaged FIP distributions for 9 configurations of the same nominal microstructures of randomly textured Ti64 at $\boldsymbol{\varepsilon a = 0.35\varepsilon y}$. 83

Figure 46. 99.9% tail of the cube averaged FIP distributions for 9 configurations of the same nominal microstructures of randomly textured Ti64 at $\boldsymbol{\varepsilon a = 0.35\varepsilon y}$. 83

Figure 47. 99.9% tail of the element FIP distributions for 3 configurations of Al 7075-T6 at $\boldsymbol{\varepsilon a = 0.7\varepsilon y}$ in the RD. 84

Figure 48. 99.9% tail of the element FIP distributions for 3 configurations of Al 7075-T6 at $\boldsymbol{\gamma a = 0.7\varepsilon y}$ in the RD-ND plane. 85

Figure 49. Comparison of extreme value distributions from 100 SVE in each of x (a) y (b) and z-axis (c) loading conditions of basal, transverse, random and actual textures using the SVE maximum FIP. 89

Figure 50. FIP distributions for 100 SVE of transverse texture Ti64 in x-axis tension/compression. 90

Figure 51. Comparison of extreme value distributions from 100 SVE in each of x (a) y (b) and z-axis (c) loading conditions of basal, transverse, random and actual textures using Monte-Carlo sampled values from the empirical CDF. 91

Figure 52. Final calibration of mesoscale crack propagation method as applied to uniaxial (left) and shear (right) loadings compared to experimental data from [80]. 97

Figure 53. Particle distribution in "stringers" along rolling direction from [122]. 100

Figure 54. Nucleation calibration mesh with fractured particle. 101

Figure 55. Calibration of estimated nucleation lives to parameter $\boldsymbol{D3}$. 104

Figure 56. Nucleation parameter fields around the cracked particle for uniaxial loading of 0° crack (a) shear loading of 0° crack (b) uniaxial loading of 45° crack (c) and shear loading of 45° crack (d). 105

Figure 57. Damage parameters as a function of crack inclination angle for applied shear (a) and uniaxial (b) load conditions. 106

Figure 58. 2D illustration of the point propagation method with initial distribution of points (left) and at a later time (right) with the previously occupied element (black) now being damaged. 108

Figure 59. Crack propagation direction p selection from local crack plane normal n_{int} using local coordinate system r, $d\theta$, n_c. Crack plane normal determined by Stage I or Stage II approach. 110

Figure 60. Point propagation pseudocode for crack extension during simulation. 110

Figure 61. Flowchart of crack propagation simulation information exchange between Python and Abaqus UEXTERNALDB [48]. 112

Figure 62. Poorly defined crack propagation paths created by the mesoscale propagation algorithm. 114

Figure 63. Two possible intermediate crack planes using the weighted normal method caused by the indeterminate direction of the individual crack plane normals. .. 118

Figure 64. Simulated crack using Stage II point based propagation at 0.4% strain amplitude tension-compression $\boldsymbol{R\varepsilon = -1}$ in the y-axis. Color-coding indicates iso-life contours. 119

Figure 65. Simulated crack using Stage II point based propagation at 0.4% strain amplitude in XY-shear with $\boldsymbol{R\varepsilon = -1}$. Color-coding indicates iso-life contours..... 120

Figure 66. $\boldsymbol{\sigma 22}$ response during crack propagation simulation. Displacements exaggerated to highlight the highly distorted crack elements..... 120

Figure 67. Sample rolled microstructure and associated target pole figure..... 122

Figure 68. Validation of the particle stringer reconstruction using 2-point statistics. Note that confidence bounds capture the majority of the sampled microstructure scans from varied sources [11, 87]. First neighbor effects are well captured in the 74-124 region. 124

Figure 69. Relative errors of MKS prediction compared to crystal plasticity simulation of $\boldsymbol{\varepsilon 22}$ (loading direction) for each element in five validation microstructures of size 21x21x21. 126

Figure 70. FS FIP intensification near particle stringers under uniaxial loading of 0.2%. 127

Figure 71. FS FIP intensification near particle stringers under shear loading of 0.4%. 127

Figure 72. Comparison of uniaxial fatigue lives as predicted from simulation and observed by Zhao and Jiang [80]. 130

Figure 73. Comparison of shear fatigue lives as predicted from simulation and observed by Zhao and Jiang [80]. 130

Figure 74. Relative difference in $\boldsymbol{D3}$ for five random orientations and nine calibration load conditions. 132

Figure 75. Relative difference in total predicted fatigue lives for five random orientations and nine calibration load conditions. 134

Figure 76. Crack propagation sensitivity to mesh resolution for five microstructures. 135

Figure 77. Crack propagation sensitivity to choice of mesoscale propagation distance. 136

Figure 78. Comparison of crack propagation values ($\boldsymbol{FIPp = 1}$) between partially elastic and full crystal plasticity simulations for varying loads. 137

Figure 79. Slip plane ratios for three microstructures under $\boldsymbol{\varepsilon a = 0.2\%}$ and $\boldsymbol{R\varepsilon = -1}$ tension/compression. 138

Figure 80. Slip plane ratios for three microstructures under $\boldsymbol{\varepsilon a = 0.5\%}$ and $\boldsymbol{R\varepsilon = -1}$ tension/compression. 139

Figure 81. Slip plane ratios for three microstructures under $\boldsymbol{\varepsilon a = 0.8\%}$ and $\boldsymbol{R\varepsilon = -1}$ tension/compression. 139

Figure 82. Slip plane ratios for three microstructures under $\boldsymbol{\gamma a = 0.4\%}$ and $\boldsymbol{R\varepsilon = -1}$ simple shear. 139

Figure 83. Slip plane ratios for three microstructures under $\boldsymbol{\gamma a = 0.6\%}$ and $\boldsymbol{R\varepsilon = -1}$ simple shear. 140

Figure 84. Slip plane ratios for three microstructures under $\boldsymbol{\gamma a = 0.8\%}$ and $\boldsymbol{R\varepsilon = -1}$ simple shear. 140

Figure 85. Crack propagation comparison using two (left) and four (right) active slip planes under $\boldsymbol{\varepsilon a = 0.4\%}$ and $\boldsymbol{R\varepsilon = -1}$ tension/compression in the y-axis. 141

Figure 86. Crack propagation comparison using two maximally active slip systems (left) and two maximally active slip planes (right) under $\boldsymbol{\varepsilon a = 0.4\%}$ and $\boldsymbol{R\varepsilon = -1}$ tension/compression in the y-axis. 142

Figure 87. Planes of maximum shear and crack growth directions from bulk strains [34]. 143

Figure 88. Comparison of true variability and condensed variability for the construction of a fatigue response surface. 145

Figure 89. Γ-plane for 7075-T6 Al depicting iso-life contours based on response surface fitting to previously calibrated model. Squares are sampled loadings for Case A, points are the sampled loadings for the Case B. The unlabeled portion of the same color contour is the Case A branch. 147

Figure 90. Nucleation mesh (left) constructed by subsampling the propagation microstructure (right) and inserting a cracked particle. Grain 50 is highlighted in both meshes along with the particle in the nucleation mesh. 149

Figure 91. Γ-plane for 7075-T6 Al depicting iso-life contours based on response surface fitting to currently calibrated model. Squares are sampled loadings for Case A, points are the sampled loadings for the Case B. The unlabeled portion of the same color contour is the Case A branch. 151

LIST OF ABBREVIATIONS AND SYMBOLS

CDF	Cumulative Distribution Function
DOE	Design of Experiments
EPFM	Elastic Plastic Fracture Mechanics
FCC	Face-Centered Cubic
FEM	Finite Element Method
FIP	Fatigue Indicator Parameter
FIP^{α}	Fatigue Indicator Parameter on slip system α
FIP_0	Fatigue Indicator Parameter prior to cracking grain
HCF	High Cycle Fatigue
HCP	Hexagonal Close-Packed
ISV	Internal State Variable
LCF	Low Cycle Fatigue
LEFM	Linear Elastic Fracture Mechanics
MSC	Microstructurally Small Crack
OW	Ohno and Wang
PDF	Probability Density Function
PSB	Persistent Slip Band
PSC	Physically Small Crack
UEXTERNALDB	User EXTERNAL DataBase subroutine
UMAT	User MATerial subroutine

$\mathbf{\Delta CTD}$	Cyclic crack tip displacement
$\mathbf{\Delta K}$	Range of stress intensity factor
$\mathbf{\Delta J}$	Range of J-Integral
$\boldsymbol{d}$	Scalar damage parameter
$\mathbf{F}$	Deformation gradient
$\mathbf{F}^e$	Elastic deformation gradient
$\mathbf{F}^p$	Plastic deformation gradient
$\dot{\boldsymbol{\gamma}}^{\boldsymbol{\alpha}}$	Shear strain rate of slip system α
$\boldsymbol{k}$	Fatemi-Socie constant
$\mathbf{L}$	Velocity gradient in current configuration
$\mathbf{L}^e$	Elastic-damaged velocity gradient in current configuration
$\mathbf{L}^p$	Plastic velocity gradient in current configuration
$\boldsymbol{m}^{\boldsymbol{\alpha}}$	Slip plane normal of slip system α
$\boldsymbol{m}_{\boldsymbol{0}}^{\boldsymbol{\alpha}}$	Slip plane normal of slip system α in intermediate configuration
$\boldsymbol{N}$	Total fatigue life
$\boldsymbol{N_{inc}}$	Number of cycles to crack the particle leading to dominant fatigue crack
$\boldsymbol{N_{nuc}}$	Number of cycles to create a crack within the matrix adjacent to incubated particle
$\boldsymbol{N_{MSC}}$	Microstructurally small crack life
$\boldsymbol{N_{PSC}}$	Physically small crack life
$\boldsymbol{N_{LC}}$	Long crack life
$\boldsymbol{s}^{\boldsymbol{\alpha}}$	Slip direction vector of slip system α
$\boldsymbol{s}_{\boldsymbol{0}}^{\boldsymbol{\alpha}}$	Slip direction vector of slip system α in intermediate configuration
$\mathbf{T}$	Second Piola-Kirchhoff stress tensor in intermediate configuration

SUMMARY

The objective of this work is to provide various improvements to the modeling and uncertainty quantification of fatigue lives of materials as understood via simulation of crystal plasticity models applied to synthetic microstructure instantiations. Given the broad scope of this thesis and the nature of scientific advances, this work builds on the work of many previous students. Calibrated material models developed by Musinski, Smith, and Hennessey for IN100, Ti64, and Al 7075-T6 were repeatedly used for many development and exploratory stages. Fatigue indicator parameter responses were characterized for several material models, morphologies, and loading conditions. Crack propagation methods from Castelluccio and Musinski were combined with improved geometric basis to better study stress redistribution effects and crack propagation through multiple grains while retaining a mesoscale level of computational efficiency. A model was implemented to describe crack nucleation behavior in Al 7075-T6 using a crack simulation strategy and fractured constituent particles. Fatigue lives were then simulated for various multi-axial stress states, with noteworthy differences between the fatigue model presented in this thesis, and the earlier work of Hennessey. These differences are presented in the Gamma Plane construct of Brown and Miller.

The major contributions of this work are the computational frameworks developed for continued advances in the field of crystal plasticity and fatigue, the reformulation and application of a fatigue crack growth model for Al 7075-T6, and the generalization of the crack propagation and information exchange required for crack propagation simulations in crystal plasticity models. These methods as well as the software developed and released will facilitate more rapid advancements in the field of crystal plasticity models, especially as applied to high cycle fatigue.

CHAPTER 1: INTRODUCTION

1.1: Introduction

The past decade has seen large advances in computational techniques, especially those concerning the prediction of the fatigue lives of various metal alloys under complex loadings. With an improvement in ability to represent physical processes of damage in metals, particular import should be placed on the increased pace and understanding with which data can be generated and analyzed for these specialized models. This work presents several fundamental improvements to a material model, demonstrates new techniques of analyzing statistical information related to metal fatigue, and discusses an improved computational framework to increase the pace of development for new material research directions. This work first begins with a summary of fatigue research and crystal plasticity modeling approaches since both are utilized throughout the text. Particular attention is paid to those mechanisms that are relevant to material system models incorporated into this work.

1.2: Fatigue

To understand material models of fatigue, their development, and applications, it is important to first understand the mechanical processes that drive fatigue failure of metals. Fatigue is the form of material failure caused by repeated application of cyclic loadings. The fatigue life of a component expresses the number of loading cycles N required to cause failure of a component based on the application of some design criteria. Accurate prediction of component lives can lead to significant savings, both monetarily and in the form of human lives saved by the prevention of catastrophic failures. Fatigue failures have been estimated by Reed et al. [1] to cost as much as 4% of the U.S. economy. One particular industry that sees the application of advanced materials in

situations where design for fatigue is of the utmost importance is the aerospace industry. Failure of components can have catastrophic consequences and because of the importance of weight, large gains can be realized if components are operated closer to yield, thus lowering the expected fatigue lives. The aerospace industry has seen the development of many exotic materials for structural and propulsion related components.

Initial research and useful methods in fatigue design focused primarily on phenomenological models informed by macroscale properties and loading conditions. One of the first successful characterizations of the fatigue life of materials is the stress-life approach pioneered by Wöhler [2] and refined by Basquin [3]. This approach is still used to estimate fatigue lives in many applications.

Deterministic relationships of macroscopic parameters have often been found to not be entirely sufficient to describe material behavior, however. Indeed, since fatigue lives can be observed over a very large range (multiple orders of magnitude) depending on the applied loadings, there are several stages of crack growth with various competing mechanisms that must occur before ultimate failure occurs. These stages are typically divided as follows: crack formation, microstructurally small crack growth (MSC), physically small crack growth (PSC), and mechanically long crack growth (MLC) which together constitute the total life of that specimen. These stages are typified by the size, expressed in terms of a multiple of microstructural features, over which similar crack propagation models may be applied. While the transitions between the various crack stages are relatively ambiguous, crack formation is typically considered over the first grain or cracked inclusion, MSC is generally considered to extend from 3-10 grain barriers, PSC up to 0.5-1 mm, and MLC for the remainder of the part life [4]. Furthermore, microstructurally small cracks are distinct from microstructurally short cracks in that the former requires all crack dimensions to be less than some threshold size, while the latter is accepted if only one crack dimension meets this criterion. This

work will only consider microstructurally small cracks and not treat the somewhat distinct problem of microstructurally small cracks.

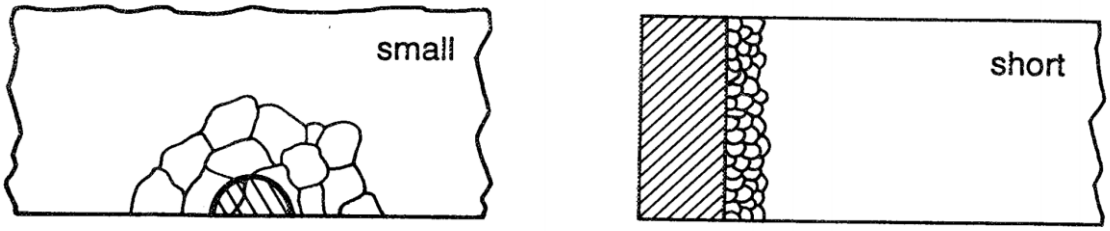

Figure 1. Microstructurally small (left) and short (right) cracks [5].

The total life may be expressed mathematically as the summation of the number of cycles to cause fatigue failure N_{total} appears as follows

$$N_{total} = N_{FOR} + N_{MSC} + N_{PSC} + N_{LC} \quad (1)$$

where N_{FOR} is the number of cycles to crack incubation, N_{MSC} is the number of cycles spent in microstructurally small crack growth, N_{PSC} is the number of cycles spent in physically short crack growth, and finally N_{LC} is the number of cycles spent in long crack growth. It is the final regime that is best understood and represented well by phenomenological models such as the Paris law.

1.2.1: Fatigue Crack Formation

Prior to crack propagation, however, a fatigue crack must form within the material. This process often occurs near geometric and microstructural stress concentrations. Fatigue crack formation can have several different mechanisms depending upon the material system of interest. Indeed, several competing mechanisms may arise in the same material system. The aluminum alloy 7075-T6, for instance, has a relatively high volume fraction of constituent particles whose debonding and fracture behavior can provide significant stress raisers for crack propagation into the metallic matrix. While Xue et al. [6] and Weiland et al. [7] observed particle debonding in this material, crack propagation did not occur from these sites. Thus, constituent particle

cracking is the primary crack formation site for Al 7075-T6. This effect is typically observed in ambient environments, with corrosive environments generally providing more optimal crack formation sites in the form of pits. For ambient environments, cracked particles provide nearly exclusive crack formation sites as reported by many researchers [6-9]. The composition of such cracked particles is generally observed as being Fe-rich such as Al_7Cu_2Fe. Multiple researchers have observed the population of these particles during loading with particular attention paid to differentiating factors in the cracked and uncracked populations. These observations indicate a significant correlation of cracking probability to particle size [10, 11]. This has been surmised by Bozek et al. [10] to be caused by the higher probability of inherent flaws in larger particles. These flaws lead to stress concentrations and cracking of the brittle constituent particles. Cracking of these constituent particles is often directly observed or assumed to occur during the first application of load [6, 9, 10].

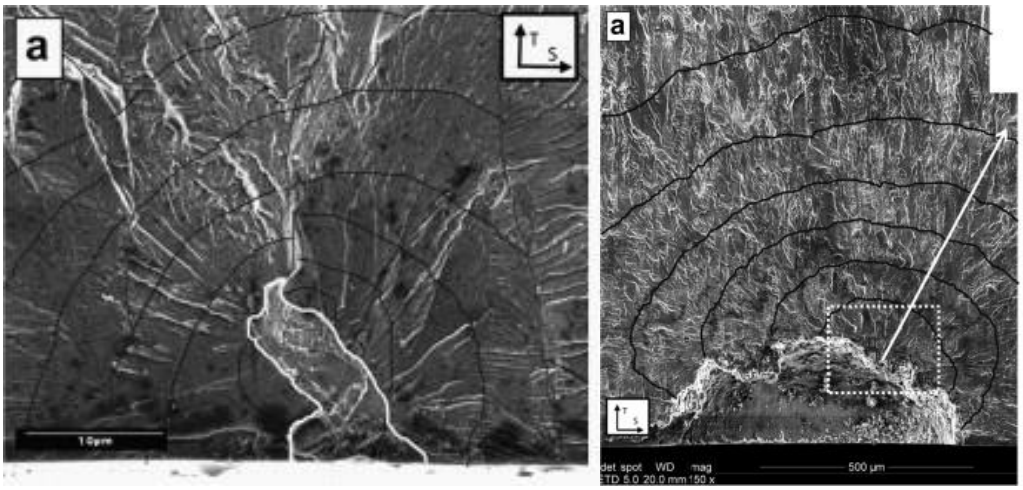

Figure 2. Cracked constituent particle (left) and corrosion pit (right) as crack formation sites in Al 7075-T6 [12].

Localization factors such as grain orientation, neighbor disorientation, and inclusions can also contribute to cyclic plasticity and the formation of persistent slip band (PSB) structures. This can provide a competing mechanism for crack formation in alloys

with significant impurities like Al 7075-T6 or be the primary crack formation mechanism for purer alloys such as those used in turbine applications. For example, Li et al. [13] corroborated earlier observations of crack formation exclusively at inclusions for low temperatures, but demonstrated that at elevated temperatures, the formation of PSB also provided crack formation sites in Al 7075-T6. In all metals, surface features can also contribute significantly to the overall fatigue life and scatter. PSB interaction with the free surface can create sharp extrusions and intrusions, which are crack precursors. In addition, residual stress effects, geometric stress concentrations, and inclusion density can drive fatigue crack formation near the surface [14]. Cyclic plastic strain can also induce subsurface fatigue crack formation. Intragranular PSB can form due to impingement of slip at grain boundaries and can contribute to fatigue crack formation and early growth.

1.2.2: Microstructurally Small Crack Growth

Microstructurally small cracks are defined by all crack dimensions being less than a threshold size based on microstructural features [5]. The crack and crack tip plastic zone can similarly be contained within a single grain or extend into a small number of grains. This contributes to microstructural features such as grain anisotropy and limited available slip systems near the crack front, producing large variations in crack growth rate. In addition to being highly variable, fatigue crack growth rates can greatly exceed predicted values using long crack formulations due to under predicting the crack tip field intensity [15].

Crack tip interaction with grain boundaries has been observed to induce significant retardation of surface crack growth rate. Many researchers have attributed this effect to grain boundary disorientation. More recently, observations using marker band growth e.g. by Burns et al., as well as other techniques, have allowed the measurement of

internal crack growth rates [12, 16]. These observations indicate that microstructural features may not impede crack growth as strongly as previously thought [12].

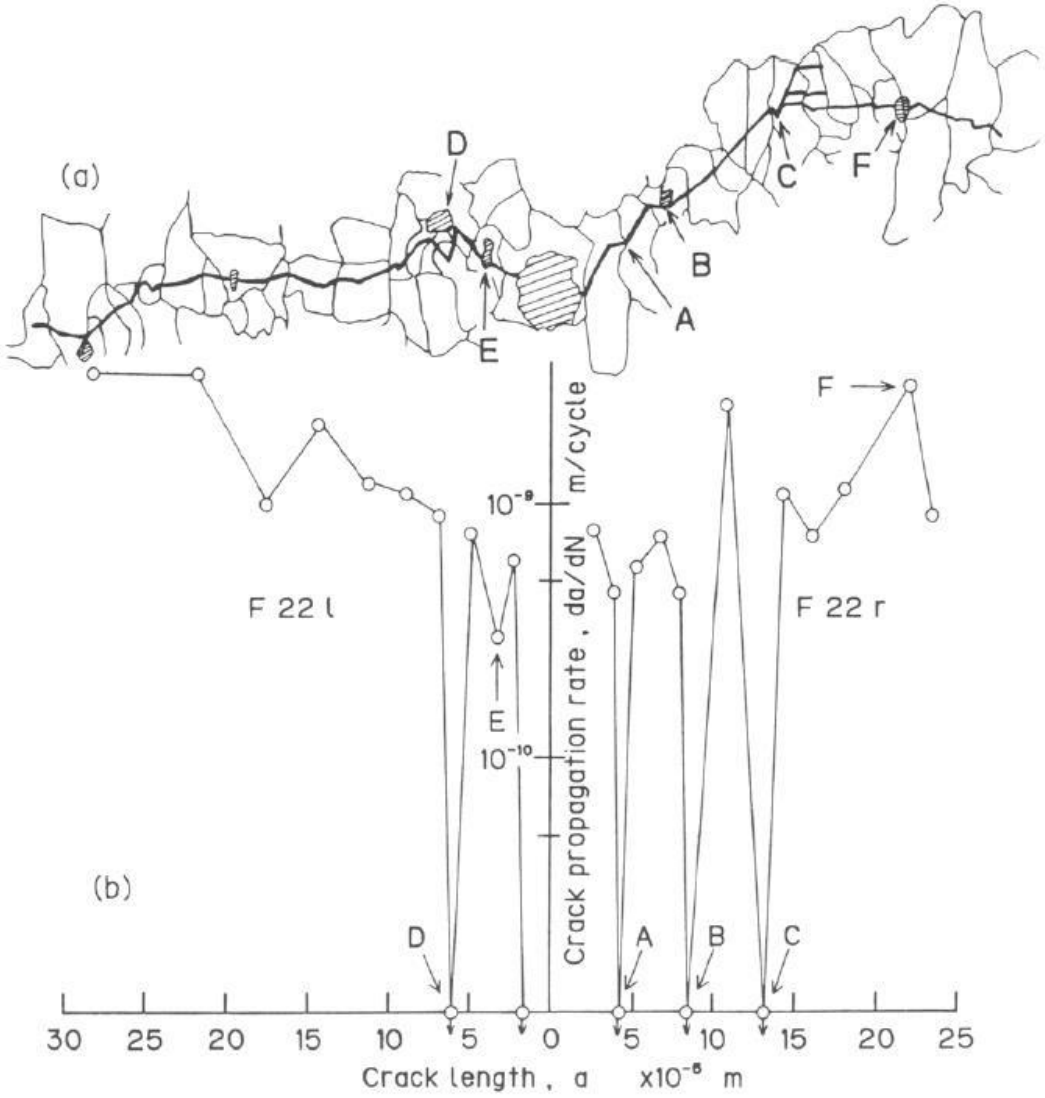

Figure 3. Fluctuations of crack growth rate in Al 2024-T3 (b) as a function of the surface crack position (a) as reproduced from [17].

The process of MSC can be further subdivided into the shear-dominated regime of Stage I, where cracks tend to propagate along individual slip planes, and thus are highly dependent on crystallographic orientation, and the later Stage II process, which tends to occur along maximum principal stress planes and across multiple slip systems. The

transition between these mechanisms is not significantly understood with some materials exhibiting almost no Stage I behavior [18, 19]. Recent efforts by Künkler et al. [20] and others have demonstrated the activation of additional slip systems near the crack tip as load or crack length increase. These models have been demonstrated to have good agreement with experimental surface crack growth for 2D applications, however, the application of such models remains relatively limited in 3D. Johnston [21] applied a three dimensional model of crack propagation using a nodal release and element contact approach to determine crack propagation behavior in Al 7075-T651 single crystals. Significant differences in crack plane orientation were observed between plane strain and plane stress loadings and between single crystals of different orientation.

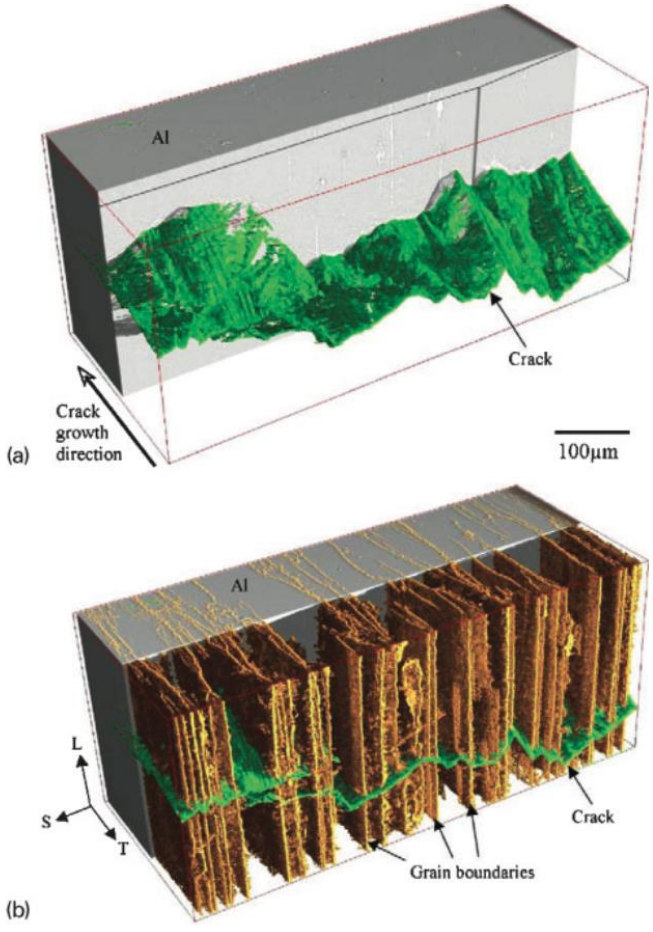

Figure 4. X-ray microtomography imaged crack surface (green) in Al 2024, with grain boundaries (gold) decorated using Ga [22].

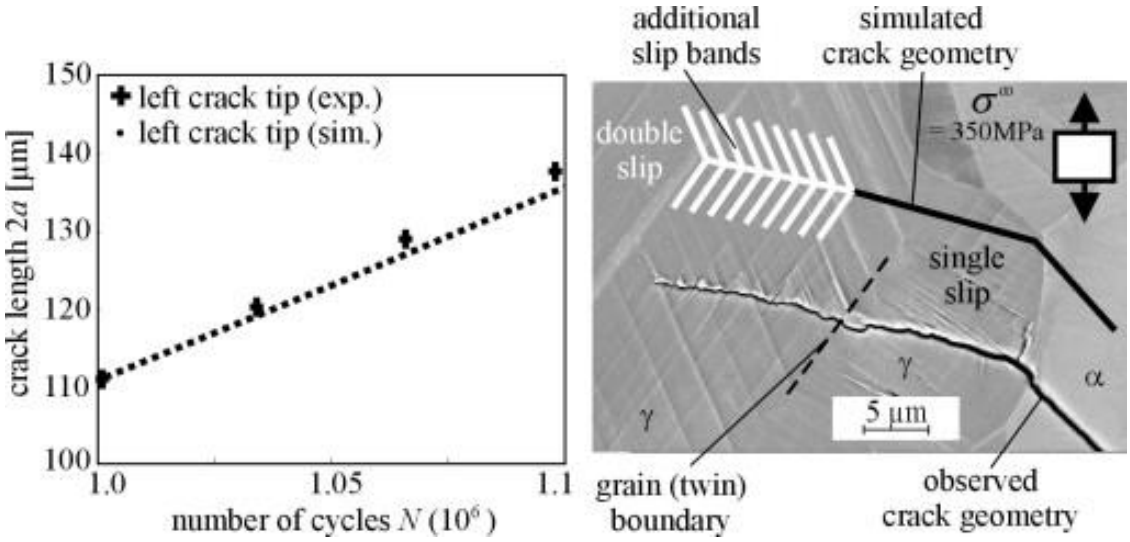

Figure 5. Surface crack growth as observed and predicted by Künkler et al. [20].

Li [23] proposed an extension of the traditional two stage propagation model with additional geometric consideration. This improvement mirrors experimental observation of Neumann [24, 25] in single crystals. Li proposes that Stage II is still a shear dominated process, with alternating crack advances along crystallographic planes of relatively equal Schmid factors. The total crack tip displacement vector $\overline{\Delta \mathrm{CTD}}$ is a summation of the contribution of the individual slip plane sliding displacements $\overline{\Delta \mathrm{CTSD}}$. Li [23] also provides a description for an intermediate Stage I extended crack growth period during which significantly unequal contributions from a primary and secondary slip system sliding displacements sum to the total crack tip displacement.

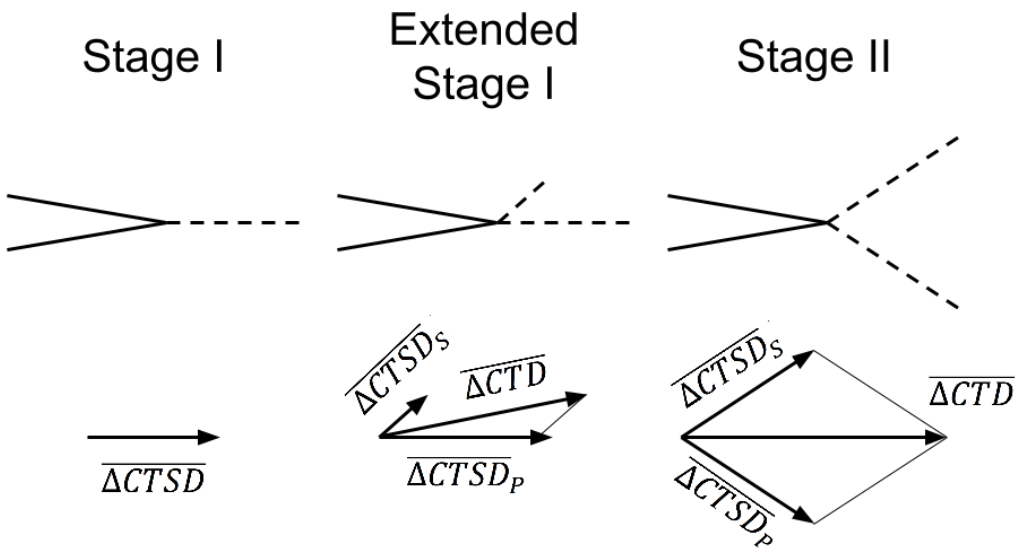

Figure 6. Geometric representations of Stage I, Stage I extended, and Stage II crack growth contributions from two active slip systems adapted from [23].

In addition to characterization of crack growth by relative growth planes, the total life of the part may be characterized by the number of cycles to failure. Common regimes include low cycle fatigue (LCF), typically less than 10^4 cycles; high cycle fatigue (HCF), typically taken as 10^4-10^8 cycles; and very high cycle fatigue (VHCF). Mostly studied using ultrasonic application of loading cycles, this regime can extend past traditional ideas of a threshold stress and produce fatigue lives on the order of 10^9 number of cycles [26]. Low cycle fatigue can generally be well expressed by macro-scale plasticity using a Coffin-Manson [27, 28] relationship for the plastic strain range $\Delta\varepsilon_p$ is the plastic strain range, ε_f' is the fatigue ductility constant, and c is the material fatigue exponent.

$$\frac{\Delta\varepsilon_p}{2} = \varepsilon_f' \left(N\right)^c \tag{2}$$

Since MSC and crack formation can consume ~90% [29, 30] of fatigue life in HCF, modelling of MSC (and thus local microstructure) is imperative to predict life scatter typically observed at the specimen level. Chan et al. [31] calculated path dependent ΔJ-integrals from stereoimaged CTD fields. These integrals exceeded far-field

estimates, an effect observed by Lankford [8] and Akiniwa [17] in the form of higher crack growth rates than those extrapolated from long crack growth data. Chan et al. [31] suggested a ΔCTD based correlation to crack growth rate as a more fundamental parameter for MSC. The crack tip displacement has also been proposed as an analogous driving force metric to the ΔJ-integral [32].

1.2.3: Damage Parameters

Various modeling efforts have been made to introduce parameters that describe processes involved in fatigue crack formation and MSC. Multiaxial loading conditions coupled with varying load ratios are beyond the predictive capabilities of traditional stress and strain metrics for fatigue lives [33]. Many recent, successful models incorporate the consideration of a critical plane on which fatigue damage is concentrated. Brown and Miller [34] determined that the plane of maximum shear strain range $\Delta\gamma_{max}$ best represented the crack propagation process. Initially, this criteria was expressed as an iso-life function of the strain range normal to maximal shear plane $\Delta\varepsilon_n$. This term provides the physical basis for increased dislocation emission and crack propagation rates with higher imposed normal displacements.

$$\Delta\gamma_{max} = f\left(\Delta\varepsilon_n\right) \tag{3}$$

One of the more prominent improvements to the concept of the critical plane approach was developed by Fatemi and Socie. Fatemi and Socie [35] expressed a modified parameter which accounts for both plastic strain and stress, i.e.,

$$DP_{FS} = \frac{\Delta\gamma^p_{max}}{2}\left(1 + k\left\langle\frac{\sigma^n_{max}}{\sigma_y}\right\rangle\right) \tag{4}$$

where the Fatemi-Socie parameter is denoted DP_{FS}, $\frac{\Delta\gamma^p_{max}}{2}$ is the maximum plastic shear strain range, k is a stress sensitivity parameter, σ^n_{max} is the peak normal stress to the plane of maximum shear strain range, and σ_y is the yield stress. The value of the

Macaulay bracket $\langle x \rangle$ term has the greater of 0 or the interior value. The tensile stress normal to the crack plane serves the same purpose as the $\Delta\varepsilon_n$ term of the initial Brown and Miller parameter by increasing the damage parameter value to account for reduced frictional effects and thus increased crack propagation rate.

The initial formulation of these damage parameters was posed at the macroscopic scale. However, when averaged over a finite fatigue damage process volume at the microstructure scale [36], these values are referred to as a fatigue indicator parameter (FIP) [37]. The Fatemi-Socie FIP (FS FIP) is formulated as

$$FIP_{FS} = \frac{\Delta\gamma^{p\ *}_{max}}{2}\left(1 + k\left\langle\frac{\sigma^{n\ *}_{max}}{\sigma_y}\right\rangle\right) \tag{5}$$

with the asterisk * indicating that volumetric averaging should be performed. Fundamental properties of the FS FIP were examined by McDowell and coworkers [18, 32] which showed good agreement with ΔJ integral approaches experimental results of multiaxial fatigue. The application of the FS FIP has been further justified by Przybyla and coworkers for both Ni-base superalloys (IN100) [38] and Ti-6Al-4V (Ti-64) [39]. More recently it has been observed that the FS FIP provides good agreement with crack tip displacements (CTD) in different alloyed materials. Castelluccio and McDowell [40] applied this method to develop a mesoscale crack model in RR 1000. Due to preferential use of the FS FIP, further references to specific FIP responses will refer to the FS FIP unless otherwise noted.

FIPs have also been applied to predict fatigue crack formation. Tanaka and Mura [41] derived a model for dislocation accumulation. Chan [42] and Shenoy et al. [43] extended this work to provide a parameter for crack formation based on continuum simulations.

$$N_{FOR} = \frac{a_g}{d_{gr}}\left(FIP\right)^{-2} \tag{6}$$

Size dependence of the slip accumulation process is incorporated via the size of the current grain d_{gr}. Castelluccio [40] incorporated low disorientation neighbor grains to contribute additional length to the d_{gr} term due to observed "super-grain" crack formation behavior in the RR1000 alloy. Calibration of the model is achieved via the a_g term, which measures the mechanical irreversibility of the slip accumulation process.

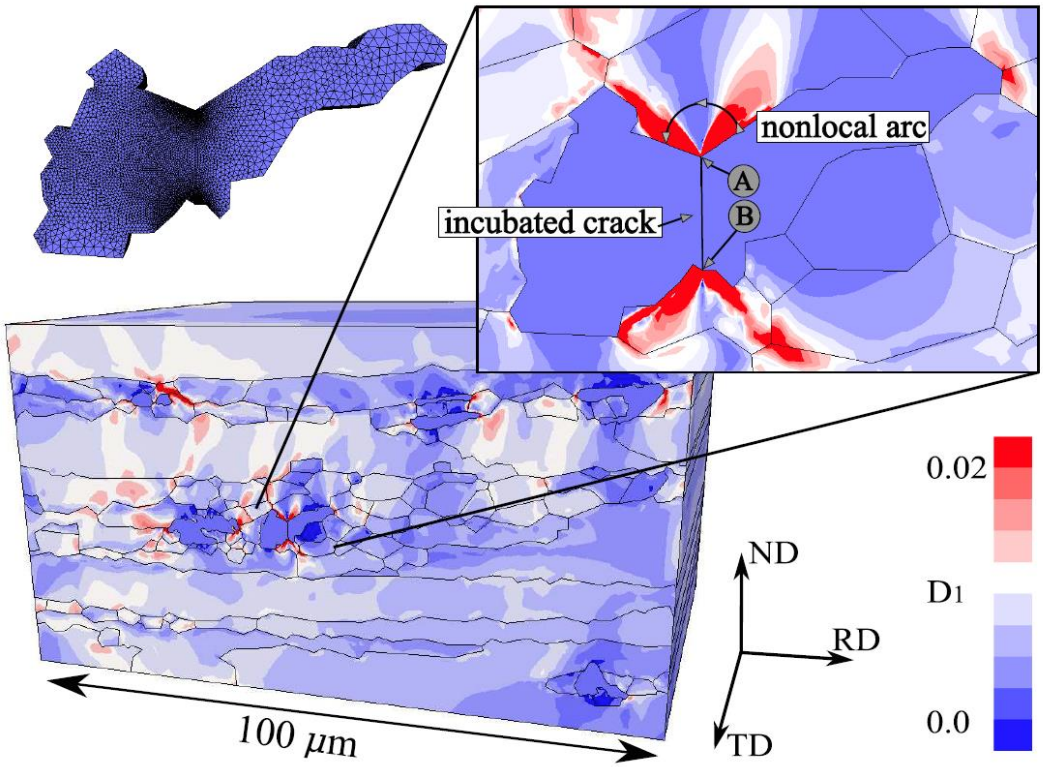

Figure 7. Nucleation microstructure and damage parameter averaging area as employed by Hochhalter et al. [44].

Of particular relevance to this thesis is a series of papers by Bozek et al. [10, 44, 45] who studied the formation of fatigue cracks at constituent particles in Al 7075-T651. This series covers constituent particle cracking probability, geometric considerations of fatigue crack formation at cracked particles, and a proposed damage parameter for modeling the number of cycles to extend a crack into the surrounding matrix. Several

damage parameters were studied over the course of this work including slip based metrics and the FS FIP. All damage parameters were averaged over a finite process area constrained by the limitation of the accuracy of the finite element method (FEM) model used, as well as the physical damage zone caused by a small crack. The proposed parameter with best agreement to experimentally observed crack nucleation lives includes the maximum shear strain over all slip systems ΔD_1^{max} as well as the accumulation per load cycle ΔD_1^{max}.

$$N_{FOR} = \frac{\left(\frac{\sigma_{\theta\theta}^{max}}{\sigma_{\theta\theta}^{ult}}\right)^{\frac{1}{\alpha}} - D_1^{max}}{\Delta D_1^{max}} + 1 \tag{7}$$

These values are taken at the radial position of maximal ΔD_1^{max} over the semicircular averaging surface area. Again, a tangential stress term $\sigma_{\theta\theta}^{max}$is used to incorporate the cumulative damaging effect of the opening of the crack surface relative to this maximum accumulation direction. Both $\sigma_{\theta\theta}^{ult}$ and α are fitting parameters used to describe the stress dependence of the nucleation process.

In addition to crack formation, the FS FIP demonstrates good agreement with the $\overline{\Delta CTD}$ expressions previously related to crack growth rate. Castelluccio and McDowell [46] established the relationship of the crack tip displacement magnitude ΔCTD and the FS FIP averaged along a banded region in Cu. The banded region exhibits features of a sufficient averaging domain for reduced (though not eliminated) mesh sensitivity, with the resultant values having good agreement with the observed ΔCTD values over a range of load mixity and amplitudes.

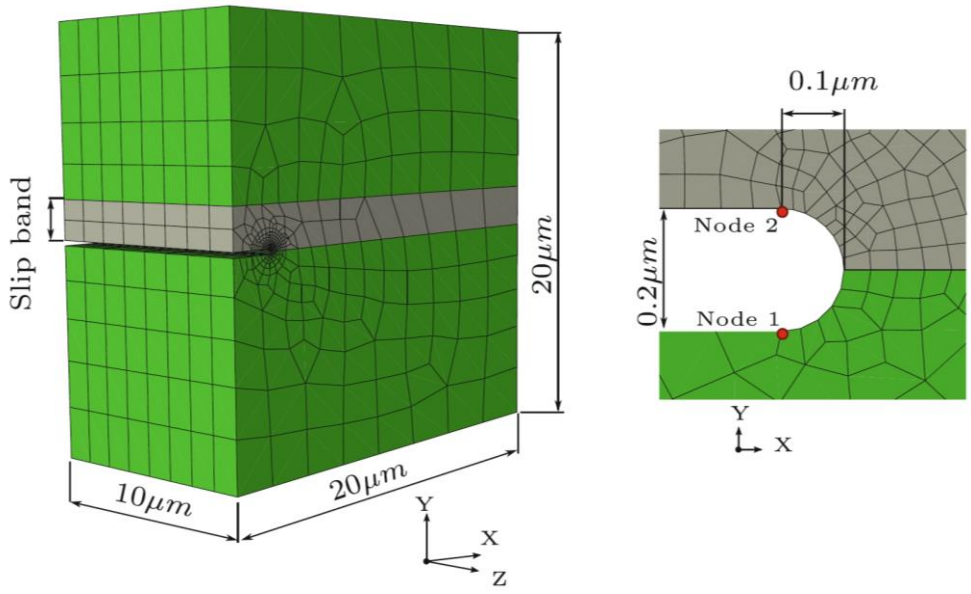

Figure 8. Mesh with highlighted slip band utilized by Castelluccio and McDowell [46] to obtain ΔCTD to FIP relationships for a Cu single crystal.

The resulting relationship is shown to be nearly linear in nature, with $b \approx 1.1$ for the relationship

$$FIP = C\left(\Delta CTD\right)^{b} \tag{8}$$

with C being an additional fitting parameter for the correlation. This relationship has been applied successfully to a mesoscale propagation model with accurate predictions of the fatigue lives for both RR1000 [47], Al 7075-T6 [48], and an adapted formulation applied to IN 100 [49].

In addition to the study performed by Castelluccio and McDowell, Rovinelli et al. [50] studied various FIP forms (including those of Hochhalter et al.) and their energetic equivalents. These simulations were conducted in varying instantiations of cylindrical IN100 specimens under uniaxial tension with static cracks. The energetic equivalent of the FS FIP was observed to vary with predictable and expected patterns while interacting with microstructural features such as grain boundaries of varying misorientation. This

parameter is also shown to relate to crack length in a similar manner to traditional crack growth rate factors such as ΔK.

1.2.4: Long Crack Growth

Following crack growth beyond several (3-10) microstructural barriers in spacing, the growth is referred to as PSC. In this stage, crack growth is still strongly influenced by plasticity induced closure and is often treated by elastic-plastic fracture mechanics (EPFM). Dowling and Begley [51] proposed the ΔJ-integral as a parameter to incorporate crack length and load conditions and relate them to crack growth rate via the material constants C and m.

$$\frac{da}{dN} = C\left(\Delta J\right)^m \tag{9}$$

This equation is an extension of the Paris law used to describe crack growth rate via linear-elastic fracture mechanics (LEFM). This is one of the most important historical relationships of crack growth, and is still used in many forms today [52-54].

$$\frac{da}{dN} = C\left(\Delta K\right)^m \tag{10}$$

In this relationship, C and m are material constants used to fit to experimental data and ΔK is the change in stress intensity factor over a loading cycle. This equation, applied by Paris et al. [55] has been utilized countless times, with many efforts being made to correlate different loading conditions to the same nominal crack growth rate formulation. Indeed, early research efforts into MSC depict crack growth rates as a function of ΔK, even though many assumptions are invalidated for cracks below ~10 grain diameters in length [5, 8].

1.3: Crystal Plasticity

Fatigue can be understood to have defining characteristics, and thus require models and understanding of material behavior, across multiple length scales [56].

Crystal plasticity models have become widely used to predict various features of polycrystalline deformation, including texture development [57] forming limits [58], and fatigue response [14, 46, 59, 60]. These models apply continuum assumptions to decompose deformation along crystallographic slip planes. Hochhalter et al. [44] and Dixit and Dixit [61] estimate these assumptions to be valid for models with elements on the order of 1 μm and but break down as one approaches element size of nm. Shenoy et al. [43] also note that for materials forming PSB, the element size should be no smaller than the PSB width. These restrictions are sufficient since the models considered in this work are simulated in volumes of 10-600 μm sidelength with fewer than 10^6 elements.

While the primary emphasis of this work is not in the constitutive calibration of a specific material model, all of the analysis is conducted from simulations of crystal plasticity codes within finite element method (FEM) frameworks. These types of models are referred to as crystal plasticity finite element method (CPFEM) models. Specifically, all material models used in this work are implemented in the user material subroutine (UMAT) of Abaqus. Several assumptions, as well as the results discussed depend upon a fundamental understanding of the continuum mechanics approach used to model polycrystalline behavior, thus the basic framework for crystal plasticity modeling will be reproduced in a limited fashion here. For additional details about numerical schemes, model forms, and the history of crystal plasticity models see the extensive summary of McDowell [56].

For implementation in finite element method (FEM) codes, a relationship must be devised between the material deformation and the stress state. Following traditional continuum mechanics of large deformations, the total deformation gradient is a tensor which maps an infinitesimal neighborhood of the material point in the initial reference frame (vector $d\mathbf{x}$) to the deformed configuration as $d\mathbf{y}$, i.e.

$$d\mathbf{y} = \mathbf{F} \cdot d\mathbf{x} \tag{11}$$

A fundamental assumption of the crystal plasticity method is the multiplicative decomposition of the total deformation gradient into elastic-plastic constituent tensors. This decomposition follows from works by Bilby et al. [62] and Lee [63].

$$\mathbf{F} = \mathbf{F}^e \cdot \mathbf{F}^p \tag{12}$$

Figure 9 illustrates the concept of the total deformation tensor as interpreted as a series of deformations by the plastic deformation gradient $\mathbf{F}^p$ into the intermediate configuration and by the elastic deformation gradient $\mathbf{F}^e$ from the intermediate configuration to the current, deformed configuration. Particular note should be made about the importance of the intermediate configuration in the following crystal plasticity formulation.

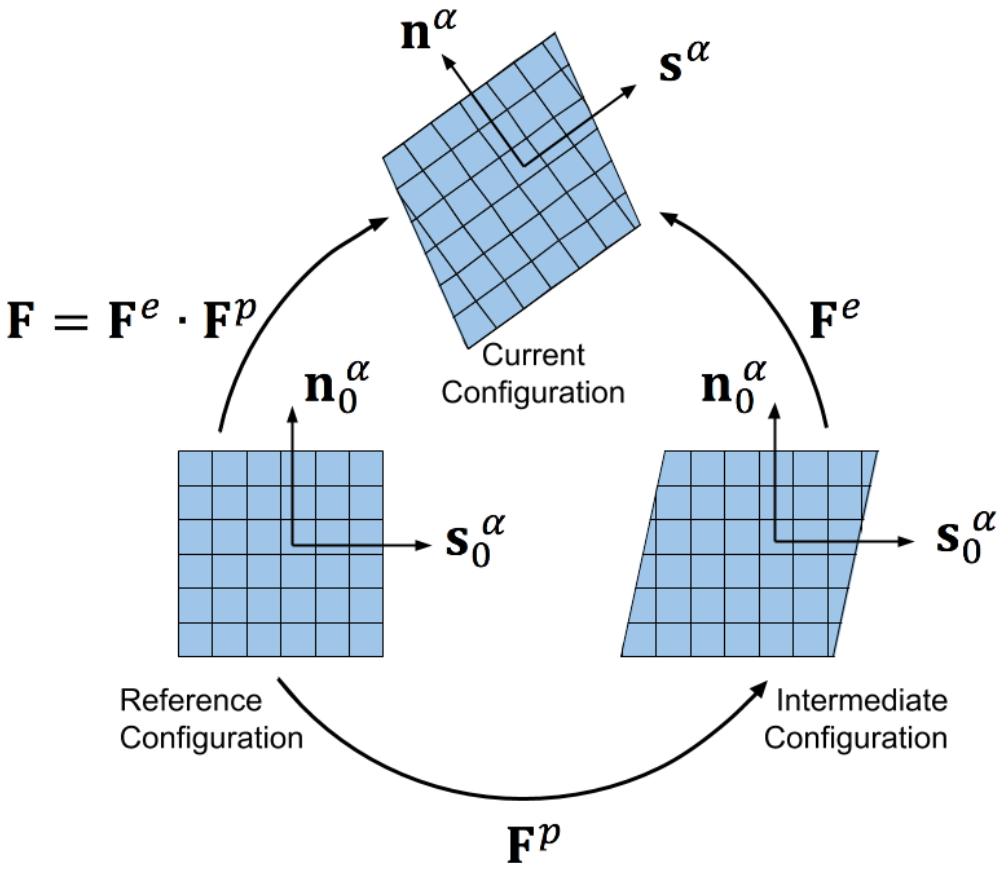

Figure 9. Multiplicative decomposition of the elastic-plastic deformation gradient adapted from [64].

In the same way, the plastic deformation rate may be related to the plastic velocity gradient by the following equation.

$$\mathbf{L} = \dot{\mathbf{F}} \cdot \left(\mathbf{F}\right)^{-1} = \mathbf{L}^{e} + \mathbf{L}^{p} \tag{13}$$

Since this is the fundamental relation of the deformation to the constitutive model, the material time derivative of the plastic deformation gradient was proposed by Asaro [65] to be related to the shearing rates on the individual slip systems by

$$\dot{\mathbf{F}}^{p} = \left(\sum_{\alpha}^{n_{\alpha}} \dot{\gamma}^{\alpha} \mathbf{s}_{0}^{\alpha} \otimes \mathbf{n}_{0}^{\alpha} \right) \tag{14}$$

where $\dot{\gamma}^{\alpha}$ is the shearing rate on the α slip system, $\mathbf{s}_{0}^{\alpha}$ is the slip direction vector and $\mathbf{n}_{0}^{\alpha}$ is the slip plane normal vector, both in the intermediate configuration. This continuum mechanics approach of expressing slip on the various slip planes as an internal state variable is perhaps the most fundamental concept of crystal plasticity models.

With this fundamental relationship of the deformation in place, an expression relating the deformation to the resolved shear stresses on each system must be made. This parameter forms the relationship from stress state back to deformation rate and is necessary for implementation in FEM. The process begins by considering the plastic velocity gradient $\mathbf{L}_{\mathbf{0}}^{\boldsymbol{p}}$ in the intermediate coordinate system as a function of the previously expressed variables.

$$\mathbf{L}_{0}^{p} = \dot{\mathbf{F}}^{p} \cdot \left(\mathbf{F}^{p}\right)^{-1} = \sum_{\alpha=1}^{n_{a}} \dot{\gamma}^{\alpha} \mathbf{s}_{0}^{\alpha} \otimes \mathbf{n}_{0}^{\alpha} \tag{15}$$

The current configuration velocity gradient $\mathbf{L}^{\boldsymbol{p}}$ is then

$$\mathbf{L}^{p} = \mathbf{F}^{e} \cdot \mathbf{L}_{0}^{p} \cdot \left(\mathbf{F}^{e}\right)^{-1} \tag{16}$$

with the elastic velocity gradient $\mathbf{L}^{\boldsymbol{e}}$ similarly expressed

$$\mathbf{L}^{e} = \dot{\mathbf{F}}^{e} \cdot \left(\mathbf{F}^{e}\right)^{-1} \tag{17}$$

The combined value $\mathbf{L}$ is related to the total deformation gradient by

$$\mathbf{L} = \mathbf{L}^e + \mathbf{L}^p = \dot{\mathbf{F}} \cdot \mathbf{F}^{-1} \tag{18}$$

The elastic strain tensor can then be constructed using the previous relationships. As in many material models, the plastic strains must be removed and only the elastic strains are considered when calculating the stress state. The elastic Green strain tensor $\mathbf{E}^e$ is constructed by

$$\mathbf{E}^e = \frac{1}{2}\left[\left(\mathbf{F}^e\right)^{\mathrm{T}} \cdot \mathbf{F}^e - \mathbf{I}\right] \tag{19}$$

where **I** is the second rank identity tensor. The second Piolo-Kirchhoff **T** stress tensor in the intermediate configuration is then expressed as

$$\mathbf{T} = C : \mathbf{E}^e \tag{20}$$

Finally, the Cauchy stress tensor σ in the current configuration is

$$\sigma = \frac{1}{\det\left(\mathbf{F}^e\right)} \mathbf{F}^e \cdot \mathbf{T} \cdot \left(\mathbf{F}^e\right)^{\mathrm{T}} \tag{21}$$

The stress state may then be related to the occurrence of slip in the modeled slip systems. The resolved shear stress on each slip system is

$$\tau^\alpha = \sigma : \left(\mathbf{s}_0^\alpha \otimes \mathbf{m}_0^\alpha\right) \tag{22}$$

An iterative or explicit solver may then be applied with the definition of a flow rule and the shear strain rate $\dot{\gamma}^\alpha$ on each slip system. Specific flow rules are discussed in this work in the context of the material models applied to various problems throughout the work.

In addition to the treatment of single grain response, models may also be considered to address grain boundary interactions. The most commonly used treatment of grain boundaries is in fact to neglect explicitly treating grain boundaries. Instead, compatibility of deformation is enforced via FEM in elements of neighboring grains [56]. This approach can be justified by the lack of information, and significant modeling complexity involved in grain boundary behavior in many materials. Soh [66] proposed the use of multi-grain elements to model boundary behavior (relatively) independent of

mesh density. Barbe et al. [67] found that the use of reduced integration elements coupled with the stair stepped nature of grain boundaries in a voxelated mesh may overestimate stress/strain values at grain boundaries. Héripré et al. [68] also demonstrated the potential for FEM grain boundary geometry to modify the location of the maximum stress responses. This information is included to acknowledge explicitly any deficiencies of the models utilized in this work, which do not explicitly treat grain boundaries and exclusively use the voxelated mesh representation and the inherent stair-stepped boundaries this produces.

1.4: Synthetic Microstructures and Statistical Volume Elements

In addition to the necessity of appropriate modeling techniques, effort must be made to ensure that simulated volumes are equally representative of those found in real material systems. Throughout this text, the concept of a synthetic microstructure will be used to describe volumetric instantiations described by a microstructure function and constructed from a set of target statistics, ideally quantified by direct observation of desired material systems.

The concept of a "microstructure function" representing the spatial distribution of a microstructure instantiation has been developed over a series of publications [69-72]. These descriptors have been applied to many process-structure-property relationships and material design applications. The microstructure function $m_{\mathbf{s}}^{\mathbf{h}}$ may be considered for all spatial locations $\mathbf{s}$ in the volumetric space Ω with a material state vector $\mathbf{h}$ in the z dimensional space H. The microstructure function then represents the probability of finding a local state in the observation window. This broad definition of the microstructure function includes continuous and discrete material descriptors. To reduce this theoretically infinite state space, the microstructure representations discussed in this work will consider spatial variation of only two parameters: phase and crystallographic orientation. All models in this work use integers for the phase state, indicating only a

single phase may exist at any given location in the defined microstructure function. The very concept of a microstructure function lends itself to a voxelated discretization of the material volume. A voxel, as the 3D equivalent of the pixel, may be considered as a rectangular prism which contains a single representative value.

With the concise representation of the distribution of microstructure states, description and interpretation of spatial statistics used to characterize different microstructures becomes significantly easier. While traditional statistical representations of microstructures rely on univariate distributions particularly at an ensemble level, e.g. grain size distributions, there exist more accurate spatial statistics to characterize microstructures. The concept of a two-point statistic [73] is particularly useful to this work, and therefore mentioned explicitly. This statistic is defined over the Ω space with a finite number of spatial locations S as

$$f_{\mathbf{t}}^{\mathbf{h}\mathbf{h}'} = \frac{1}{S}\sum_{0}^{S-1} m_{\mathbf{s}}^{\mathbf{h}} m_{\mathbf{s}+\mathbf{t}}^{\mathbf{h}'} \tag{23}$$

The joint probability of finding state $\mathbf{h}$ at the location $\mathbf{s}$ and state $\mathbf{h}'$ at location $\mathbf{s}+\mathbf{t}$ is the value $f_{\mathbf{t}}^{\mathbf{h}\mathbf{h}'}$. Note that this value is typically computed over a periodic space such that $\mathbf{t}$ spans the same possible coordinates as $\mathbf{s}$.

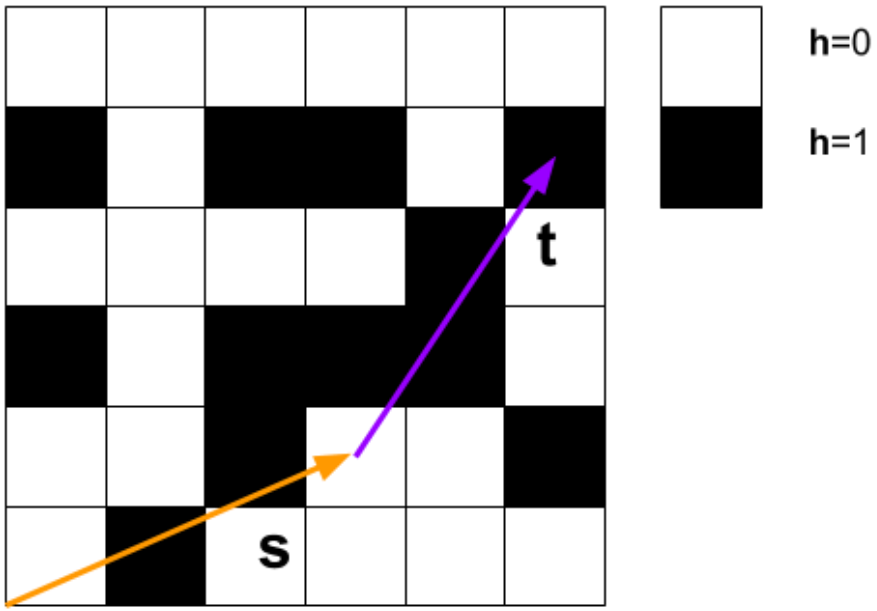

Figure 10. Two point spatial statistic for the cross-correlation of a two-phase microstructure function.

The concept of a representative volume element (RVE) extends naturally from the notion of a microstructure function. An RVE may be defined for material structure and material property statistics. The most prominent definition of the RVE size, known as the Hill condition, may be stated as:

"a sample that (a) is structurally entirely typical of the whole mixture on average, and (b) contains a sufficient number of inclusions for the apparent overall moduli to be effectively independent of the surface values of traction and displacement, so long as these values are macroscopically uniform." [74].

By expanding the (b) definition to include any material response of interest, the RVE size becomes a function of the response type. Lacy et al. [75] have demonstrated that statistical homogeneity may not be achievable for certain damage parameters, and that indeed characterization should consider gradient values. This concept has been extended with the work of Przybyla and McDowell [39] to statistically characterize material properties in the region of significant damage via the use of marked correlation

functions. Gitman et al. [76] demonstrated that the existence of an RVE size for a computational model may not be present (or be prohibitively large) based on work with composite simulations and stress/strain response. These studies indicate that the RVE can be very large for high cycle fatigue (HCF); in fact, it can exceed the laboratory specimen or component scales. Often times the very definition of an RVE becomes unclear under complex loading conditions with stress concentration factors since it is impossible for the entire specimen to be subject to the same nominal stress-state [60]. In such cases, it is instructive to consider the random (aleatory) variability associated with randomness of microstructure (both intrinsic and extrinsic attributes) at length scales well below the laboratory specimen scale.

Modeling approaches may address the problem of intractable computation for properties with prohibitively large RVE size by the application of an ensemble of statistical volume elements (SVE). This approach has been used to quantify macroscopic properties [77], spatial distributions of stress/strain [78], and fatigue responses [43, 79]. By allowing for fluctuations in the individual SVE response, computational times may be significantly reduced while still providing a convergent description of the property of interest.

RVE may also be of interest as described by the spatial statistics representing a microstructure of interest. This may be seen as an extension of the (a) definition from the Hill condition. Theoretically, this definition can be applied to any statistical measure. Since a finite number of samples are taken to approximate the population, a convergence threshold must be applied to create a definition for the RVE. This simple definition also neglects uncertainties associated with the construction of the idealized definition of the typical microstructure desired, e.g. the parameters of a statistical distribution used to represent the grain sizes observed in a material.

1.5: Thesis Outline

As significant effort is expended in the development of accurate crystal plasticity models and analysis techniques become more intricate, the benefit of developing standardized protocols and frameworks becomes more tangible. This work contributes to the body of knowledge regarding the interpretation of extreme value results using FIPs and the selection of simulation parameters independent of the chosen model. Additional model developments provide more accurate life predictions of the Al 7075-T6 alloy under a variety of loading conditions. The functionality of all of the included work is demonstrated within an automated framework for crystal plasticity simulations. This framework, which includes support for multiple material models and analysis methods, is intended to advance the pace of development within the McDowell group and the Georgia Tech materials simulation community.

This work began with an introduction of the basic material and modeling considerations employed in this paper. A summary of the fundamental basis of the mechanical response of metals in fatigue was presented to contextualize the material responses, modeling strategies, and analysis techniques presented in this work. Special attention was paid to the fundamental processes of fatigue crack formation and microstructurally small growth in various metal alloy systems. Similarly, the computational techniques applied to microstructure sensitive models were introduced and discussed. The continuum mechanics framework for crystal plasticity models was presented as these models are utilized throughout this work to simulate material responses correlated to fatigue damage.

Chapter 2 introduces a new, automated material simulation pipeline. This pipeline has been developed around the abundance of crystal plasticity models developed within the McDowell group. Various aspects of the design of this pipeline are discussed and a relatively complete documentation of features and options is provided. This pipeline is applied to the simulations conducted throughout the remainder of this work. In addition,

the analysis and plotting discussed in this thesis are incorporated in the various Python modules that compose the entire pipeline.

Following the discussion of CPFEM and development of an automated simulation framework, application of extreme value distributions for fatigue resistance characterization is discussed in Chapter 3. This method of ranking microstructures is then used to analyze the fatigue responses for two material models under varied loading amplitudes with the intent of constructing a response surface for the variability of decision making across various simulation parameter ranges. Statistical adjustments will be made to the extreme value distributions to compare across unequal SVE sizes.

This treatment of extreme value responses prompted investigation of the life-limiting distribution of FIPs as a material response. Chapter 4 follows the investigation into the behavior of the cumulative distribution functions (CDF) of FIPs. Following this investigation, a new characterization method describing the extreme values of FIP responses is then proposed. This characterization and extrapolation method is used to compare microstructure fatigue rankings across a variety of materials, crystallographic textures, and simulation parameters. Sensitivities of extreme value rankings are also presented for comparison with the previously developed SVE maximum approach to extreme value distribution construction.

Chapter 5 introduces a new mesoscale crack propagation model, which has been developed to retain desirable traits of methods utilized by Musinski and Castelluccio. This method also benefits from the application of improved geometric rigor and the incorporation of a nucleation simulation phase. Taken together, the fatigue model may be used to predict fatigue lives in the Al 7075-T6 material system.

In Chapter 6, this new method is calibrated and employed to predict fatigue life responses in synthetic microstructure instantiations of rolled Al 7075-T6. Extensive comparison is made to experimental data, especially that of Zhao and Jiang [80] to emphasize the applicability of the presented models over a wide range of loading

conditions and amplitudes. In addition, slip system activation ahead of propagating cracks was briefly investigated for the Ohno-Wang model. Finally, multiaxial fatigue response surfaces were constructed and compared for two separate fatigue model forms. Differences in the response surfaces may be traced to various fatigue model properties and calibrations while clearly demonstrating the importance in capturing material behavior and the limitations of models when predicting fatigue response in varying load conditions.

CHAPTER 2: AUTOMATED SIMULATION PIPELINE

2.1: Motivation

As models improve in predictive capability and as computational resources increase, computer-automated design tools become feasible to apply to material design scenarios. These tools are increasingly powerful and have been used in various disciplines to improve performance metrics and reduce design time while affording researchers and practitioners time to dedicate towards other skilled tasks [81-83]. Many of these techniques require significant knowledge of the system to be optimized. This information may be in the form of a database, surrogate model, or models evaluated during optimization. Optimization and design tasks are thus aided by the standardization of simulation routines and analysis methods, particularly when the data of interest are distributions of values obtained to multiple synthetic reconstructions of material volumes.

In the domain of material design and development, an important thrust of recent research efforts has been the Materials Genome Initiative (MGI) [84], announced by the White House Office of Science and Technology Policy in an effort to preserve strategic superiority in materials development in the United States of America. Materials development has traditionally required significant trial-and-error and been the source of many redundancies in research efforts, something that can be improved with iterative design processes using simulations to limit experimental data sets required. One of many efforts to improve development rates is the Materials Project [85] which includes a collaborative database with the desire to produce and validate data on demand for design exploration. We seek to similarly pursue MGI objectives by extending and improving toolchains with a focus on materials design.

Initial motivation and funding for the development of this automated simulation pipeline was provided by Dassault Systèmes Simulia Corp. with the original intent to

provide a suite of tools to support rapid analysis of the fatigue sensitivities of crystal plasticity models. Continued development has occurred with increased efforts to provide documentation and support for various material models, post-processing methods, and simulation strategies. To facilitate the organization, development, and maintenance of code, all of the software produced in this group has been version controlled using the Git version control system. The software repository is located on an enterprise version of GitHub maintained locally at Georgia Tech. The McDowell-Lab organization now maintains control of several repositories for material models and simulation packages, with the intent of open-sourcing projects when feasible.

2.2: Simulation Modules

The main goal of the automated simulation pipeline is to provide intuitive and fast initiation and management of many simulations required to gather comparative statistics on fatigue in different material models. To facilitate this, the core functionality of the software is broken down into four Python [86] modules, each dedicated to a logically distinct portion of the pipeline as depicted in Figure 11. The following paragraphs provide an overview of the functionality and interdependence of these modules as well as any external software used. The reader is also encouraged to reference APPENDIX A and the formal documentation files located on the McDowell-Lab repositories for additional information.

The overall structure of the pipeline reflects the ad-hoc development approach combining functionality of codes from various students into a unified environment. The overall structure strives to be highly flexible by using good coding practice and small, highly specific functions. The Python language was chosen to reflect this flexible scripting desirability as well as having several advantages particularly for the academic environment including, but not limited to, free use (no license required), compatibility

(across operating systems), ease-of-use, and large number of available packages for scientific computing.

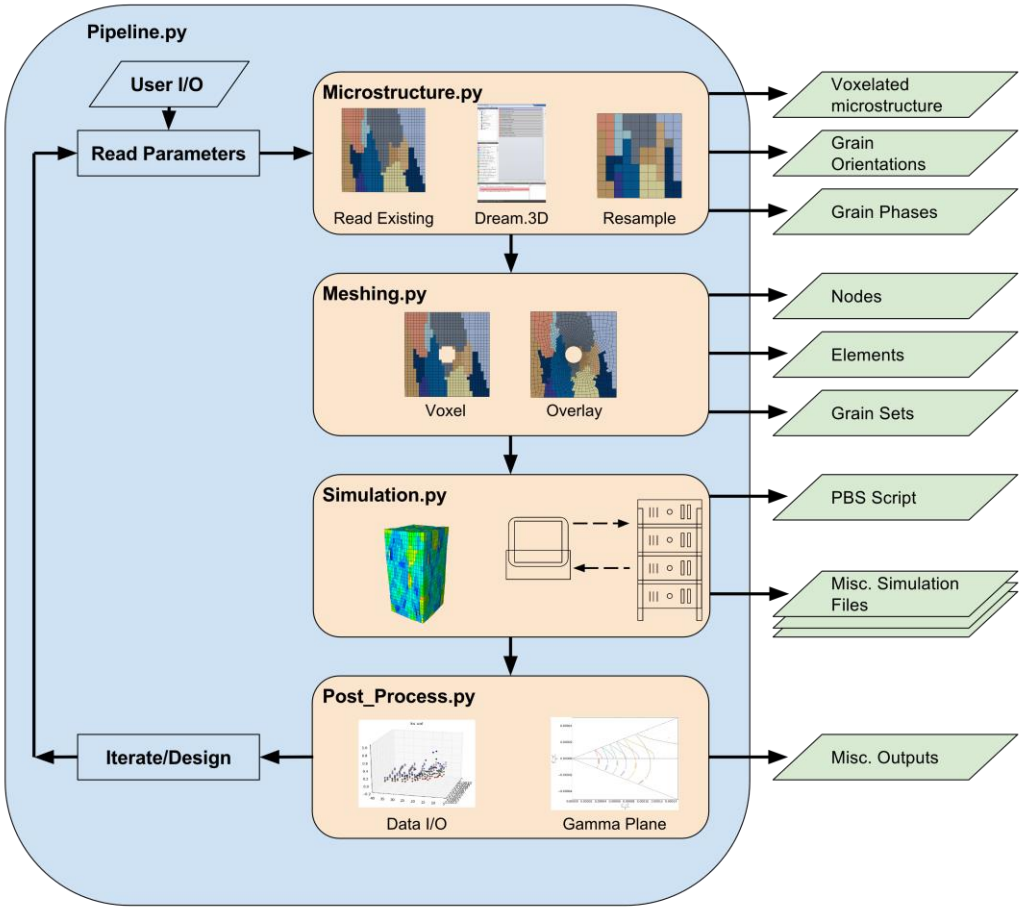

Figure 11. Overview of the Automated Simulation Pipeline modules and organization.

2.2.1: Microstructure

The first stage in any crystal plasticity simulation is instantiating the desired synthetic microstructure. Associated functions are contained in the *microstructure.py* module. The synthetic representation of the material system includes statistical data e.g. texture, grain sizes, aspect ratios, as well as higher order spatial statistics [87-89]. Each of

these factors can have a profound impact on the simulated material response as indicated in this work and the work of many others e.g. [10, 90]. The internal storage of the microstructure *ms* is a NumPy [91] array (ndarray) with 3 dimensions representing, in order, the x, y, and z volumetric locations within the microstructure. Each index stores an associated grain number $g \in [0, n-1]$, and must be accompanied by ndarrays *orientations* and *phases* containing the orientation and phase for each grain. This information is inherently organized in a voxelated representation which has been commonly used for many crystal plasticity simulations of the McDowell group and others [40, 59, 70, 79]. Since it is difficult for a single research group or individual to keep pace with the developmental needs associated with synthetic microstructure generation of increasing fidelity, a third party tool is primarily used for microstructure reconstruction.

Dream.3D [92] is used due to its catalog of extensive plugins, rapid adoption in the community, and open-source nature. This software also uses a voxelated representation internally and optimizes synthetic microstructures to a variety of input statistics including grain size and shape, phase volume fraction and crystal orientation and misorientation [89, 93]. The primary use case is the instantiation of multiple synthetic microstructures via the PipelineRunner.exe distributed with Dream.3D. The *microstructure.py* module also contains functions for reading and writing phase, orientation and grain assignments from VTK, OIM, and internal text formats. Since there are several ways to represent crystallographic orientations [94], an internal standard of the Bunge-Euler angles (expressed in radians) is selected for consistency in the pipeline. This is consistent with the selection of rotation standard used by Dream.3D. Finally, resampling of the voxelated microstructure may be performed in this step to reduce data density. The average time taken in this step is several seconds per microstructure. A 100x100x100 element microstructure consisting of four textured phases and 3500 grains was produced in less than 25 seconds.

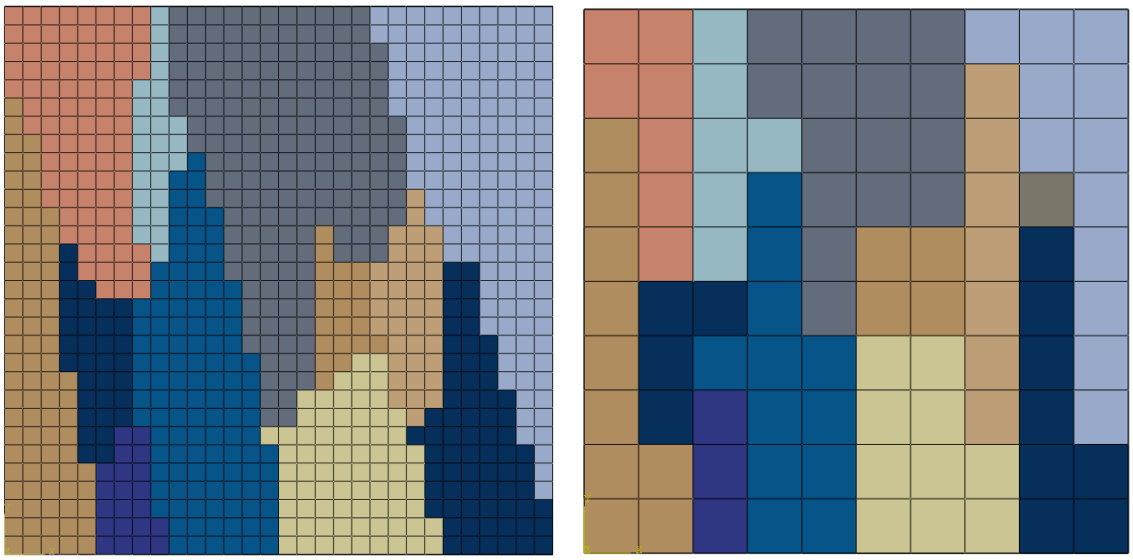

Figure 12. 2D cross-sections of the 3D voxelated representation of a synthetic microstructure (left) and subsampled representation (right).

2.2.2: Meshing

The next step in the pipeline is the transition of the voxelated microstructure representation to a mesh suitable for simulation in the FEM. Such a mesh requires material assignments and nodal connectivity for each element. The functions relevant to mesh operations are contained in *meshing.py*. Each element has an associated grain number in the ndarray *el_grains* while the nodal connectivity for each element is assigned in the *elements* ndarray. Since material properties are assigned on a grain-by-grain basis, a *grain_el* dictionary is also constructed. The keys to this dictionary are the grain numbers with the number -1 reserved for Abaqus material behaviors such as elasticity or isotropic plasticity. During pipeline execution, the selected material module determines the specific implementation of this behavior. Material modules and their functionality are detailed in the section entitled Material Repositories. Having obtained the microstructure information, there are two main methods of constructing a suitable FEM mesh.

The first, and most common, method of mesh construction is a voxelated mesh constructed from the voxelated microstructure representation and size information. Using this method the number of FEM elements in each is determined by the *shape* (number of elements per dimension) and *size* (extents of the mesh in each direction) to create a prismatic mesh with an arbitrary number of elements and aspect ratios. In addition to the trivial structured mesh possible by a fully dense microstructure, meshes can be constructed with missing elements to create various stress intensification features such as cracks, notches, and through holes. The generic implementation of this requires the construction of a *mask* (ndarray of the same dimensions as *ms*) of Boolean values True where the element should remain in the mesh, and False where the element should not. The nodes are placed if any of the potentially connected elements are True in the mask, or if a mask is not provided. Finally, brick elements are assigned nodal connectivity based on the created node numbers and the inherent structure to a voxelated mesh for each of the eight nodes required. A cubic mesh with no holes (worst case) for a mesh of 125,000 elements is generated in less than one second.

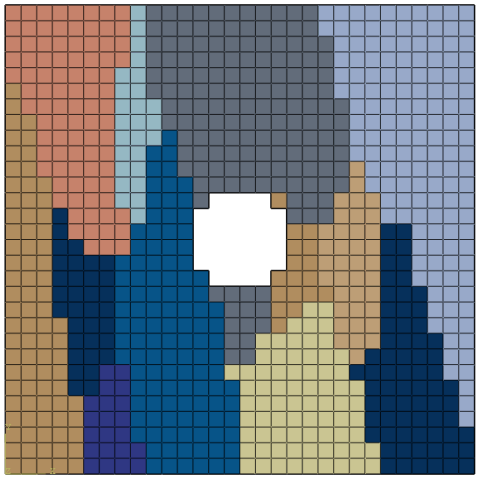

Figure 13. 2D cross section of a 3D voxelated, masked FEM mesh.

The second meshing strategy requires a mesh generated from another source. A common use case is the input of an .inp file describing the mesh geometry, in which case

the node spatial position and element connectivity are read in directly from the mesh file. Note that node and element numbers are adjusted to a 0-based index (native Python indexing convention). To facilitate automation and flexibility in the pipeline, the ability to generate several different mesh geometries using Abaqus [95] scripting is included. These geometries include the same notch, hole, and crack geometries discussed previously.

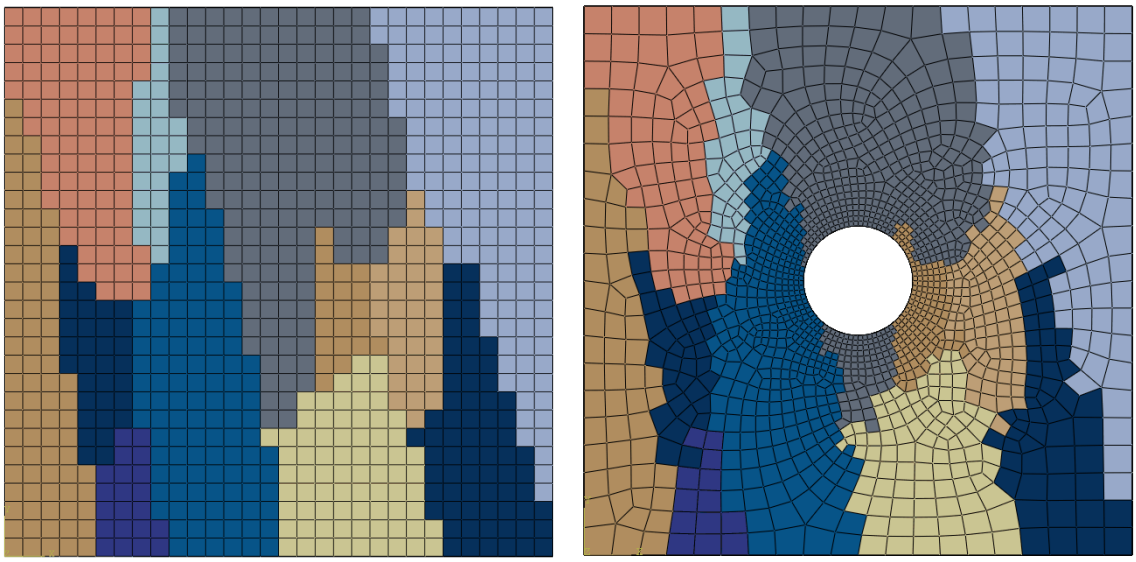

Figure 14. Overlay of microstructure (left) on unstructured mesh (right) as viewed from the z-axis.

Once the mesh information is read into the pipeline, a process referred to as overlaying the mesh occurs. This process links the microstructure information to the mesh to allow FEM simulation. Arbitrary placement of the microstructure within the mesh volume is accomplished by provided offsets from the mesh origin. By default, the microstructure is centered within the mesh volume. With the relative spatial locations set, overlaying is accomplished by computing which microstructure voxel that contains the coordinate of each element centroid. If this location is contained within the microstructure, an index of *ms* is computed and the grain value from this index is assigned to the element. Alternatively, if the centroid location is outside of the

microstructure, a grain value of -1 is assigned. Assigning a default grain value outside of the allowable range is used to create a material set with behavior differing from that of the UMAT. This feature may be particularly useful to reduce the computational effort required to simulate large components by having simple linear elasticity or isotropic plasticity outside of the microstructure region. Reading and overlaying a mesh of 125,000 elements is accomplished in less than 3 seconds.

A final feature of the meshing module is the ability to generate banded meshes to support the mesoscale fatigue crack growth algorithms of Hennessey and Castelluccio [47]. To band the microstructure, a bandwidth is supplied along with the crystallographic planes and grain orientations. For every element, the distance to a crystallographic plane passing through the grain centroid is computed. Elements are assigned a layer based on the bandwidth interval within which they reside for each plane computed. An example of a banded mesh is presented below. This feature is provided to retain backwards compatibility with codes previously used in the McDowell group. A mesh of 125,000 elements is banded in less than 15 seconds.

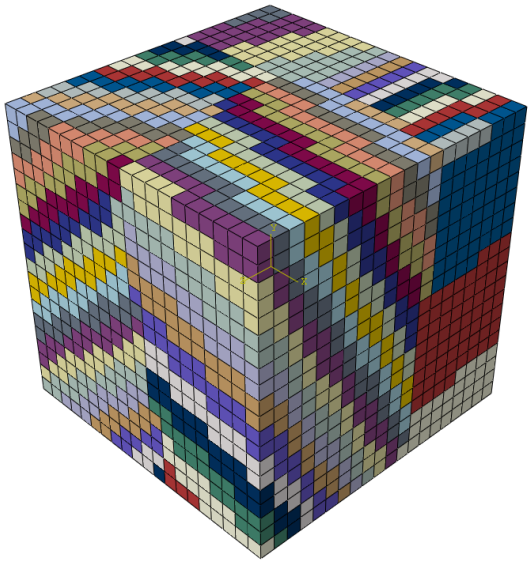

Figure 15. Example banded mesh. Different colors indicate different layers for a single crystallographic plane. Grain boundaries may be observed where a transition in the plane orientation occurs.

2.2.3: Simulation

The third module required for pipeline execution is the *simulation.py* module. This module contains functions specific to simulation parameters for specific FEM software as well as executing simulations and downloading results from a remote cluster. Prior to these functions being executed, any material and mesh specific parameters should be written to the corresponding simulation files.

All simulations belonging to the same batch have the same loading conditions and mesh, with only the microstructure instantiations differing. To accommodate this, a common loading file, *loads.inp*, is created to contain the applied loading steps, output requests, and boundary conditions. Arbitrary loading conditions are described by defining the components of the displacement tensor for the extents of the geometry. Any displacement not explicitly defined by the user is left unconstrained by the applied boundary conditions (allowed to displace freely). Displacements are solved for by a modified version of the deformation gradient definition where **u** is the displacement vector for a loaded node, (**F**-**I**) is the displacement tensor defined by the user, and **X** is the reference location of the node.

$$\mathbf{u} = \left(\mathbf{F} - \mathbf{I}\right) \cdot \mathbf{X} \tag{24}$$

The logic of whether a displacement is applied $(a = 1)$ or not $(a = 0)$ may be defined as follows, where **M** is the logic tensor with value 1 where a displacement value was modified by the user and 0 elsewhere. The vector location **V** follows the same naming convention as the node labeling used for the application of boundary conditions. This convention has a 0 for the innermost or a 1 for the outermost node along this dimension, e.g. V010 is the node along the y-axis from the origin and V011 is the node at the corner of the face containing the y and z axes. See Figure 17 for further clarification.

$$a = \begin{cases} 1, & \sum_{i=1}^{3} \mathbf{M}_{ij} \mathbf{V}_j > 0 \\ 0, & \text{otherwise} \end{cases} \tag{25}$$

These displacements are then applied to the outermost nodes of the mesh, V000, V001, V010, V011, V100, V101, V110, and V111. Rigid body modes are eliminated by setting the V000 (origin) node to have 0 displacement and the axis nodes (V001, V010, V100) to have 0 displacement out of axis.

The displacement tensor is defined in a normalized manner, with the amplitude ε_a and the load ratio $R_\varepsilon = \varepsilon_{max} \ / \varepsilon_{min}$ being used to find the actual displacement values during loading. Currently the pipeline only supports quasi-static loading with a strain rate of 10^{-3} 1/s. The time for each step is found using this strain rate and the applied strain. Finally, the output request interval may be defined by the user, since this can significantly impact computational time and storage required. These and other loading parameters are displayed for clarity in Figure 16.

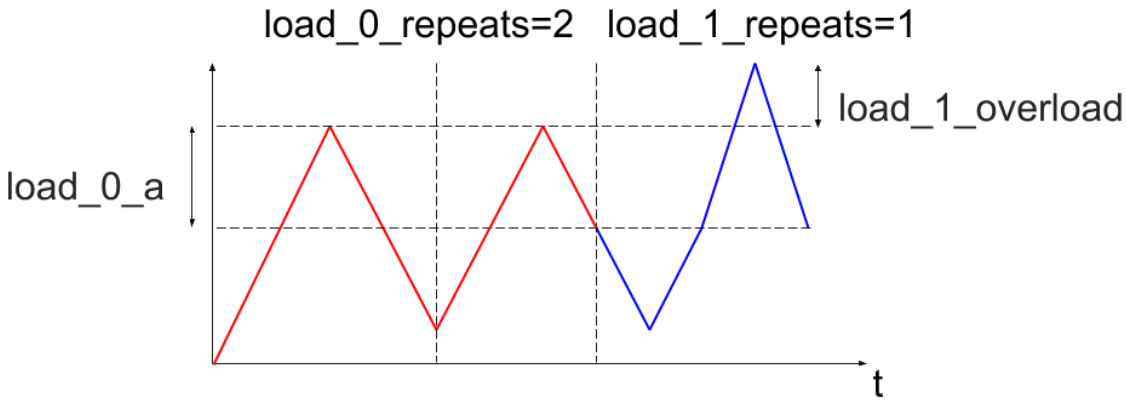

Figure 16. Loading steps and parameters for pipeline execution.

Additional node sets describe opposing faces and edges and are labeled according to a standard used by Przybyla and other previous students of the McDowell group [40, 79] which allows for clear, concise labeling and application of common boundary conditions encountered in crystal plasticity simulations.

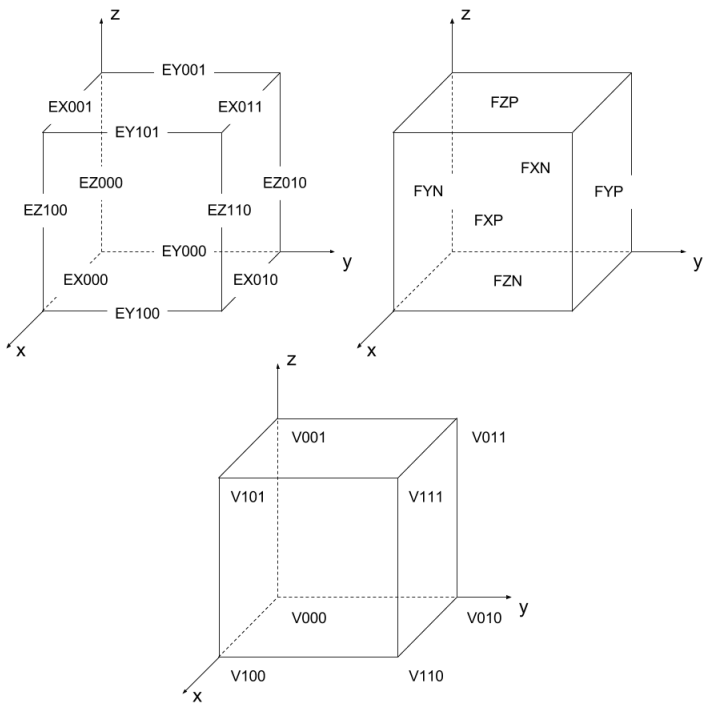

Figure 17. Node sets used for applying loads and boundary conditions.

Currently, several different boundary conditions are supported in the pipeline, in any combination. The currently supported boundary conditions are flat (faces remain parallel to initial orientation), periodic, and free. The periodic boundary conditions are most common to crystal plasticity modelling and are used to emulate the behavior of a subsurface material volume and improve the convergence rate to macroscopic material properties [79, 96]. These boundary conditions enforce equal displacements across opposing faces by the use of zero-valued linear systems of equations (Abaqus boundary condition standard). This condition ensures the deformed volume can be tessellated in the chosen direction, thus the displacements are periodic. This condition should be utilized in conjunction with periodic microstructures.

The zero sum equations require a consistent number of variables, thus, each paired node set must contain an equal number of nodes. For periodic boundary conditions, this has the implication that the periodicity of the boundary conditions should

match the periodicity of the mesh (nodal positions matching across opposite faces). This condition is satisfied for the prismatic meshes used in this work, however, there does exist a general formulation which can be implemented for non-periodic meshes at the expense of significant complexity [97]. Another shortcoming of the current implementation is that all node sets are required to have at least one element such that the boundary conditions do not break. This restriction can be relaxed with additional effort. For additional detail on the equations used to generate periodicity using the listed node sets, see Przybyla [64]. Finally, a list of simulation files is compiled including *main_[0-9]⟨1,⟩.inp*, *loads.inp*, UMAT, and a remote execution script. A Python package, Paramiko [98], is used to ssh to the remote cluster, upload the files, and submit the execution script remotely.

2.2.4: Post-Process

The fourth module, *post_process.py*, is not explicitly integrated into the usual operation of the pipeline. Instead, this module is designed to provide users with a means of analyzing common forms of data generated by crystal plasticity simulations e.g., FIP files. This means that functions are readily available to integrate into user-developed automation suites incorporating the pipeline to facilitate design and automated analysis in one iterative loop. In addition, functions are provided to facilitate plotting common forms of data to reduce redundant efforts.

2.2.5: Pipeline

While the previous modules have been introduced with a logical ordering to the data created and utilized, they do not contain the functionality to automate the execution of multiple crystal plasticity simulations. The functions required to perform these automation tasks are contained in the *pipeline.py* module. The two core functions of this

module are *doe_runner* and *pipeline_runner*. The *pipeline_runner* takes in a Parameter object along with several flow control arguments. This function utilizes the building blocks presented above to prepare crystal plasticity simulations as specified. Upon completion, the current batch will be finished with preparations and either residing solely on the local machine or submitted for simulation on the remote cluster. The other function, *doe_runner*, is the only function to interface directly with user inputs. This function relies upon the existence of a file, DOE.csv, in the root of a directory that determines the specific simulation configurations to execute.

Execution of the pipeline is performed via the command line and the only mandatory argument is the path in which to operate. The final directory in this path becomes a unique identifier of the simulations performed and a matching results directory is created on the remote cluster. A Parameter object is constructed which parses the DOE.csv file and the *doe_runner* iterates over each configuration line, creating simulation files in directories numbered $i = 0,1, \dots, n-1$. For documentation regarding these objects and user parameters, please see the included documentation files. The *pipeline_runner* is executed for each configuration to create a batch of simulations. If the user desires, all of the configurations may be submitted simultaneously in a so called "batch mode" or pause for successful completion of the previous batch. In either case, eventually the *doe_runner* must eventually reach a polling mode. During this mode, the *doe_runner* sleeps for a set period of time (currently 30 seconds) before resuming execution and querying the cluster for the number of simulations in progress. This is accomplished by ssh-ing into the remote cluster and executing a command, which counts jobs remaining in the queue that match the current DOE name. This cycle of sleeping allows for minimal processor overhead while remote jobs are executed so that the user's machine is not negatively impacted. Upon completion of a batch of simulations, the results are downloaded to the local user's machine in the corresponding directory and further post-processing can be performed. This entire process retains traceability without

becoming cumbersome to the user. There is not the high overhead of interfacing with a database and learning a new schema, instead the files are located in a directory of the same name on the remote cluster and the user's local machine. Finally, the selected configuration options are retained in the root directory in the form of the DOE.csv, presenting an easy interpretation of past simulations.

2.3: Material Repositories

In addition to the core pipeline and its repository, each material model supported by the pipeline is also maintained in a standalone repository. Because of this loosely structured approach, there exist some dependencies that are not immediately apparent. These dependencies are highlighted in Figure 18, which also depicts the requisite folder hierarchy of local repositories. Both the pipeline and material repositories must reside in the parent GitHub folder. Currently, material and application paths (e.g. GMSH, Dream.3D, etc.) are expressed relative to the pipeline repository (PythonScripting) to respect user PATH variables and folder structures.

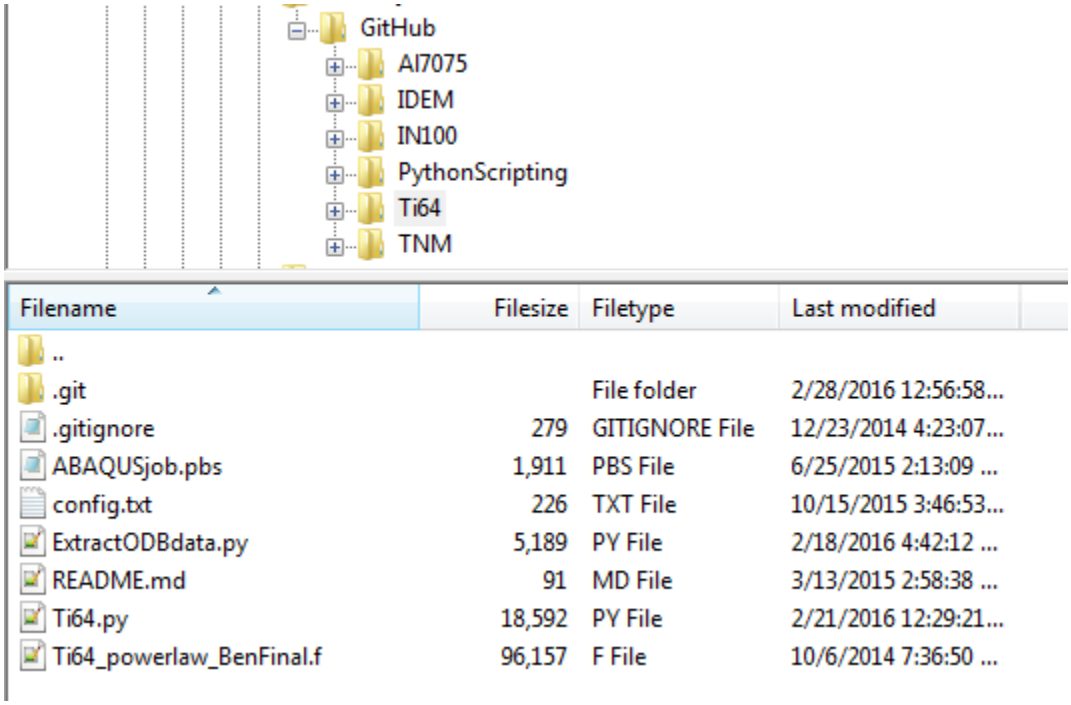

Figure 18. Example material repository structure with required files.

The following files are required in each material repository.

- Material module (Ex. *Ti64.py*): Must be named the same as the material repository. Contains functions to write material information and request SDV outputs to the Abaqus .odb file.
- *config.txt*: Colon delimited list of configuration options loaded before the pipeline prepares simulations for this material. See pipeline.py for use cases of various configuration options. Options for material or general configuration may be seen in the section Summary of Features and Parameters.
- Remote Submission Script (e.g. *ABAQUSjob.pbs*): A template script to execute simulations involving the material model. This needs to include initialization of the module environment, creating a scratch directory, executing the simulation, and extracting any necessary information.

During pipeline execution multiple batches of simulations may be performed. Prior to each batch execution, the requisite material module is loaded from the appropriate repository. The file *config.txt* is also parsed to provide additional parameters and override pipeline defaults where appropriate. This combination allows for extended functionality of the pipeline specific to individual material models and simulation parameters.

2.4: Summary of Features and Parameters

While it is anticipated that the pipeline will continue to grow in function and potentially be restructured, a thorough documentation of the options available to the user to configure simulations is presented as a representative snapshot of the current time. For up to date documentation, see the pipeline repository, and specifically the Parameters object in the pipeline.py module for updated information. The following is a list of

options exposed to the user in the DOE.csv file. The list is broken down by parameters, these are further enumerated by the input type, and an explanation of the current functionality. Each parameter is the heading of a column in DOE.csv. Each batch (row) in DOE.csv can define the option or leave it blank (empty string) to progress with the default option.

- num_runs: Integer
    - Number of microstructure instantiations to simulate with the current parameters
- size: comma separated list of Floats
    - Geometric extents of the microstructure and, if linked, mesh in mm
    - List is in order x, y, z
- shape: comma separated list of Integers
    - Number of voxels in each dimension
    - List is in order x, y, z
- sve_periodic: Boolean, optional
    - Defaults to True
    - Flags Dream.3D to allow periodicity in microstructure instantiation
- sve_banded: Boolean, optional
    - Defaults to False
    - Produces banded mesh and requisite files, see [47, 48]
- sve_band_thickness: Float, optional
    - Required for banded mesh
    - Determines the banding thickness in mm
- mesh: String
    - Determines the meshing type applied
    - Must be one of voxel, tet, or repeat_inp

- ms: String
    - Determine source of microstructure descriptions
    - Must be one of: dream3d, copy_previous, read_existing, or single_crystal(ϕ_1, Φ, ϕ_2)
- mat: String
    - Material repository name to utilize for batch simulations
    - Case sensitive
- load_i_
    - repeats: Integer
    - r: Float
    - msc: Boolean
        - Evaluate MSC cracking via mesoscale or other crack propagation routine at the conclusion of this loading application
    - E_{ij}: Float
        - Relative in-phase loading displacement for the equivalent direction
    - a: Float
        - Strain amplitude in mm/mm

Additionally, the configuration file supports several options which may be used to configure pipeline behavior for the user's specific computer and remote cluster setup. These options may also be redefined in each material repository. The *config.txt* file is a colon-delimited file with the following options:

- *MaxRunningOnCluster*: pipeline repository
    - Courtesy limit to not overload queue and run out of Abaqus tokens
    - Will pause job submission if the current number of jobs exceeds this value
- PiplineRunner_

    - v4: pipeline repository
    - v6: pipeline repository
    - Relative path of the Dream.3D application PipelineRunner to processs synthetic microstructure for the appropriate version number
- gmsh: pipeline repository
    - Relative path of the Gmsh executatble
- Server: pipeline repository
    - Cluster supporting qsub and ssh
- DataMover: pipeline repository
    - Optional remote login which supports faster data download and movement operations
- *IncludeFiles*: material repository
    - Comma separated lsit of files with fixed names that remain constant for all of the microstructures to be simulated in a batch.
- *InstantiationFiles*: material repository
    - Comma separated list of filename 1, extension 1, filename 2, extension 2, … Specific microstructure instantiation numbers are inserted between the filename and the extension during pipeline execution prior to upload for remote execution.
- *UMAT*: material repository
    - UMAT filename in the current folder
- *Pipeline*: material repository
    - Dream.3D pipeline located in this folder, if not included a default pipeline will be run from the pipeline repository.
- *PBS*: material repository
    - Name of the remote submission script located in this directory.

Finally, there are several pipeline options that are supplied as command line arguments. These arguments are:

- b: batch mode
    - executes all lines of the DOE.csv simultaneously
- o: offline
    - Does not attempt to contact the remote cluster
    - Does not upload or execute simulation files
- r: resume
    - repeats the execute of the DOE resuming at the supplied configuration number
- v: verbose
    - Supplies additional information to the user during runtime

2.5: Conclusions

The framework for an automated crystal plasticity simulation pipeline has been presented. While not a formal documentation of the data structures and dependencies, the intent is to provide a brief introduction and point interested users to the formal, up to date documentation on the Github repository. The intent of this pipeline is to streamline simulation and development of new capabilities within the McDowell group and beyond. The scripting tools provided here and flexible structure should facilitate reduced startup time. Future chapters will not explicitly mention the use of the pipeline, however it should be apparent that the amount of data generated and analyzed was greatly facilitated by the use of the pipeline. All simulations and material models used in this work are supported within this framework. The compilation of such resources should significantly reduce the effort required to add data to existing simulation studies and build additional features to improve model fidelity and data analysis rigor.

CHAPTER 3: SENSITIVITY ANALYSIS OF FATIGUE IN CRYSTAL PLASTICITY MODELS

3.1: High Cycle Fatigue as an Extreme Value Problem

One of the most important research efforts in quantifying fatigue processes is that of Freudenthal and Gumbel [99], interpreting fatigue damage processes as a continuous survival function. This survival function expresses the cumulative frequency of the number of surviving samples as a function of the number of cycles. Obtaining statistically significant numbers of fatigue specimens is costly due to extensive experimentation required. Instead, modeling approaches have been introduced to facilitate the understanding of fatigue in terms of extreme value distributions. Many researchers have attempted to relate fatigue lives to distribution of initial defects [100-103]. Other efforts have considered competing fatigue mechanisms to explain increased life scatter and differences in observed fatigue behavior [36, 104, 105].

One particular method of fatigue analysis using crystal plasticity simulations that has become increasingly prevalent, especially within the McDowell group, is the use of FIP based extreme value statistics gathered from the ensemble of SVE. The FIP response is calculated for all locations in the FEM mesh, with the maximum FIP from each SVE then compiled into a list of maxima. This concept of selecting extrema from equal sized samples forms the basis for extreme value theory. In the derivation by Gumbel [106], individual samples X_i are independently identically distributed (IID) from a known cumulative distribution function $F_X(x)$ which may be referred to the as the underlying distribution in this work. The following formulations will only consider the extreme value theory in terms of the life limiting (maximum) values. For an ensemble of n SVE, the maximum Y_n is expressed

$$Y_n = max\left(X_1, X_2, \ldots, X_n\right) \tag{26}$$

where X_1 to X_n are the individual SVE maximum FIP values. The cumulative distribution F_{Y_n} expresses the probability of finding a Y_n less than the value y.

$$F_{Y_n} \equiv P\left(Y_n \le y\right) = P\left(X_1 \le y, X_2 \le y, \ldots, X_n \le y\right) \tag{27}$$

Finally, for univariate distributions, it has been shown that there are three extreme value distributions to which this extreme value distribution can converge [107]. The set of all distributions for which the tail behavior converges to one of these three distributions is referred to as the domain of attraction for that distribution. Przybyla [64] studied the behavior of the ensemble FIP maximum introduced above. The Type III, or Weibull, extreme value distribution was deemed inappropriate to fit given the inability to define a true maximum response value [39]. The Type I Gumbel distribution was found to better fit the extreme behavior of various FIP values when compared to the Type II Fréchet distribution [108]. The probability density function (PDF) of a Gumbel distribution is given by

$$F_{Y_n}\left(y\right) = exp\left[-e^{\frac{-1}{\sigma_G}\left(y-\mu_G\right)}\right] \tag{28}$$

where μ_G is the characteristic largest value of X_n and σ_G is a measure of dispersion. Both values may be fit with a least-squares regression after transforming the data with natural logarithms [60]. Such a transformation is also useful for plotting and verifying the goodness of fit for the Gumbel distribution to the extreme value observed. The linear transformation for the Gumbel distribution is of the form

$$-\ln\left[-\ln\left(F_{Y_n}\right)\right] = \frac{1}{\sigma_G}y - \frac{\mu_G}{\sigma_G} \tag{29}$$

which is useful for plotting the distribution linearly and performing regression. MATLAB [109] was used to provide confidence intervals of the fitted parameters using maximum

likelihood estimation (MLE). These fitted parameters may then be correlated with microstructure parameters, marked correlation functions, and fatigue responses to guide engineering design based on the probability of extreme events.

Within this framework of extreme values, there are several mechanistic justifications for various averaging volumes. Shenoy et al. [43] indicate the applicability of FEM volumes on the order of slip bands to be valid for conducting fatigue simulations. Castelluccio and McDowell [46] also observed slip band and grain size averaging volumes and their impact on FIP values, noting that the maximum values tend to occur near grain boundaries. Diard et al. [59] utilized an averaging volume of approximate grain size but which did not extend into the neighboring grains. Due to these observations, several different averaging schemes will be investigated to ascertain their effect on the extreme value responses.

3.2: Sensitivity Analysis Procedure

While the use of SVE and FIP extreme distributions has begun to permeate the literature, little effort has been expended to understand how the selected simulation parameters influence decision making for fatigue resistance. In the existing literature, SVE size has been selected based on a justification of convergence of local plastic strain response and cyclic FIPs. While it has been demonstrated at the single SVE level that these values do not reach convergence [60], the impact on extreme value distributions has been thus far neglected. Establishing a knowledge base regarding the behavior of FIPs, extreme value decision-making, and comparative strategies becomes increasingly important as design for fatigue resistance expands in scope and research is conducted by and across different groups. While single studies tend to compare fatigue response for varied materials across a constant set of simulation parameters, there is the potential for independent researchers to desire to correlate results across different literature sources that have utilized varying simulation parameters. This work aims to inform this ability to

standardize information exchange and explore the limitations of extreme value FIP analysis over a range of simulation parameters.

All meshes in this study will be cubic to reduce dimensionality of the design space. This assumption matches many simulations conducted using crystal plasticity models because specimen geometry is not considered, and it is instead desirable to measure the bulk response. Measuring the bulk response is also facilitated by the use of the aforementioned periodic boundary conditions. This assumption is also necessitated by the work of Przybyla et al. [108], who demonstrated that the application of the Gumbel distribution to extreme value analysis of FIPs is only valid in the case of periodic boundary conditions. Traction free surfaces greatly change the deformation at the boundary and thus present differing regions of FIP responses, which breaks down some of the assumptions inherent in the extreme value analysis. These boundary conditions can also introduce competing mechanisms of fatigue that are not investigated in this study. Instead, the intent is to understand, for subsurface volumes, the variation of extreme value distributions from simulation parameters.

An initial investigation was funded by Dassault Systèmes Simulia Corp to study the impact of different simulation parameters. This investigation used a Latin Hypercube DOE over a larger parameter space than the one presented in this work. This fact, coupled with the inclusion of strain amplitude as a variable in the DOE, contributed to relatively high uncertainties and made drawing definite conclusions impossible. This work addresses some of the previous shortcomings by analyzing the responses over a Full Factorial DOE for the following parameters.

The first sensitivity parameter δ is the number of average grain diameters along the SVE sidelength. This parameter is commonly used in RVE convergence studies to represent the number of nearest neighbor effects necessary to obtain convergence. This parameter also serves as a proxy measurement for the total number of grains in the simulated volume. Increasing number of grains will improve fitting of the

crystallographic orientation, misorientation, and grain size distributions. This parameter is used such that the conclusions should be independent of the grain size studied.

The second parameter E_g is the number of voxels across an average grain diameter. Again, this is a linear parameter intended to represent potential strain gradient effects developing within grains as the mesh undergoes refinement. This parameter has been investigated by Castelluccio and McDowell [110] for a limited set of SVE, but not at the ensemble level. Again, this value is held constant for all three spatial dimensions, and a normalized value chosen to reflect the general applicability of the results to any grain size and mesh size.

The applied strain amplitude ε_a is the final parameter for this investigation. Different applied strain amplitudes are desired since strain localization has been observed to be a function of the applied strain, i.e., as applied strain increases, the heterogeneity of plasticity tends to decrease. This transition has been linked to the scatter in fatigue lives associated with HCF and ultimately the transition to LCF and more homogenous plasticity. To study these effects, two loading conditions were modeled for each material system. One, to represent VHCF, is chosen as $0.35\varepsilon_y$ and the other, for HCF, is selected as $0.7\varepsilon_y$ where ε_y is the strain at macroscopic yield. If observations are consistent across the widely varying plasticity regions encompassed by these loading conditions, it may be reasonably assumed that they are consistent conclusions across the parameter space relevant to fatigue simulations. To limit the size of this initial investigation, all loads are fully reversed $R_\varepsilon = -1$. All loads are applied for three cycles to approximate steady state values [39].

For consistency of language, a "configuration" is a unique combination of the above parameter values. In addition, two different types of sensitivity studies were conducted. The first type utilizes the subsampling routine discussed previously to conduct simulations across the range of configurations while utilizing ostensibly the "same"

microstructures. The idea of this study is to provide a baseline by reducing the aleatoric uncertainty associated with the number of samples in each batch. A Kolmogorov-Smirnov (KS) test was used to test whether the distributions of FIPs were drawn from the same distribution for all configurations of a given type (same, unique). For both materials studied, the "nominally same" simulations were more closely related for all but one of the configurations examined. For this reason, unless otherwise noted, the batches referred to in the results are from the "nominally same" microstructure simulations.

Table 1. KS test statistics for "nominally same" and "uniquely generated" microstructure batches compared to the highest fidelity reconstruction (Configuration 9).

	Ti64			IN100	
	ε_a=0.35ε_y	ε_a=0.35ε_y	ε_a=0.7ε_y	ε_a=0.7ε_y	ε_a=0.35ε_y
Configuration #	Uniquely Generated	Nominally Same	Nominally Same	Nominally Same	Uniquely Generated
1	5.28E-02	2.24E-02	2.02E-02	1.52E-01	3.12E-01
2	6.35E-02	1.89E-02	1.37E-02	8.13E-02	3.09E-01
3	3.56E-02	1.97E-02	1.48E-02	9.25E-02	2.43E-01
4	3.18E-02	9.07E-03	2.20E-02	7.61E-02	3.04E-01
5	2.17E-02	8.43E-03	1.19E-02	8.12E-02	2.36E-01
6	6.28E-03	8.89E-03	6.08E-03	2.44E-02	6.51E-02
7	3.48E-02	2.38E-03	2.17E-03	6.72E-02	2.44E-01
8	1.57E-02	1.57E-03	1.38E-03	6.10E-02	8.60E-02
9	0.00E+00	0.00E+00	0.00E+00	0.00E+00	0.00E+00

Two different material systems will be investigated to ascertain the general applicability of the results presented here as well as any discrepancies. For each material system, several response variables will be considered. The first response is the coefficient of variance for the stress observed at the peak imposed strain. The coefficient of variation is a standard statistical measure for a normally distributed property and may be expressed by the ratio of the standard deviation to the mean

$$c_v = \frac{\sigma}{\mu} \tag{30}$$

where σ is the standard deviation of the variable in question and μ is the mean. Since this variable will be used to quantify many relative uncertainties, the subscript will denote the variable of interest, e.g. c_σ is the coefficient of variation for the peak stress. This is similar to many macroscopic convergence measures used in other sources [111, 112].

In addition, the extreme value distribution parameters and their coefficient of variation will be studied for distributions fitted to extreme values arising from different averaging schemes. Przybyla [64] demonstrated the reduction in sensitivity of extreme value distributions by averaging over a grain-size-equivalent volume. These volumes should be determined by the damage process relevant to the material, e.g., slip bands in recent work by Castelluccio [40]. The importance of this consideration is also noted by Shenoy et al. [43]. The first type of value reported is the "element" FIP with Gumbel parameters $\mu_{element}$ and $\sigma_{element}$. Since reduced integration elements (C3D8R) are used for all of the studies in this work, this computation is performed at the single integration point in the center of each element. The second type of averaging volume discussed is a "grain equivalent volume" with parameters μ_{kernel} and σ_{kernel}. This volume is averaged by using a Gaussian kernel with the standard deviation set such that two standard deviations on each side will average over the mean grain diameter. A coarser application of grain equivalent averaging volume may also be applied in the form of cubic volumes with the number of elements selected to approximate the average grain diameter. Parameters for this averaging method are μ_{cube} and σ_{cube} The final averaging type, "grain averaged," is the mean response over all elements in each grain with parameters μ_{grain} and σ_{grain}.

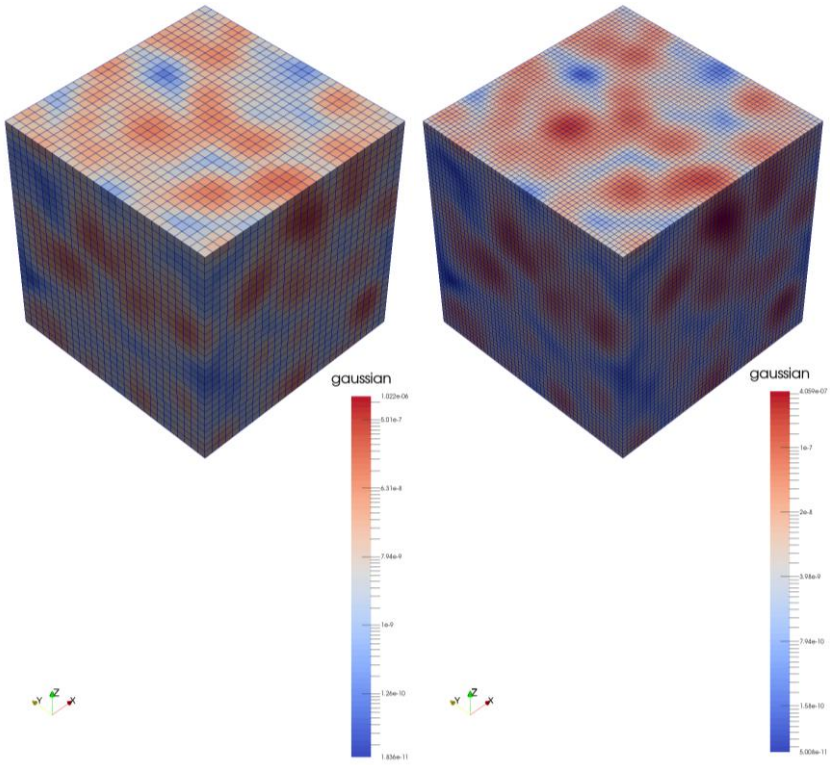

Figure 19. FIPs averaged over grain equivalent volumes for two representations of the same nominal microstructure.

SVE parameter selection will inherently generate a non-constant number of FIP responses from which to select the maximum. Since extreme value distributions are fundamentally linked to this sample size, it is relevant to observe the response variable behavior before and after adjusting for this statistical effect. The term observation window will be used to differentiate this sample size from other sampling sizes involved in this work. This term, often used for observation of particles or voids in steel assessment, is equivalent to the observation time frame in extreme wind measurements, and several sources note a procedure for adjusting the extreme value distribution to account for differing observation windows. While this procedure can be found in several sources, the formulation used by Beretta et al. [104] is reproduced below for consistency in extreme value fatigue failure applications. First, the ratio of the observation sizes is expressed as

$$V = \frac{Y_{02}}{Y_{01}} \tag{31}$$

where Y_{02} and Y_{01} are the sizes of the observation windows and V is the size ratio. The redefinition of the actual Gumbel distribution must necessarily be expressed as

$$F_{Y_{02}}(x) = \left(F_{Y_{01}}(x)\right)^{V} \tag{32}$$

conditional on the independence of the observation windows, and the individual samples contained within. This results in a shift of

$$-\ln\left(-\ln\left(F_{Y_{O2}}(x)\right)\right) = -\ln(V) - \ln\left(-\ln\left(F_{Y_{O1}}(x)\right)\right) \tag{33}$$

for plotting the distributions of the extremes in a linear fashion. Gumbel parameters adjusted in this manner will be referred to as "adjusted" distribution parameters. All adjusted distributions are constructed with some "target" observation window size that will depend on the type of value used to construct the extreme value distribution. Selection of target sizes is discussed further alongside the results.

3.3: Ti64 Case Study

The first material system observed is the Titanium alloy Ti-6Al-4V (Ti64) using the power law model calibrated by Smith [113]. The reader is referred to the work of Smith for additional details on the implementation of the crystal plasticity model and material system. This study simulates the β-annealed microstructure with random texture, which will simply be referred to as Ti64 in this work. A log-normal grain size distribution was also applied for this material system with $\mu_{\ln} = 4.064$ and $\sigma_{\ln} = 0.2462$ such that the average grain size is 60 μm and the standard deviation is 15 μm as determined by Smith [113], i.e.,

$$f(x) = \frac{1}{x\sigma_{\ln}\sqrt{2\pi}} \exp\left(-\frac{(\ln(x) - \mu_{\ln})^2}{2\sigma_{\ln}^{\ 2}}\right) \tag{34}$$

A full factorial DOE was selected to capture any potential interaction effects between the parameters and allow for response surface construction. The selected configurations are shown in Table 2. Example microstructures for each configuration can be seen in Figure 20 to demonstrate the subsampling in three dimensions as well as the effect of varying the two variables studied. Twenty microstructures were simulated for each configuration. This is near the limit observed by Przybyla and McDowell [60] as having good agreement with the extreme value distribution. Following simulation, this was found to be a sufficient number of SVE for all configurations.

Table 2. List of configurations for the Ti64 sensitivity DOE.

Configuration #	Nominal number of grains per SVE sidelength δ	Elements per average grain diameter E_g
1	3	4
2	3	5
3	3	7
4	5	4
5	5	5
6	5	7
7	7	4
8	7	5
9	7	7

The first parameter c_σ is very well behaved. For both the high and low strain cases, this variable decreases with increasing δ and shows no trend in E_g. Indeed, the behavior is well fit by several other studies of macroscopic stiffness convergence such as that of [70]. These results are entirely anticipated as they exhibit features observed by many researchers about the convergence of stress/strain response as a function of SVE

size such as Barbe et al. [67] whose results indicate a relative insensitivity of the stress/strain distributions to the mesh refinement for a constant SVE volume. Extensive analysis is not presented on the c_σ response since this has been well studied in the literature, instead this was predominantly used to verify the general trends in the SVE reconstructions and simulations. Data is included in APPENDIX B.

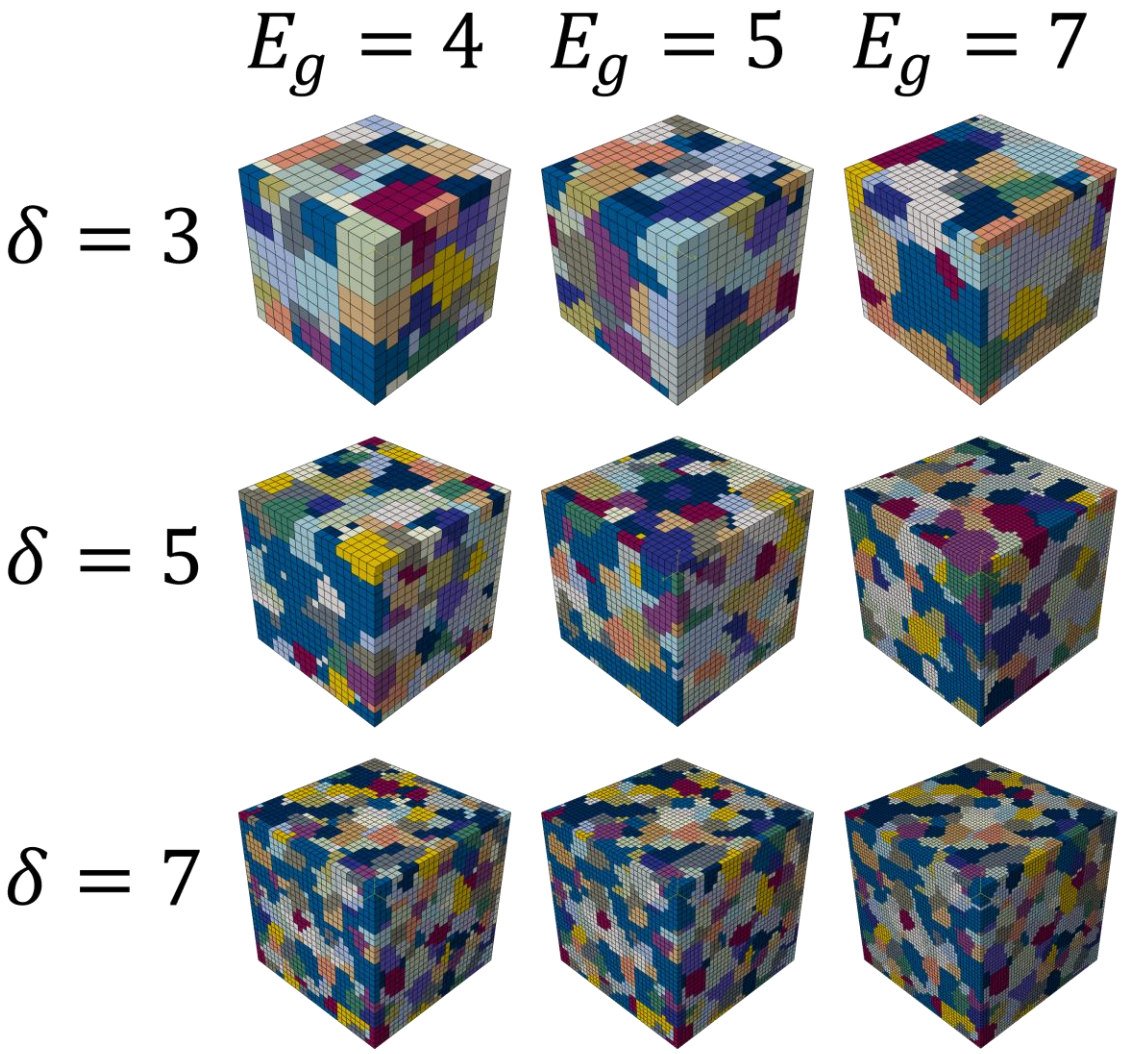

Figure 20. Example meshes for nine configurations of Ti64 sensitivity DOE.

Less well studied is the fatigue value sensitivities with respect to simulation parameters. Unfortunately, the Gumbel distribution parameters are not particularly well

behaved in raw or adjusted form. For all of the extreme FIPs studied, the distribution parameters are outside of the 95% confidence bounds of at least one other simulation configuration. This is also true of the adjusted distributions. Due to the large number of responses considered, representative responses are selected for reproduction here. All error bars plotted are the 95% confidence interval for each parameter as estimated from the MLE routine.

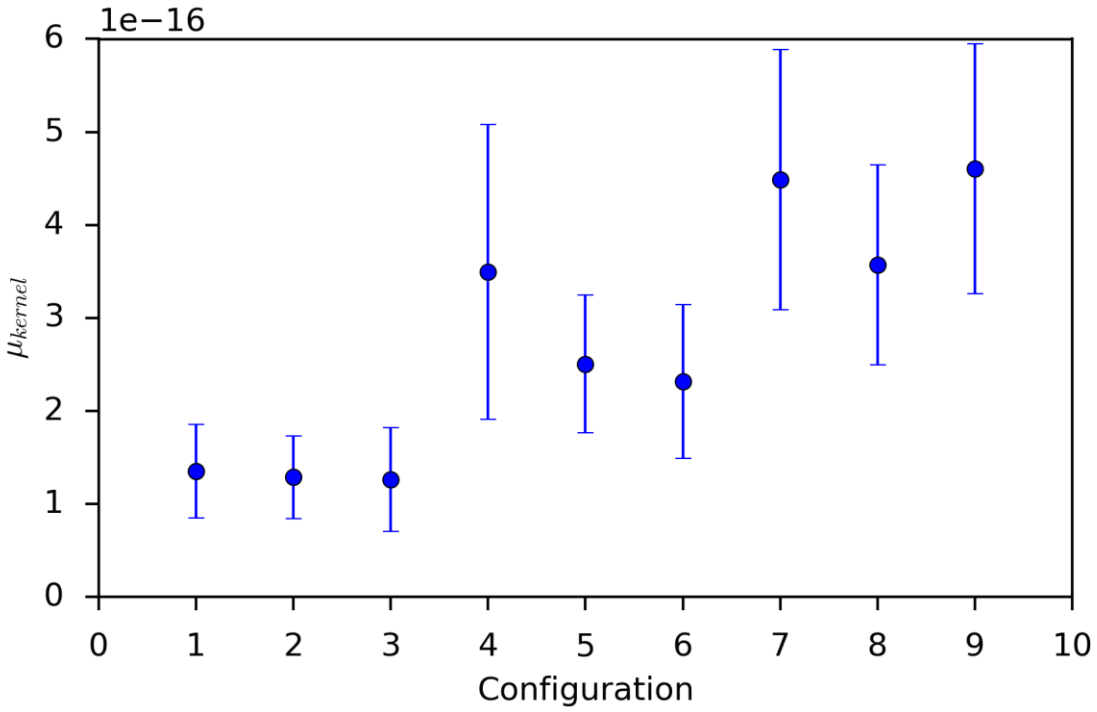

Figure 21. Behavior of μ_{kernel} from Ti64 simulations at $\varepsilon_a = 0.35\varepsilon_y$.

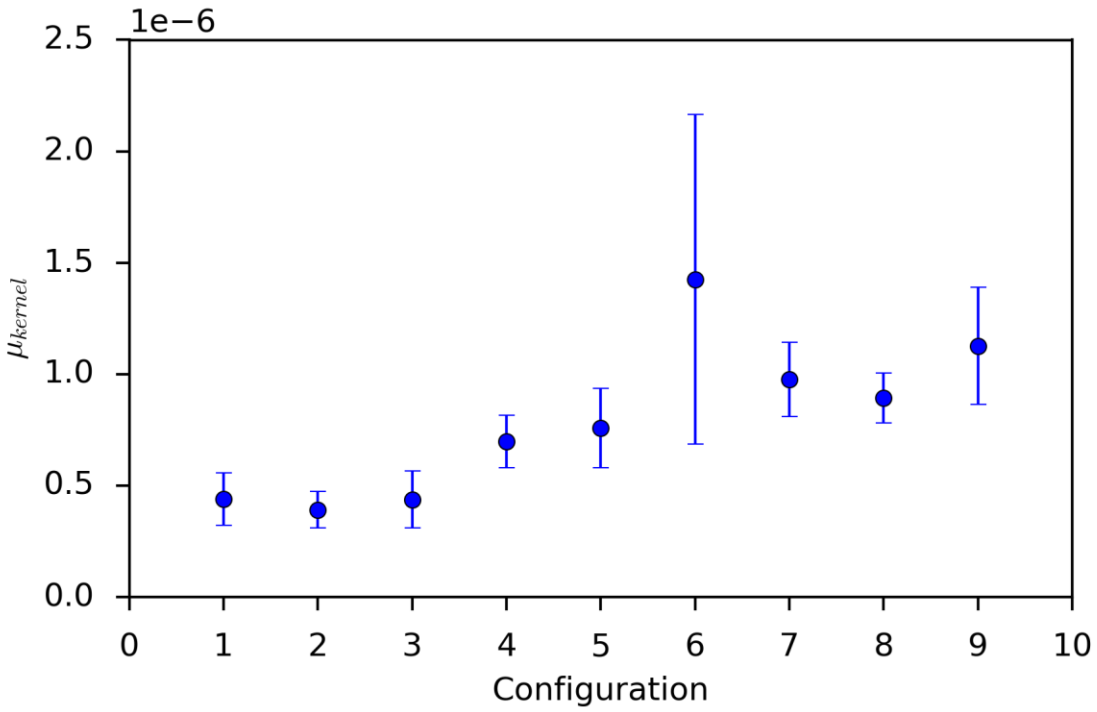

Figure 22. Behavior of μ_{kernel} from Ti64 simulations at $\varepsilon_a = 0.7\varepsilon_y$.

Correction using the statistical methods previously introduced does not adequately shift the distribution values, and in fact creates many problems in the data set. In addition to providing poor agreement with the reconstructed mean, the statistical adjustment for sample size does not explain the observed shift in the σ_G parameter as demonstrated in Figure 23. These variations can be significant (on the order of the variations in μ_G) and not explained simply by a change in sample size. This would tend to indicate a violation of the underlying assumptions.

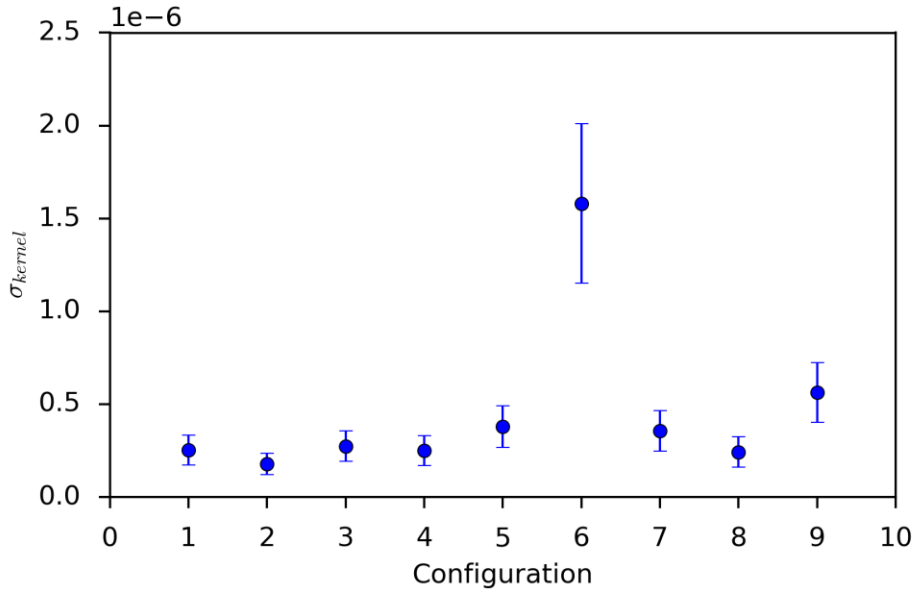

Figure 23. Behavior of σ_{kernel} from Ti64 simulations at $\varepsilon_a = 0.35\varepsilon_y$.

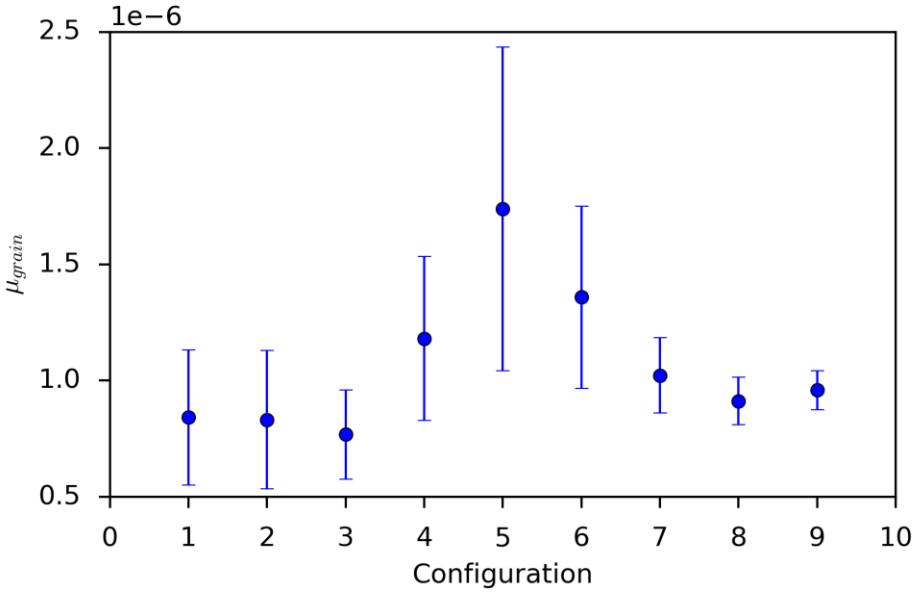

Figure 24. Behavior of μ_{grain} from Ti64 simulations at $\varepsilon_a = 0.35\varepsilon_y$.

Of particular interest is the response of the grain equivalent averaged FIPs. These results provide a significant challenge in analyzing in the extreme value framework as the assumption of IID samples from the underlying distribution is now violated. This

indicates that the adjustment of observation window should instead account for the averaging volume. For the nominally same microstructures it appears that the subsampling method leaves a larger than desired number of small grains. By contrast, the uniquely generated microstructures have a nearly constant packing factor relative to the number of cubic grains in the space. Note that the results are presented using only the average values for the 20 microstructure instantiations; however, the actual number of grains fluctuates from sample to sample which makes the selection of an observation window for correction more difficult.

Table 3. Number of grains observed in nominally same and uniquely generated microstructures.

Configuration	Number of Cubic Grains	Average Number of Grains (Nominally Same)	Average Number of Grains (Uniquely Generated)
1	27	92.3	51.9
2	27	104	51.8
3	27	116.5	52.25
4	125	337.8	237.95
5	125	394	232.85
6	125	398.9	239.45
7	343	652.25	645.9
8	343	652.25	639.25
9	343	652.25	651.05

Using the expected or actual grain numbers, it is apparent that the strategy does not fully compensate for the differences in extreme value distributions. For instance, the conclusions are different depending on the target window size. This is due to the non-constant σ_G term which should nominally be the same for extreme values distributions constructed from IID samples of the same underlying distribution. This presents a significant complication in successfully adjusting the distributions to a target size.

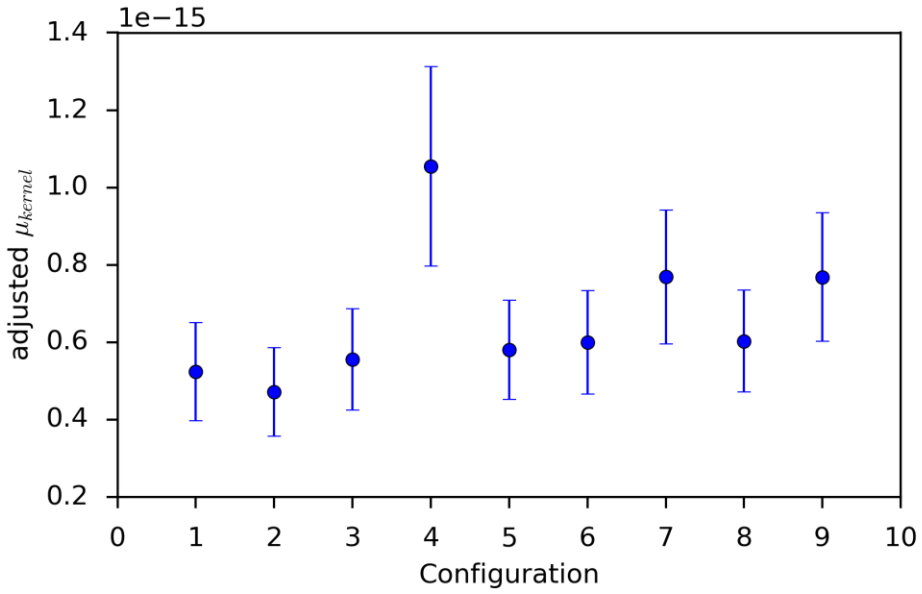

Figure 25. Behavior of adjusted μ_{kernel} with target size of 1000 grains. Samples from nominally same Ti64 microstructures at $\varepsilon_a = 0.35\varepsilon_y$.

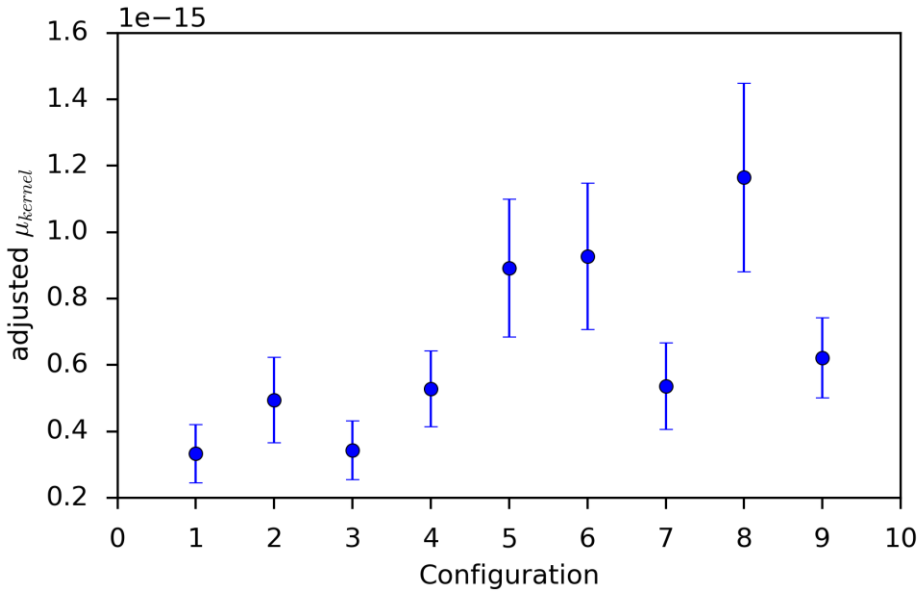

Figure 26. Behavior of adjusted μ_{kernel} with target size of 1000 grains. Samples from uniquely generated Ti64 microstructures at $\varepsilon_a = 0.35\varepsilon_y$.

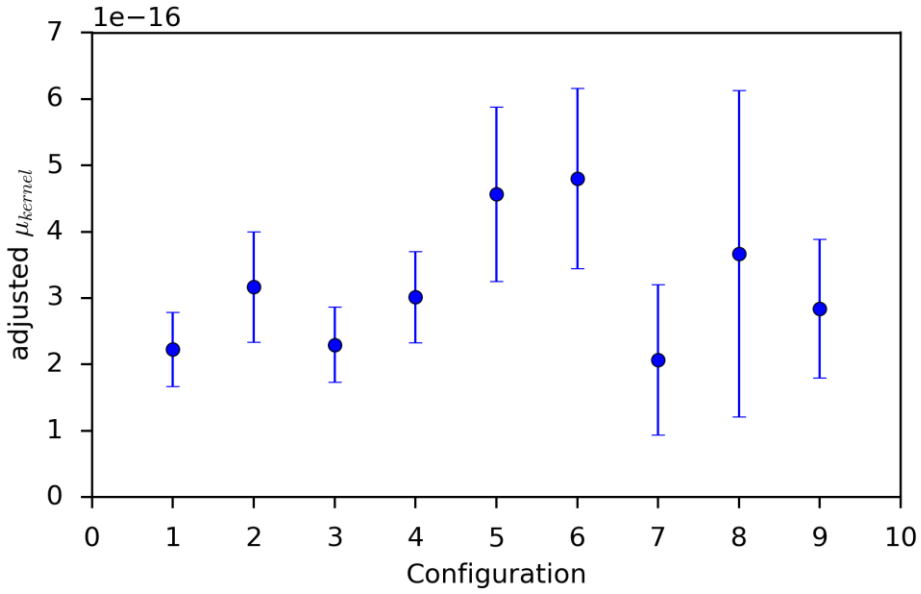

Figure 27. Behavior of adjusted μ_{kernel} with target size of 200 grains. Samples from uniquely generated Ti64 microstructures at $\varepsilon_a = 0.35\varepsilon_y$.

To understand the role of uncertainty in informing potential decisions, the coefficient of variance was also studied for each simulation configuration. This response has relatively little sensitivity to the selection of simulation parameters, indicating that the convergence of the extreme value distribution is not strongly linked to the SVE over the ranges of parameters studied. This is encouraging as it indicates that fundamental changes in the SVE behavior are not occurring and that the relatively inexpensive simulations may be equally representative of the fatigue response. In general, all values for c_x remain relatively constant across all configurations. The one exception for Ti64 is depicted in Figure 28 which shows a very slight reduction of ~10% with an increasing number of elements.

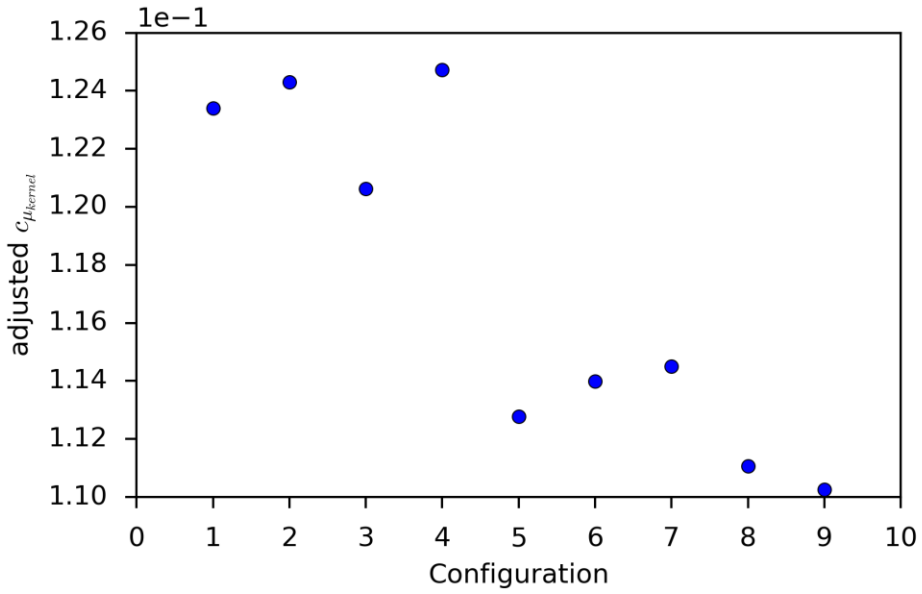

Figure 28. Behavior of adjusted $c_{\mu_{kernel}}$ with target size of 200 grains. Samples from uniquely generated Ti64 microstructures at $\boldsymbol{\varepsilon_a = 0.35\varepsilon_y}$.

3.4: IN100 Case Study

The second material studied in this work is the Nickel-base superalloy, IN100. This alloy is commonly found in aerospace turbine applications. Details on modeling efforts and material features may be found in [43, 49, 60]. A log-normal grain size distribution was also applied for this material system with $\mu_{\ln} = 2.9895$ and $\sigma_{\ln} = 0.1115$ such that the average grain size is 20 µm and the standard deviation is 4 µm as utilized by Przybyla [64]. The maximum values of the δ and E_g parameters were reduced slightly since the material model proves significantly more computationally intensive than the previously studied Ti64 model.

Table 4. List of configurations for the IN100 sensitivity DOE.

Configuration #	δ	E_g
1	3	4
2	3	5
3	3	6
4	4	4
5	4	5
6	4	6
7	5	4
8	5	5
9	5	6

The conclusions of the IN100 investigation are very similar to those of the aforementioned Ti64 study. That is to say, the Gumbel parameters do not display significant, nor consistent correlation to the parameters studied. Similarly, the statistical adjustments for number of observations do not account for the differences in Gumbel parameter values. Again, several plots are reproduced below as representative samples and the remainder of the data is presented in APPENDIX B.

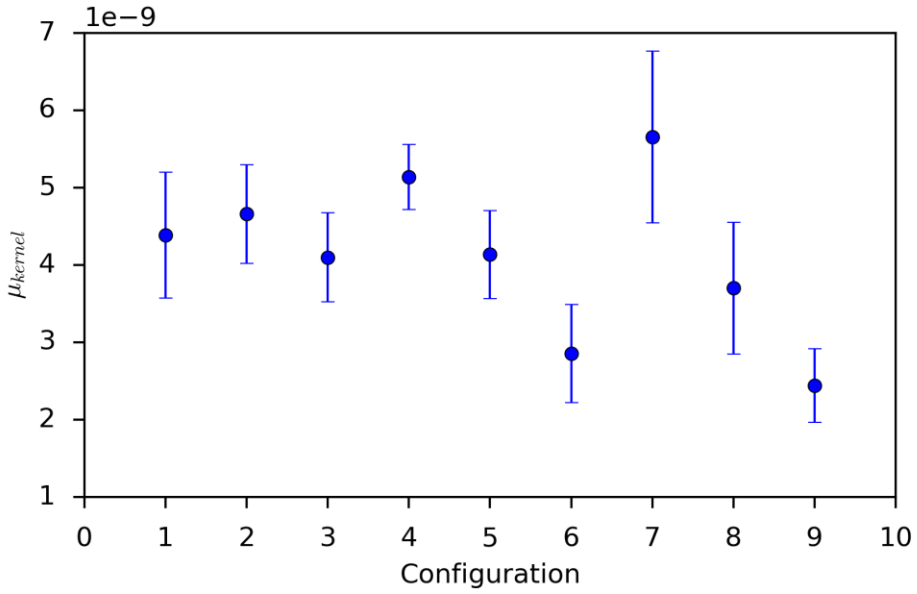

Figure 29. Behavior of μ_{kernel} from IN100 simulations at $\varepsilon_a = 0.35\varepsilon_y$.

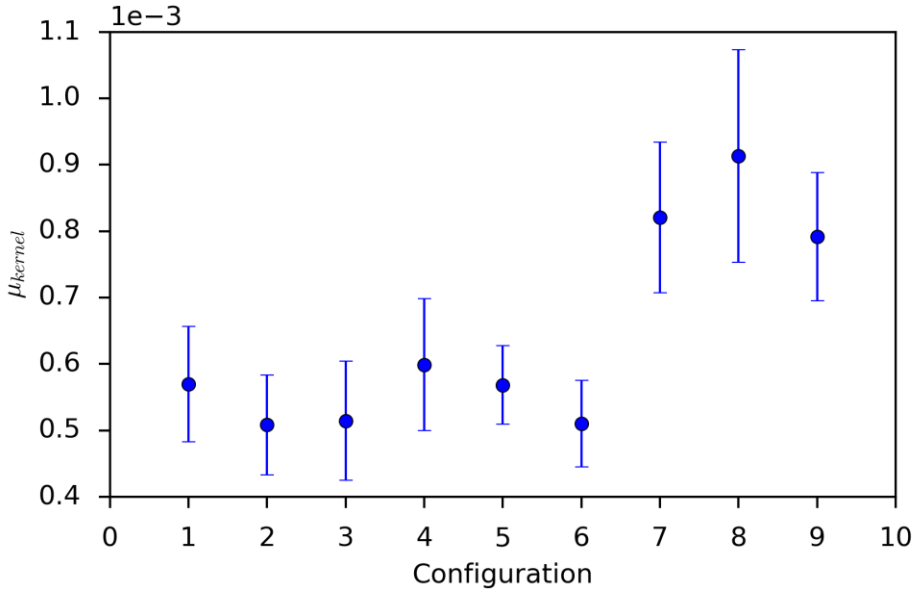

Figure 30. Behavior of μ_{kernel} from IN100 simulations at $\varepsilon_a = 0.7\varepsilon_y$.

In the particular response highlighted in Figure 29 and Figure 30, opposite trends are observed for the high and low strain cases. In this case, it is likely that in the low strain case, plasticity is only being developed at the grain boundary, and thus adding

elements in the interior of the grain suppresses the total response. The statistical adjustment will not account for this difference, e.g. assuming a target size greater than the current number of samples, the adjustment magnitude will be smaller if the number of samples (elements in this case) is closer to the target.

3.5: Conclusions

This chapter presented the results of sensitivity analysis for the extreme value problem of fatigue as applied to two material systems. For both IN100 and Ti64 systems, direct relationships between simulation parameters δ and E_g to Gumbel distribution parameters do not appear viable given the seemingly random occurrences of outlier values. The inability to provide consistent correlations for these responses as a function of simulation parameters indicate the presence of additional confounding variables, which should be further investigated. In addition, the relative uncertainties of the extreme value distributions constructed do not appear to have significant correlation with any of the variables studied. In other words, while the scale and location (σ and μ) variations are not well understood, the extreme value distributions they describe are well behaved for all SVE sizes studied. This indicates that the SVE size and mesh density necessary to construct an appropriate extreme value distribution are satisfied in the region studied and no additional benefit is obtained from this perspective by increasing computational effort. It is noted that these observations were obtained for equiaxed grains with random texture, the simplest of morphologies.

In addition to the analysis of Gumbel distribution parameters as fitted to SVE extreme FIP values, statistical adjustments were performed to these values to correct for the inherent differences in the extreme value sample size (number of elements/grains) by shifting the location parameter μ according to a selected target sample size. These adjustments are relatively standard in the realm of extreme value statistics; however, they do not yield correct results when applied to the extreme value distributions constructed in

this study. Gumbel distribution parameter orderings for the nine configurations studied were observed to differ based on the target adjustment size. These results are not indicative of a fundamental fatigue response for the material of interest. Instead, consistent conclusions cannot be drawn for different SVE configurations in these material systems. It should also be noted that changes in grain morphologies, e.g. increase in grain size, may change the parameters δ and E_g for a constant SVE configuration, and thus particular care should be taken in drawing conclusion for fatigue resistance as a function of the material morphology and texture. As observed, large fluctuations can occur and provide erroneous conclusions for extreme value distributions constructed from SVE maximum FIP values in these cases. This motivates a different approach to quantifying the extreme value behavior, one that is based on an invariant property of the selected microstructure and material model.

CHAPTER 4: MESH INSENSITIVE METHOD FOR APPLYING EXTREME VALUE FATIGUE LIFE ESTIMATES

4.1: Convergence of FIP Distribution

One of the most important assumptions for the convergence of an extreme value distribution is that all samples are selected from the same underlying distribution. For reference, see the introduction in High Cycle Fatigue as an Extreme Value Problem. This underlying distribution dictates the form of extreme value distribution obtained in the limit as the sample size increases [114]. Rankings of fatigue resistance should ultimately be based on this underlying distribution, ideally an invariant response of the material for a consistent loading and sufficiently converged mesh. Similar distributions have been used in various fatigue analysis methods, e.g., the fatigue assessment proposed by Wormsen et al. [115] for a loaded component experiencing spatially varying stresses. This approach considered the volumetric probability of the number of defects in conjunction with the probability of stresses exceeding the critical stress dictated by the defect density. By assessing the life limiting behavior as a function of both probabilities, the overall probability of part survival may be estimated.

Additionally, while works such as [39] and [113] have treated FEM simulations as SVE and captured extreme values for comparison, little effort has been made to characterize the FIP distributions and apply a formal definition for which microstructure meshes may be considered suitable SVE of fatigue response. Many research efforts have instead considered the convergence of local plasticity, maximum averaged FIP value, or macroscopic response in the determination of SVE simulation size [60, 116]. These approaches follow logically from the formal definition of the RVE by Hill [74].

Several other works, however, have directly addressed the distribution of damage criteria. Shenoy et al. [43] computed such a distribution for a limited set of simulation of

IN100 for the purposes of a life distribution prediction. Trias et al. [78] considers the distribution of stress/strain field of composites as additional convergence criteria to the Hill condition. Diarde et al. [59] and Barbe et al. [67] studied the stress distributions of crystal plasticity models as a function of the SVE size and mesh resolution. Distributions were found to have good agreement down to a resolution such that each grain was only represented by a single element. Castelluccio and McDowell [46] also made general observations about the distribution of FIPs using various averaging schemes and under various levels of refinement. Coarse microstructure representations were generally concluded to be acceptable for use in crystal plasticity models given the lack of treatment of grain boundaries and slip bandwidth. These results were not used to make any statement about the appropriateness of the coarsely meshed volumes as SVE, nor the transition towards an RVE with increasing volume. A more formal discussion of the role of SVE and RVE definitions and characterization of FIP behavior as applied to extreme value problems is warranted, however. Applying the notion of an RVE as a function of the FIP distribution logically yields the following:

- The RVE of fatigue represents the volume for which the FIP distribution is entirely representative of the population.
- A volume should be considered an SVE of fatigue if an ensemble of these volumes estimates the true FIP distribution without diverging, but instead remains within a small neighborhood of the true distribution as additional SVE are added to the ensemble.

This first statement is likely to require infeasibly large computational volumes as discussed in the introduction to Synthetic Microstructures and Statistical Volume Elements. The second statement is an intentionally weak claim given the lack of information about various factors influencing the potential distribution of FIPs, e.g. grain boundary treatments, mesh refinement, n-neighbor effects, etc. Both statements can be examined within the context of the previously discussed FIP distributions from sensitivity

analysis of extreme value distributions. Additional FIP distributions, generously provided by Matthew Priddy and funded by NSF GOALI Program (CCMI-1333083), will also be utilized in the following discussion. This database consists of four textures and three loading conditions of uniaxial strain along the x, y, z SVE axes at $\varepsilon_a = 0.5\%$. Each load condition and texture was simulated for 100 instantiations of 21^3 elements. The considered textures are Basal, Transverse, Random, and Actual (taken from EBSD scans of Ti64). FIP distributions referenced are taken over grain-size equivalent averaging volumes using a cubic averaging method.

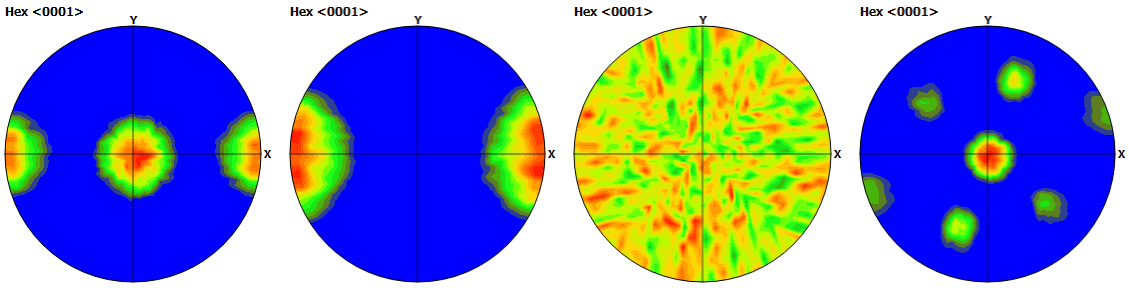

Figure 31. Example pole figures for the (from left to right) Basal, Transverse, Random and Actual textures utilized in this work [113]. Note that pole figure axes are labelled according to SVE axes for comparison to applied loading.

Unless otherwise noted, all distributions shown are the empirical cumulative distribution function (CDF) estimated from element averaged FIPs for reduced integration elements (C3D8R). The Kaplan-Meier estimator is used to construct the CDF. Each SVE thus contributes a number of samples equal to the number of elements used in the mesh and the total distribution represents that volumetric probability of the distribution of FIP values. These distributions span several orders of magnitude, thus are best viewed on a log scale. To accommodate this plotting, all FIP distributions are plotted with all 0 value FIPs removed. The relative percentage of 0 value FIPs remains relatively constant for individual SVE of a configuration and for all configurations at the same loading condition. For the randomly textured sensitivity data, it is evident that the

distributions are all of similar form. At the higher strain levels, a more homogenous distribution of plasticity is observed (the CDF is more vertical, indicating a higher probability density in this region). These observations are consistent for the life limiting tails of the distribution as well.

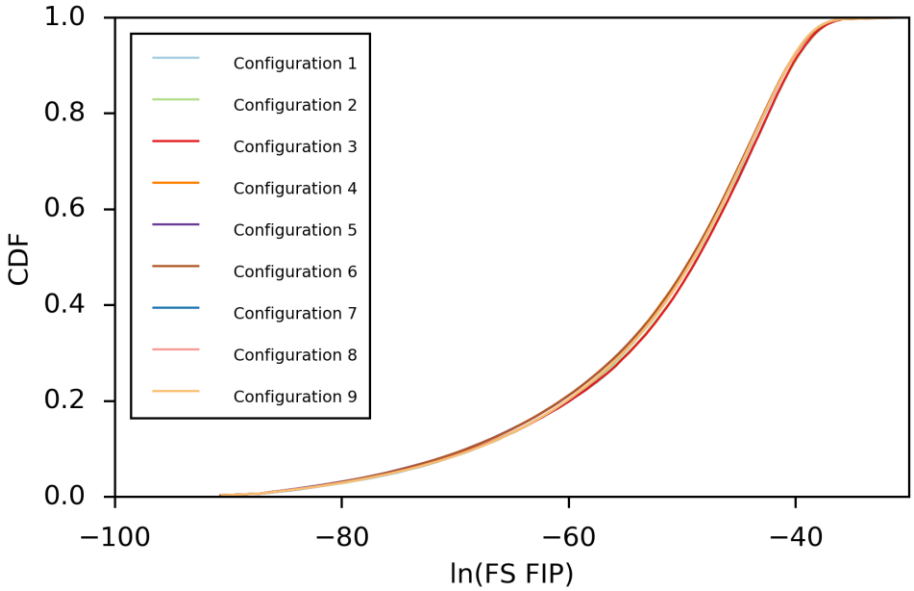

Figure 32. FIP distributions for 9 configurations of the same nominal microstructures of randomly textured Ti64 at $\boldsymbol{\varepsilon_a = 0.35\varepsilon_y}$.

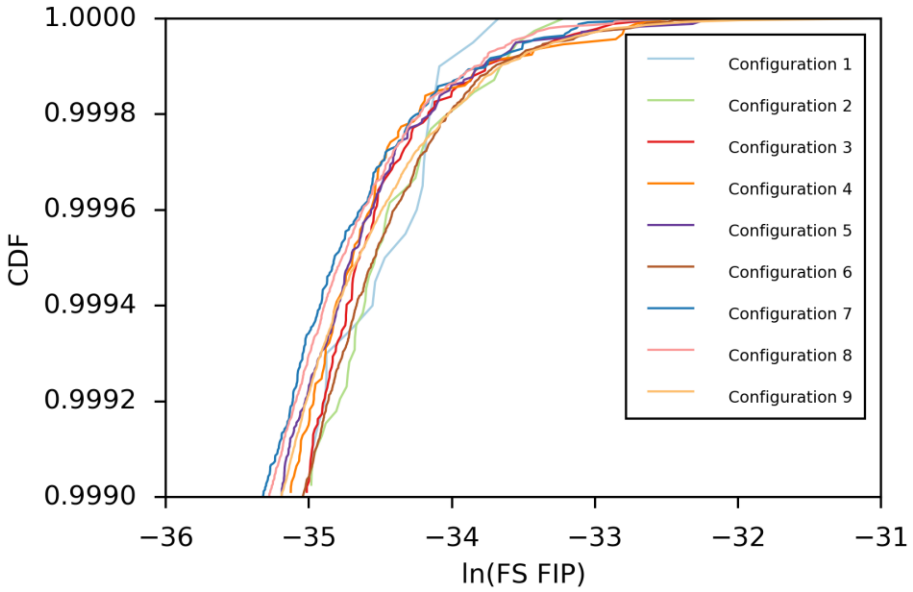

Figure 33. 99.9% tail of the FIP distributions for 9 configurations of the same nominal microstructures of randomly textured Ti64 at $\boldsymbol{\varepsilon_a = 0.35\varepsilon_y}$.

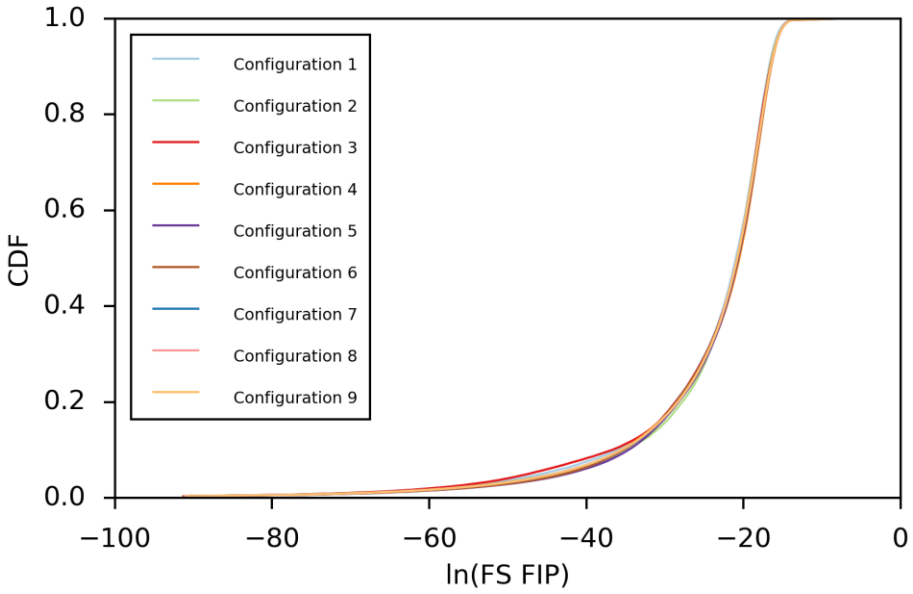

Figure 34. FIP distributions for 9 configurations of the same nominal microstructures of randomly textured Ti64 at $\boldsymbol{\varepsilon_a = 0.7\varepsilon_y}$.

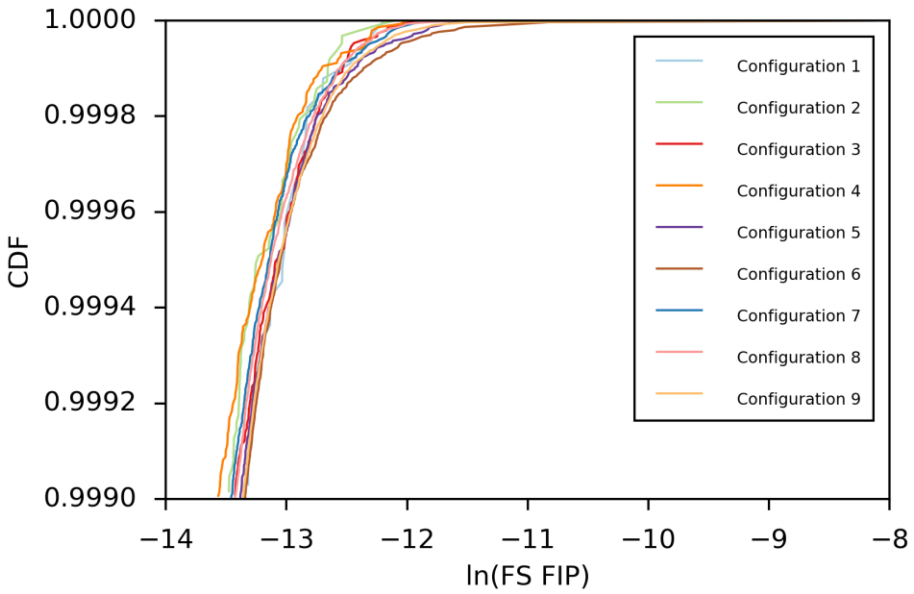

Figure 35. 99.9% tail of the FIP distributions for 9 configurations of the same nominal microstructures of randomly textured Ti64 at $\boldsymbol{\varepsilon_a = 0.7\varepsilon_y}$.

While these FIP distributions are relatively comparable, the KS-test rejects the notion that these samples are randomly selected from the same distribution by any rational threshold ($p < 10^{-4}$). The tail ordering is not significantly correlated with the number of elements, grains, nor mesh refinement in each SVE, however.

While Figure 32 - Figure 35 were for the same target microstructure and texture, Figure 36 provides a reference for FIP variations of various textures for the same material. It is observed that the scatter in FIP distributions is significantly larger when the texture is varied and the simulation parameters are held constant than when the simulation parameters are varied for a randomly textured microstructure. This is a desirable trait, as uncertainty associated with the decision variable (FIP distribution) should be minimal in comparison to the variation due to different inputs (textures) to confidently inform design decisions.

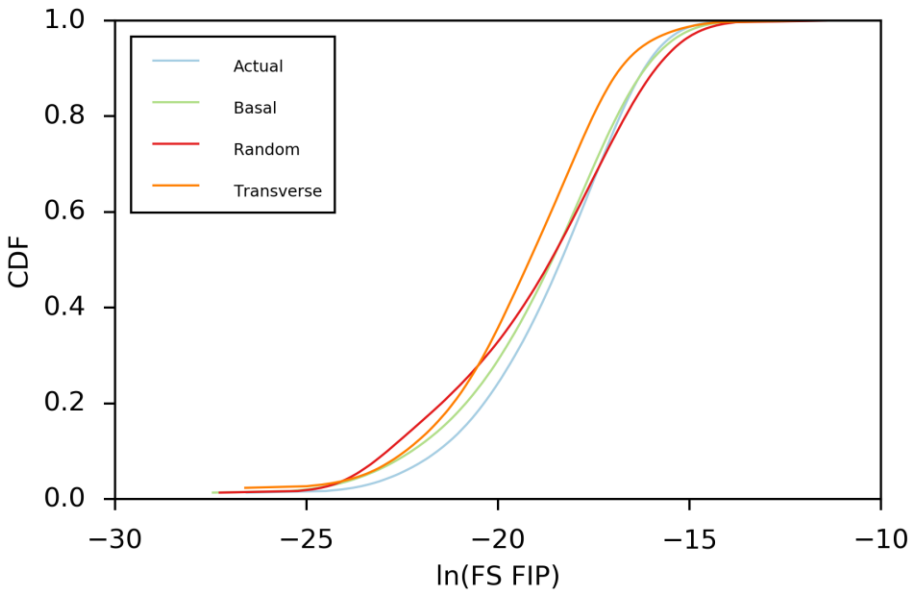

Figure 36. FIP distributions for four textures of Ti64 with y-axis tension/compression at $\boldsymbol{\varepsilon_a = 0.75\varepsilon_y}$.

If stress gradient and mesh refinement lead to a shift in FIP distribution, reduced fidelity models should not remain in a stable region around the refined simulation. Configuration 1 Table 2 and a new configuration of 500 μm sidelength composed of 1000 elements ($\delta = 8.\overline{3}$ and $E_g = 1.2$) were repeated for 100 instantiations to explore potential divergence in the distributions. These configurations will be referred to as Small Configuration 1 and Small Configuration 2, respectively. The convergence of each FIP distribution to the "true" distribution, constructed from the total FIPs for 40 instantiations of Configuration 9, is presented in Figure 37.

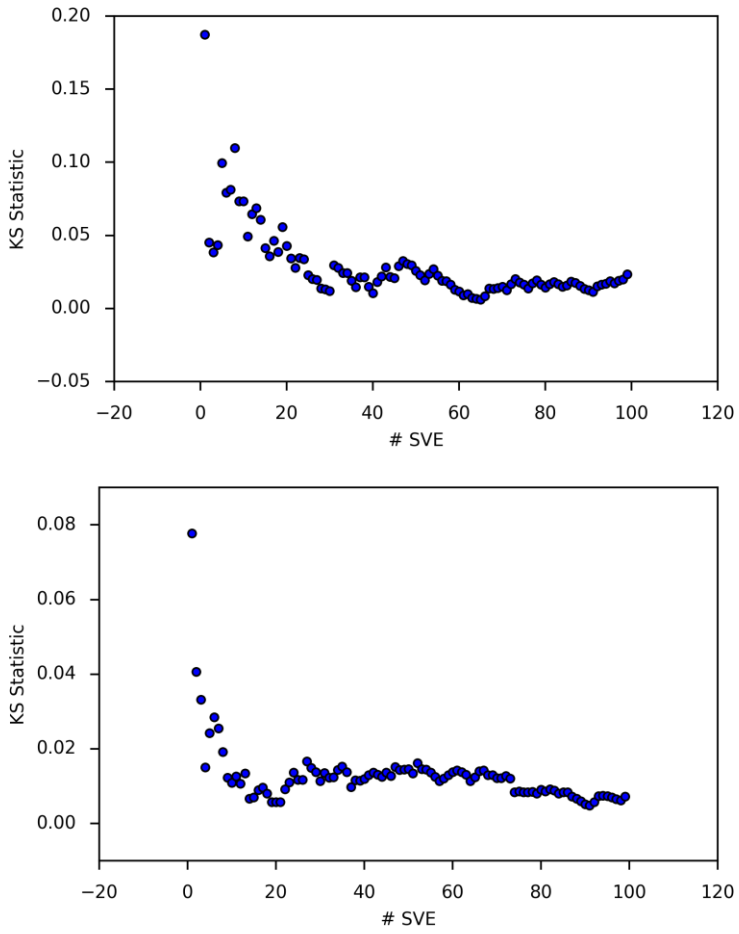

Figure 37. Convergence of FIP distributions for 12^3 15 µm (top) and 10^3 50 µm element (bottom) meshes of randomly oriented Ti64 grains as compared to 40 SVE of 49^3 8.5 µm elements.

Instead of producing a divergence, both reduced fidelity models remain in a neighborhood of the "true" distribution. Indeed, the convergence of the poorest morphological reconstruction is more rapid and remains closer to the "true" distribution. Even with the average 2 elements per grain, the overall distribution is captured quite accurately. While this is a toy problem and not demonstrative of intragranular stress gradients and grain boundary slip transfer, these results may indicate (for this particular material and model) that the convergence is determined primarily by sampling from the full orientation and misorientation space. That is to say, by sampling across more grains

and not requiring higher fidelity meshes it appears that the convergence rate to the true volumetric distribution of FIPs may be increased. It is also important to note that these initial conclusions were drawn from the simplest of grain morphologies (equiaxed) and crystallographic texture (random).

4.2: Tail Behavior of FIP Distributions

Since extrapolation of observations is critical to predict the scatter in fatigue lives, quantification of the tail behavior of the FIP distributions is desirable. Moriarty et al. [117] conducted extensive work in extrapolating wind loadings and the associated fatigue spectrum from limited simulations of observed wind loading data on turbines. Maximum loadings over a 99% threshold were fit to various distributions and the estimated return periods compared. A similar method may be used to characterize and extrapolate the finite FIP observations from crystal plasticity simulations. Quantification and characterization of the tail behavior by a standardized probability distribution reduces the amount of information required to build a useful database of fatigue resistances of simulated materials while also providing a reliable means of extrapolating values.

The work of Przybyla and McDowell [39] clearly established the FS FIP response from periodic crystal plasticity simulations as belonging to the Gumbel domain of attraction. Since an exponential tail typifies these underlying distributions, it is most desirable to fit the tails with an exponential function. Indeed, a Gamma distribution (a generalization of the exponential distribution with a shape parameter) is found to provide a satisfactory fit for the tails of the FIP distributions of all simulations conducted. As in previous distributions, the μ_g parameter locates the distribution, σ_g scales the distribution, and α describes the shape of the distribution and $\Gamma(x)$ is the Gamma distribution. The probability distribution of this three-parameter form is found in Equation (35).

$$f\left(x\right)=\frac{1}{\Gamma\left(\alpha\right)}\left(\frac{x-\mu_g}{\sigma_g}\right)^{\alpha-1}e^{-\left(\frac{x-\mu_g}{\sigma_g}\right)} \tag{35}$$

The following figures are provided to emphasize the closeness of both the distributions constructed from the same SVE parameters as well as the degree to which the Gamma distribution consistently describes the tail behavior. Specific information about the goodness of fit and distribution parameters may be found in APPENDIX C.

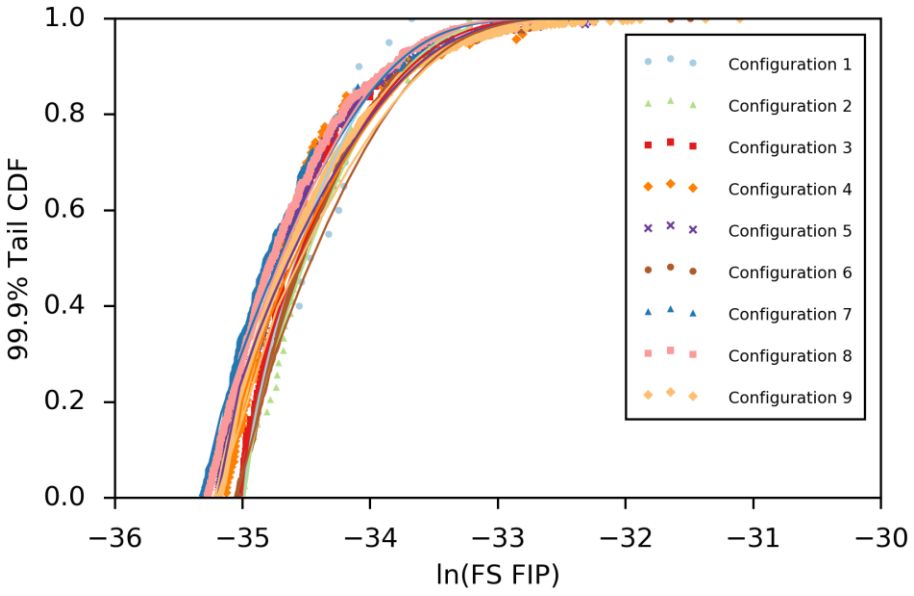

Figure 38. Gamma distribution fits for 9 configurations of the same nominal microstructures of randomly textured Ti64 at $\boldsymbol{\varepsilon_a = 0.35\varepsilon_y}$.

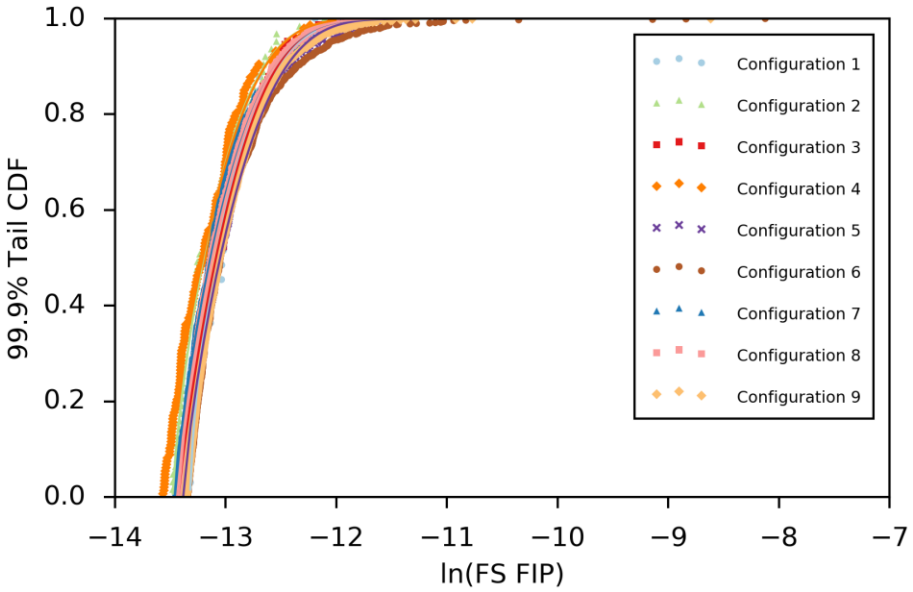

Figure 39. Gamma distribution fits for 9 configurations of the same nominal microstructures of randomly textured Ti64 at $\varepsilon_a = 0.7\varepsilon_y$.

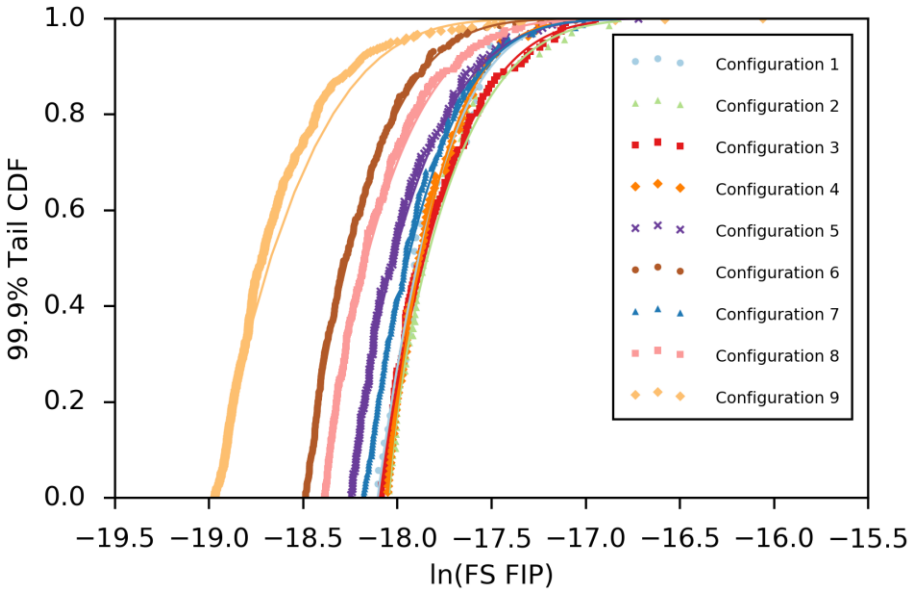

Figure 40. Gamma distribution fits for 9 configurations of the same nominal microstructures of randomly textured IN100 at $\varepsilon_a = 0.35\varepsilon_y$.

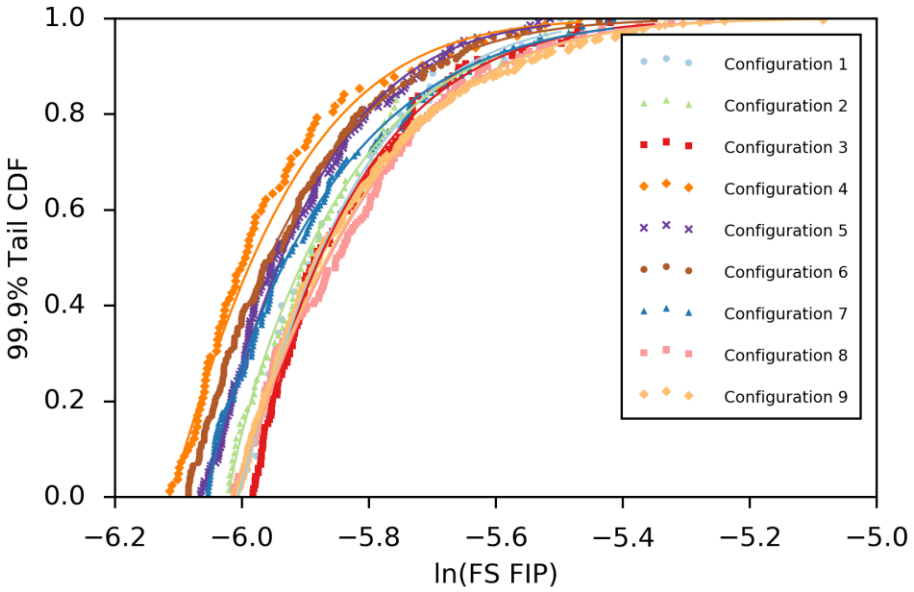

Figure 41. Gamma distribution fits for 9 configurations of the same nominal microstructures of randomly textured IN100 at $\boldsymbol{\varepsilon_a = 0.7\varepsilon_y}$.

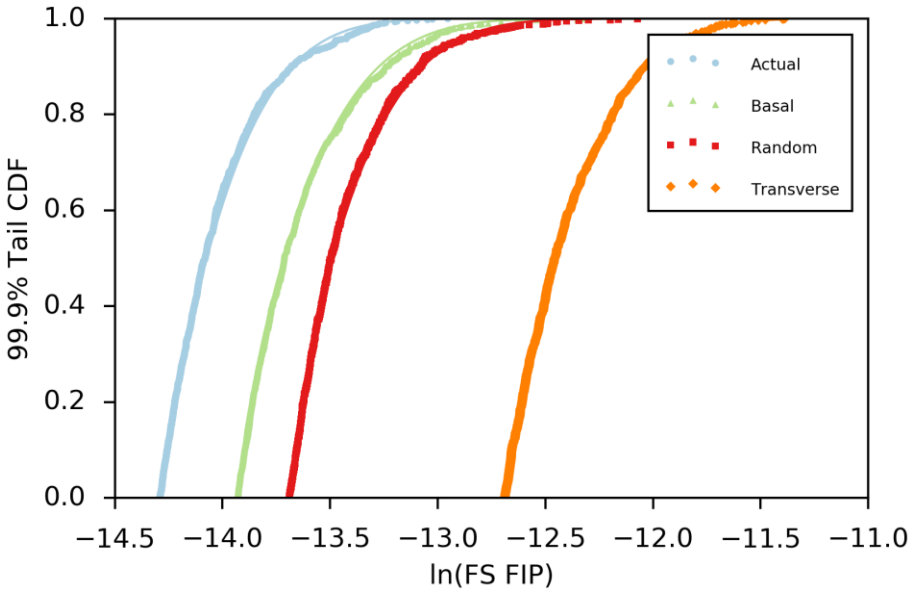

Figure 42. Gamma distribution fits for FIP tails of four textures of Ti64 under $\boldsymbol{\varepsilon_a = 0.7\varepsilon_y}$ x-axis strain.

For the randomly textured simulations, neither the tail length nor any of the simulation parameters have significant correlation to the distribution parameters. If the

sampled FIP distributions are indeed not randomly sampled from the same distribution, some neglected factor must be causing the variance in tail and overall distribution behavior. Since the tail behavior is well behaved and described by the chosen distribution form, a sufficient description of the fatigue resistance appropriate for extrapolation can be contained in a concise, and easily presented manner.

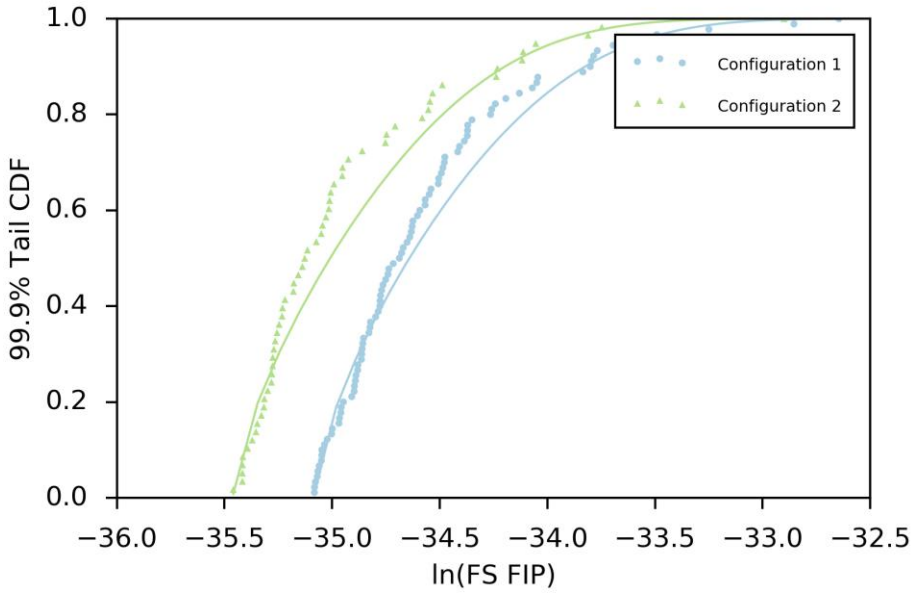

Figure 43. Gamma distribution fits for 100 SVE of Small Configuration 1 and Small Configuration 2 randomly textured Ti64 at $\boldsymbol{\varepsilon_a = 0.35\varepsilon_y}$.

As was previously observed at the overall FIP convergence level, the reduced fidelity SVE behaves similarly at the tail. Both configurations are accurately fit by parameters within the range previously fit for FIP distributions of more realistic morphological reconstructions. The similar results across vastly different simulation parameters indicate a relative insensitivity to the selected mesh. This fact is useful when selecting mesh configurations to use in parametric studies or optimization problems requiring large numbers of material simulations. The absolute characterization of fatigue resistance by the FIP distribution may be performed (with relatively minor uncertainties) with significantly less computational expense.

While the total number of SVEs is relatively high for the sampled small configurations, it is pertinent to note that the total number of FIP samples for Small Configuration 2 is still less than the total number of samples from the 20 largest SVE in Configuration 9. Indeed, the total 10^5 elements in is still less than the $1.25x10^5$ elements from a single SVE at Configuration 9. The variance of the tails is depicted in Figure 44 when compared with the combined distribution of Small Configuration 2. It is important to note that even though Configuration 9 samples an average of 650 grains in each SVE, the scatter observed between the SVE tails is relatively high. This is likely attributable to the fact that each tail is composed fewer grain responses compared to the total number of samples. For Configuration 9, 1452 elements are represented in the 20 tails with only 401 grains being sampled. These samples thus contain the covariance imposed by the similar intensification features (e.g. neighbor orientation, Schmid factors, etc.) and the compatibility of deformation from the FEM. This rough analysis also neglects other potential covariant features including neighboring grains that are also contained in the tail.

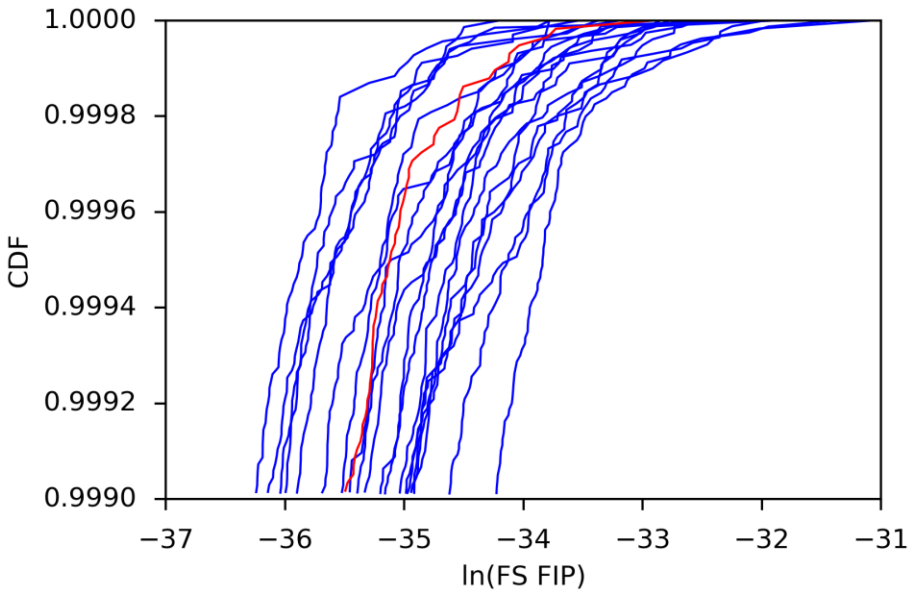

Figure 44. Comparison of empirical CDF of 20 SVE at Configuration 9 (blue) and the combined empirical CDF of 100 Small Configuration 2 (red) randomly textured Ti64 at $\boldsymbol{\varepsilon_a = 0.35\varepsilon_y}$.

In addition to the observations of the individual element FIPs, it is desirable to characterize the behavior of the tails of the various averaging methods. Compared to the previous simulations for which all configurations had relatively constant curvature, the averaged FIP distribution tails demonstrate significant differences in both location and shape. This is because the relative independence of FIP samples is reduced by the averaging method. For smaller simulation volumes, the 99.9% tail of 20 SVE may contain only 2-3 full averaging volumes, whereas for the larger SVE, this is mitigated with the tail containing samples from significantly more (10-15) full grain equivalent volumes. If fitted distributions are used to sample via Monte-Carlo methods the extreme value behavior for comparison, significant differences will arise due to the drastically difference tail shape. In addition to the change in tail shape, the relative scatter of the location μ_g is not reduced when compared to the element FIP values, thus limiting the

improved power of averaged FIPs when volumetric distributions are compared between simulation configurations.

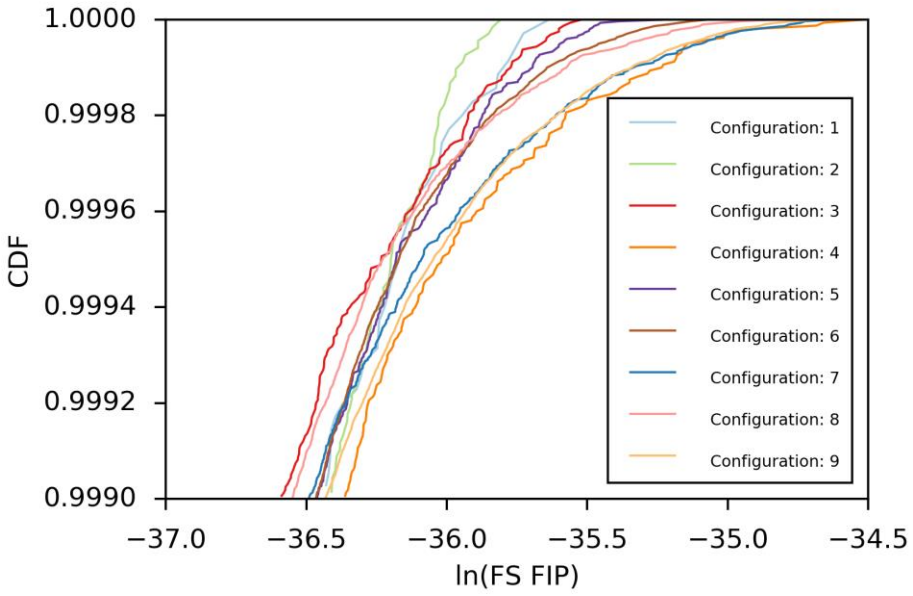

Figure 45. 99.9% tail of the Gaussian averaged FIP distributions for 9 configurations of the same nominal microstructures of randomly textured Ti64 at $\boldsymbol{\varepsilon_a = 0.35\varepsilon_y}$.

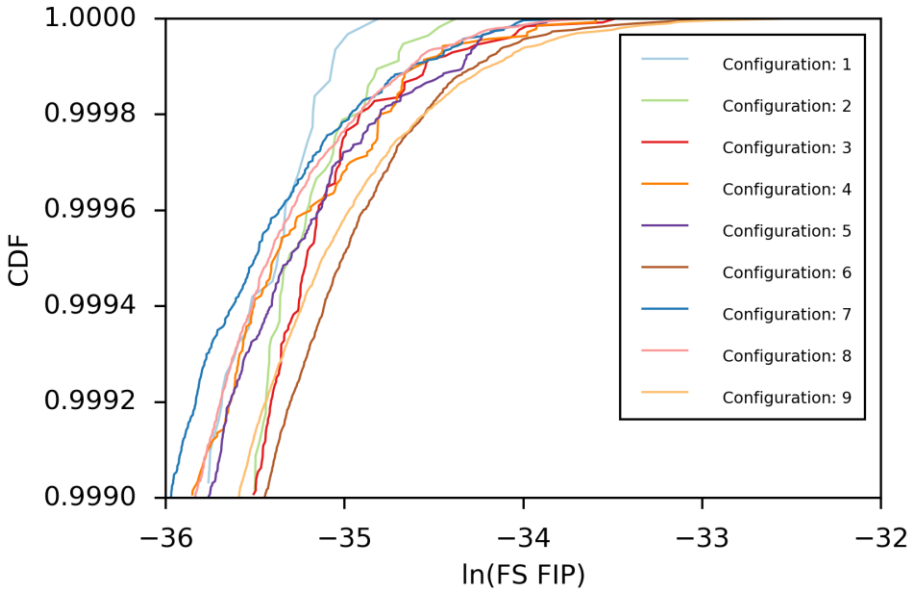

Figure 46. 99.9% tail of the cube averaged FIP distributions for 9 configurations of the same nominal microstructures of randomly textured Ti64 at $\boldsymbol{\varepsilon_a = 0.35\varepsilon_y}$.

Taking into account the previous observations for the Ti64 and IN100 models, a third material, Al 7075-T6, was also used to observe FIP tail behavior. This model and morphology is described in depth in Chapters 5 and 6. The textured material was loaded in RD-ND shear and RD tension/compression to see if a consistent shift in FIP distribution is observed under varied loadings. Twenty SVE were simulated for each configuration.

Table 5. List of configurations for the Al 7075-T6 FIP comparison.

Configuration #	δ	E_g
1	4	5
2	8	2.5
3	16	1.25

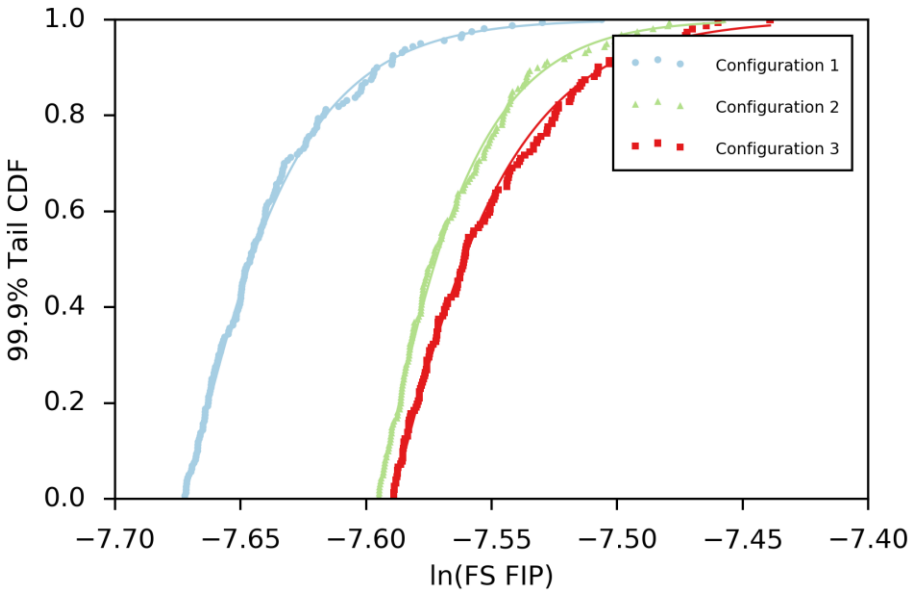

Figure 47. 99.9% tail of the element FIP distributions for 3 configurations of Al 7075-T6 at $\boldsymbol{\varepsilon_a = 0.7\varepsilon_y}$ in the RD.

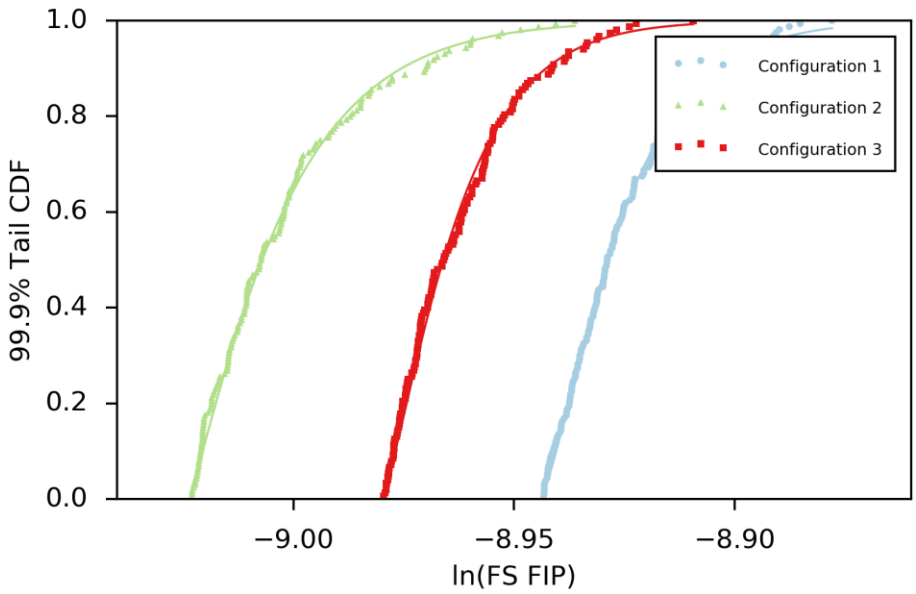

Figure 48. 99.9% tail of the element FIP distributions for 3 configurations of Al 7075-T6 at $\gamma_a = 0.7\varepsilon_y$ in the RD-ND plane.

Several important observations can be made from this data. The Gamma distribution still appears to provide an accurate representation of the FIP tail behavior. In addition, the relative ordering of the configurations is not consistent, though the total scatter in the distributions is relatively minimal. Even with these relatively minute differences in distribution (~5%), it is important to note that the uncertainty inherent in the tail fitting process is significantly less than the uncertainty due to the limited number of influencing features (e.g. orientation, disorientation, etc.) sampled in the SVE. Furthermore, the uncertainty associated with the experimental CDF as a predictor of the true CDF is complicated by the covariance involved in the sampling from the underlying FIP distribution caused by the process of synthetic microstructure reconstruction and CPFEM simulation for each SVE. This is observed in the fact that the individual SVE distributions, displayed in Figure 44, are noticeably different in shape from the total empirical CDF. This difference is also rejected by statistical tests such as the KS test. The uncertainties associated with the empirical CDF and the covariance in the sampling of

individual SVEs should be addressed in further works quantifying the distribution of FIPs in various materials.

4.3: Proposed Mesh Insensitive Fatigue Comparison

As previously discussed, several different fields utilize extreme value distributions in various ways to extrapolate various behaviors. It is useful to discuss the behavior of FIP observations as compared to these more traditional fields. For particle counting methods, there is an inherent link between the observation window and the resolution with which a particle may be described based on limitations of laboratory equipment. For FIP responses, the finite resolution obtainable by a microscope appears to be analogous to the total number of elements in the FEM mesh. Likewise, the observed area may be equated to the simulated volume.

There is no inherent advantage in particle counting to treat the combination of multiple small observation windows as a single, larger window so long as each observation window is already of sufficient size to observe the largest particle (of the considered type). The stitching together of multiple observation windows may be equated to simulating a larger SVE with consistent element size. Increasing the simulated volume, however, can more accurately capture long range spatial ordering and misorientation distributions while reducing potential boundary value effects. Both aspects can contribute to shifts in the FIP distribution [46].

To take advantage of this fact, the well-defined tail behavior, and desirability of conducting a reduced number of SVE simulations, a new method of comparing fatigue driving forces is proposed. The proposed method retains the ability to characterize fatigue response through extreme value distributions and return periods, reduces uncertainties associated with limited quantity of SVE simulations, and provides the ability to compare more easily, fatigue responses arising from varied simulation sources.

The proposed method can be performed as follows:

- Construct the empirical CDF of FIPs from multiple SVE simulations.
- Characterize the tail distribution.
- Use Monte Carlo sampling to construct an extreme value distribution from the averaged distribution and fitted tail.

By constructing and explicitly addressing the underlying FIP distribution, the method reinforces the source of fatigue comparisons. In addition, convergence of this distribution from multiple SVEs is more closely coupled with the definition of the SVE as discussed previously. Characterization and presentation of the tail distributions creates a low cost method of presenting and reproducing fatigue information for a variety of uses. Coupled with a simple plot of the overall FIP distribution, comparisons to literature become significantly easier and entire datasets may be recovered for additional analysis. Finally, this proposed method decouples the sample size for the extreme value distribution and the SVE size. Previously these two values were constrained to be the same value by virtue of selecting the maximum values on a per SVE basis. Decoupling the sizes relaxes the need to adjust Gumbel distribution parameters to make comparisons between fatigue driving forces in different materials. For instance, if a data set is provided in 1,000,000 element simulations, there is significant computational cost to construct a similar data set with a new material for comparison. Instead, it should be apparent from the previous sections that this level of mesh refinement (or volume size) is not necessary to describe the fatigue behavior of the material and we may instead estimate the fatigue resistance for comparison with significantly cheaper simulations. In addition to reducing computational costs by means of cheaper individual simulations, computational costs may also be reduced by minimizing wasted simulations. SVE of different configurations may still provide useful estimates of the FIP empirical CDF and thus be used to improve the empirical CDF estimate.

By sampling from the total distribution instead of the individual SVE, the new method does not reflect the spatial covariance of FIPs present due to the grain

orientations. These spatial correlations have been well studied in works by Przybyla and McDowell and indeed, the data required to reconstruct them is still included in any SVE of reasonable fidelity used with the proposed method. Additionally, the incorporation of uncertainty is no longer directly attributable at the extreme value distribution with appropriate confidence intervals yielded from the maximum likelihood estimation of the Gumbel parameters. Uncertainty must instead be addressed at the FIP distribution level, with confidence intervals placed on the distribution and the parameters of the fitted tail distribution. Once confidence intervals have been established on the underlying distribution, Monte-Carlo sampling may be used to estimate the true extreme value distribution with associated confidence intervals.

4.4: Comparison of Fatigue Performance for Textured Ti64

To illustrate the application of the proposed fatigue simulation approach, a series of simulations of variously textured Ti64 were considered. For a baseline, the traditional method of constructing and extreme value distribution from the SVE maximum FIP values is presented in Figure 49.

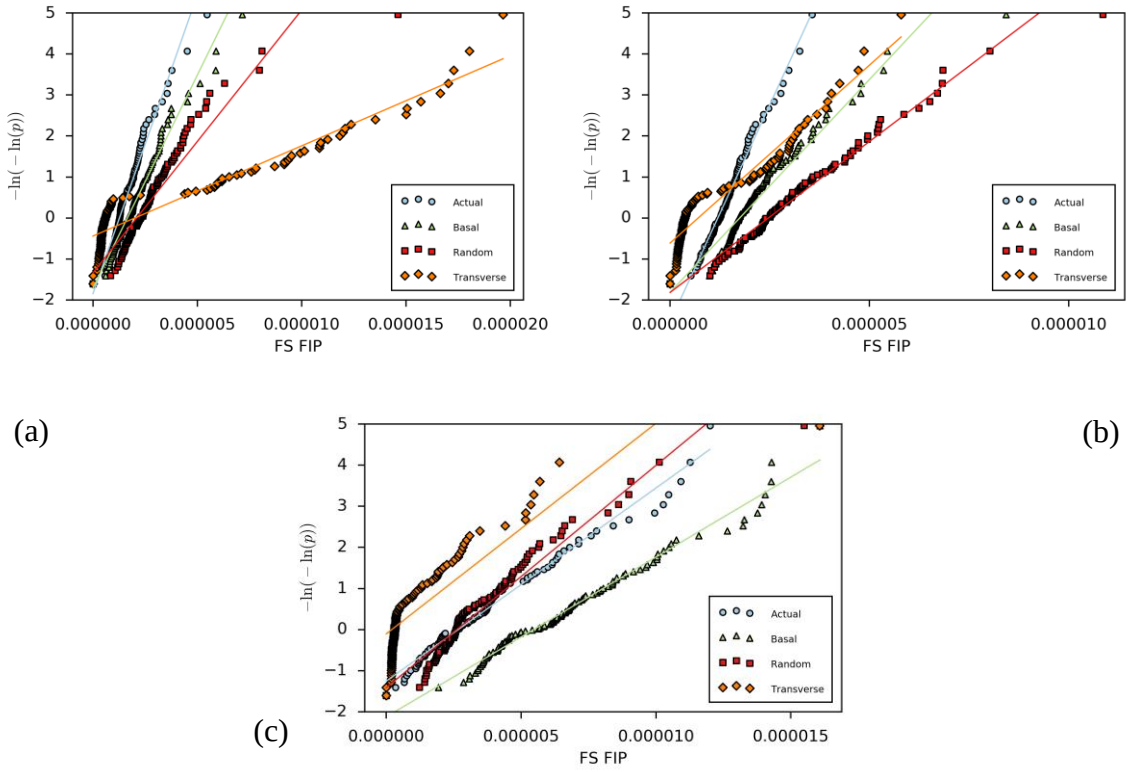

Figure 49. Comparison of extreme value distributions from 100 SVE in each of x (a) y (b) and z-axis (c) loading conditions of basal, transverse, random and actual textures using the SVE maximum FIP.

In this comparison of the fatigue resistance of the various Ti64 textures, it is apparent that the Gumbel distribution for the extreme FIPs is not a good representation of the extreme behavior of the transverse texture. This type of kinked curve is typically observed in materials where multiple mechanisms are competing to drive the fatigue behavior. Methods of treating this behavior as a single distribution include the competing risks and mixture models [104]. Indeed, there appear to be two distinct classes of FIP distributions from the SVE simulated as evidenced in Figure 50. It is unknown if a local minimum in the reconstruction process or some other phenomenon led to the significant covariance present in the samples. The three remaining textures appear to exhibit random behavior with central tendencies along the entire CDF. The relative spread of the tails for

all other textures are less than ½ the range (on the log plot) of the transverse textured ln(FIP) tails.

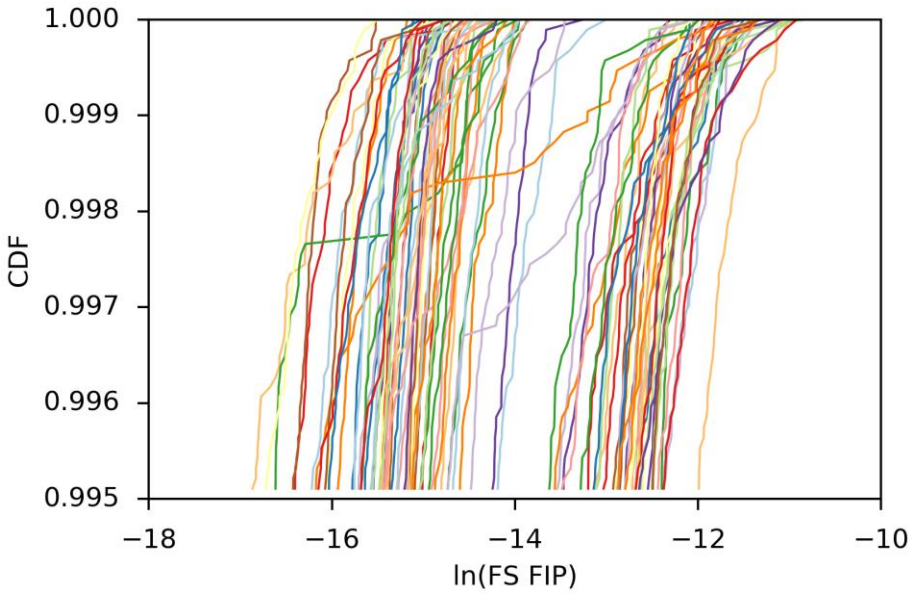

Figure 50. FIP distributions for 100 SVE of transverse texture Ti64 in x-axis tension/compression.

Fundamentally, however, it is undesirable to consider FIP distributions in this manner. Specifically, the volumetric occurrence of FIP values should be related to the fatigue lives. Weighting the occurrence of low and high FIP microstructures equally does not facilitate an accurate distribution of damage for the purposes of fatigue design. The probability of failure should instead be linked directly to the total volumetric FIP distribution as constructed from the ensemble of instantiation values.

This can be demonstrated using the proposed method with a sampling size less than the SVE size of 9261 elements. A sample size of 1000 elements is selected a baseline given the performance of the reduced fidelity meshes considered in the previous sections.

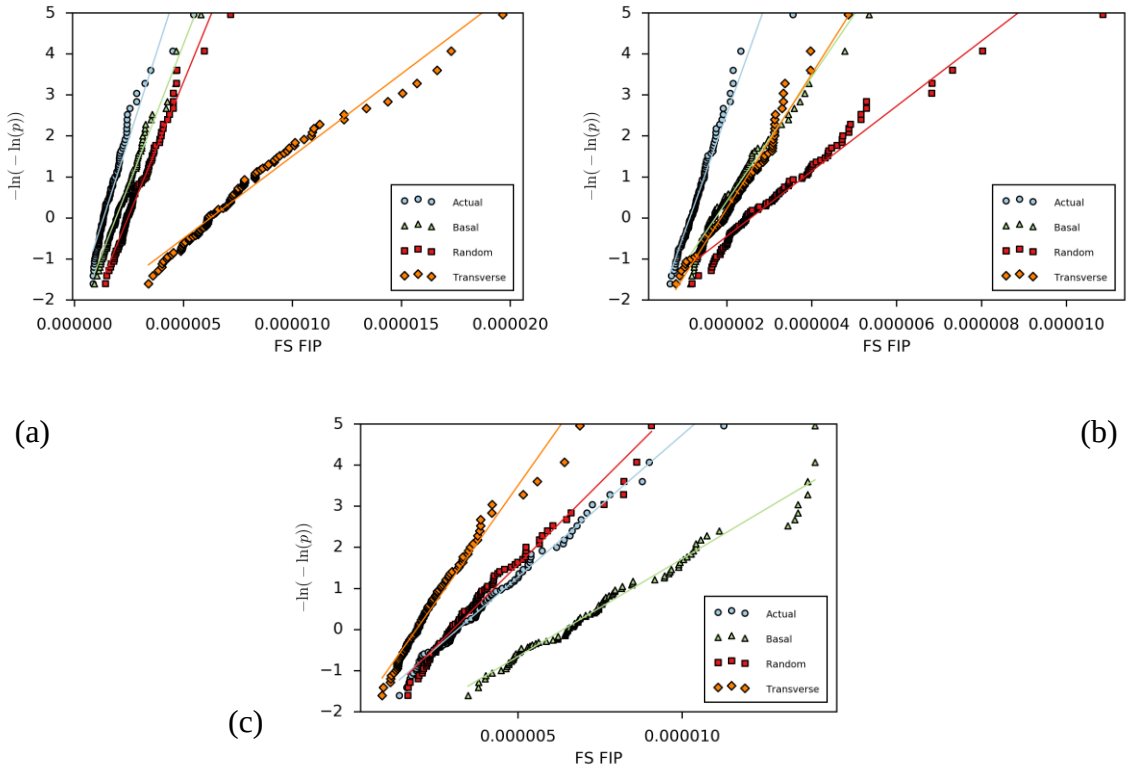

Figure 51. Comparison of extreme value distributions from 100 SVE in each of x (a) y (b) and z-axis (c) loading conditions of basal, transverse, random and actual textures using Monte-Carlo sampled values from the empirical CDF.

It is apparent that the relative ranking of the microstructures remains the same after the transformations by the proposed method. The linearized plot for the transverse texture extreme values is now indeed linear. This is because the new samples are randomly selected from the underlying distribution and the tail of the transverse texture distribution remains in the domain of attraction for the Gumbel distribution. On the other hand, if the detection of a competing risks failure behavior is desirable, the presented method will likely not provide the appropriate response, and instead a method based on individual SVE extremes should be considered.

In addition to the study of varied microstructures, it is desirable for the new method to obtain invariant results across a wide range of mesh parameters. To ascertain the effectiveness of the proposed method, this same method was repeated for

configurations and load conditions in the sensitivity analysis. Again, a sample size of 1000 was used for each SVE equivalent sample with the Gumbel distribution constructed from 50 SVE equivalent samples. These constructed distributions show remarkably lower sensitivity to the SVE parameters. This is because the underlying covariance has been removed and the values are now IID from the same underlying distribution. For Monte-Carlo samplings of the same underlying distribution, estimates of the true Gumbel distribution would be obtained in the limit. For the observed distributions, the relative distribution differences (as previously noted) will now determine the differences in observed behavior.

Upon application of the proposed method, the following results were obtained. The HCF Ti64 configurations had a maximum relative error of 89% for $\sigma_{element}$ and 27% for $\mu_{element}$ compared to the >300% for the estimates from SVE maximum values when excluding the outlier of >10000%. VHCF of Ti64 had relative errors of 48% and 27% for $\sigma_{element}$ and $\mu_{element}$ respectively. IN100 demonstrated significant correlation in the FIP distributions to the SVE parameters, and the results of this are higher relative errors of 96% and 138% for $\sigma_{element}$ and $\mu_{element}$ respectively. The correlation of the distribution tails creates a deterministic correlation in the respective extreme value distributions, with the highest element configuration (Configuration 9) have less than ½ the location as the lowest element configuration (Configuration 1). For HCF IN100 simulations, however the correlation is no longer apparent and the relative errors are significantly reduced to 26% and 13% respectively. While the errors presented are the maximum values for each simulation model and load, they indicate significantly improved agreement between the model parameters. It is estimated that with additional SVE these values may continue to converge. This can be captured by measuring the convergence of the distribution based on certain distance metrics, however, estimating the uncertainty for a fixed number of SVE is a significantly more challenging proposition. This is especially true because, as has been previously established, the

individual SVE sample distributions are not IID from the overall distribution and the ensemble distributions have greater differences than can be attributed to sampling error. This invalidates many traditional methods of dealing with uncertainty in distributions e.g. the Kaplan-Meier estimator for survival functions. Further work will be necessary to characterize the uncertainties associated with the proposed method.

4.5: Conclusions

In this chapter, the fundamental behavior of FIP distributions was investigated. It was observed that the distributions tend to be very well behaved, following similar trends across different instantiations. In addition, distributions were observed to be more similar for ensembles of SVE with the same nominal microstructure, indicating that larger numbers of SVE will be required to produce a converged distribution. The sampled distributions do appear to be reasonable approximations of the true, underlying distribution, however. In addition to the mean behavior, the life limiting tails were investigated. It is observed that for all load conditions studied across three material models and multiple textures, the tail of the empirical CDF appears to be well described by the Gamma distribution. Parameter values are found to have little correlation to the simulation values used to construct them, with the exception of the VHCF simulation of IN100. This particular load and material model has a left shift in FIP values with an increasing number of elements in the tail, thus producing non-conservative fatigue life estimates.

In addition to the observations of the underlying distributions, a new method was proposed with which to analyze and rank microstructure fatigue response. The Monte-Carlo based method was demonstrated to perform well on two data sets. For the comparison of multiple textures of Ti64, this method was found to rank microstructures in a similar fashion the previously utilized method with no loss of generality. In addition, the new method provides a reasonably reliable method of obtaining similar Gumbel

parameter estimates from simulations utilizing a wide range of SVE parameters. These results are more in line with a fundamental fatigue process and hold for HCF and VHCF simulations of Ti64, as well as HCF simulations of IN100. The exception cases appear to be related to the aforementioned shift in values with increasing number of elements, the cause of which is yet unknown. While additional research is necessary, this work provides a fundamental investigation into the role of the SVE and its construction parameters in terms of fatigue simulations using crystal plasticity models.

CHAPTER 5: POINT PROPAGATION FATIGUE MODEL

5.1: Introduction

Aluminum alloy 7075-T6 is an Al-Zn-Mg-Cu alloy designed for aerospace applications. The T6 designates a peak aged alloy developed for optimal precipitate hardening, and is often used in rolled plate applications. Of particular concern to the modelling efforts of this paper are the constituent particles that develop from impurities introduced during alloying and processing. These constituent sizes are typically on the order of 1-50 μm [118]. The constituents are still smaller than the average grain sizes observed for this material and consist of a relatively small volume fraction. Since SVE size is selected to allow relatively coarse grain definitions to capture multiple grain in a computationally efficient manner, the further refinement necessary to explicitly model constituents is not desirable. Instead, a homogenized material model was developed and calibrated by Hennessey [48] as part of previously contracted work with NAVAIR. The constitutive model form was carefully selected considering empirical cyclic ratcheting/mean stress relaxation, local plasticity, and cyclic stress/strain curves. Additional details concerning the process of selecting and fitting an appropriate model may be found in the work of Hennessey [48].

The selected model adheres to a standard power law flow rule

$$\dot{\gamma}^{(\alpha)} = \dot{\gamma}_0 \left| \frac{\tau^{(\alpha)} - \chi^{(\alpha)}}{g^{(\alpha)}} \right|^m sgn(\tau^{(\alpha)} - \chi^{(\alpha)}) \tag{36}$$

where α is the current slip system, $\dot{\gamma}^{(\alpha)}$ is the shear strain rate on this slip system, $\dot{\gamma}_0^{(\alpha)}$ is the reference shear strain rate, $\tau^{(\alpha)}$ is the shear stress, $\chi^{(\alpha)}$ is the back stress, and $g^{(\alpha)}$ is the drag stress. The current model implements the flow rule on the 12 octahedral slip

systems <110> (111). The Ohno-Wang (OW) [119] form of evolving back stress was selected to better capture mean stress effects and is formulated as follows

$$\dot{\chi}^{(\alpha)} = \sum_{i=1}^{2}\left(h_i\dot{\gamma}^{(\alpha)} - r_i\left(\frac{\left|\chi^{(\alpha)}\right|}{b_i}\right)^{m_i}\chi^{(\alpha)}\left|\dot{\gamma}^{(\alpha)}\right|\right) \tag{37}$$

where h_i and r_i capture the hardening and recovery and m_i is the OW exponent relating the different powers of the hardening and recovery terms. This model has a constant drag stress

$$\dot{g} = 0 \tag{38}$$

Fatigue calibration by Hennessey was performed using the mesoscale approach introduced by Castelluccio [40] with the development of improved methodology to incorporate Stage II crack growth along multiple slip systems. The final fatigue calibration and crack growth formulations are reproduced in Figure 52 and Equations (39) - (44) respectively.

$$N_{total} = N_{inc} + N_{nuc} + N_{MSC} + N_{PSC} + N_{LC} \tag{39}$$

The crack growth law includes several terms comprising the life of the part until failure N_{total}. The first step is the fracturing of the constituent particle necessary to create a dominant fatigue crack N_{inc}. This work considers two definitions of the nucleation life N_{nuc}. The first term was used by Castellucio and Hennessey and considers the number of cycles until the formation of a crack within a nucleant grain based on a simplified dislocation model by Tanaka and Mura [41]. This method assumes the crack length at nucleation is the entire slip band across the nucleant grain.

$$N_{nuc} = \frac{\alpha_g}{d_{gr}}\left(FIP^{\alpha}\right)^{-2} \tag{40}$$

The second definition of N_{nuc} used is the number of cycles required to extend the crack from the incubated particle into the surrounding grain. This definition is used by a

series of papers by Bozek and Hochhalter et al. [10, 44, 45]. Differing definitions are also used by Xue et al. [120] who consider N_{inc} to be the number of cycles during which the particle is cracked and the crack extends through the initial notch root influence, thus any reference to the early stages of crack growth will be explicit in definition used.

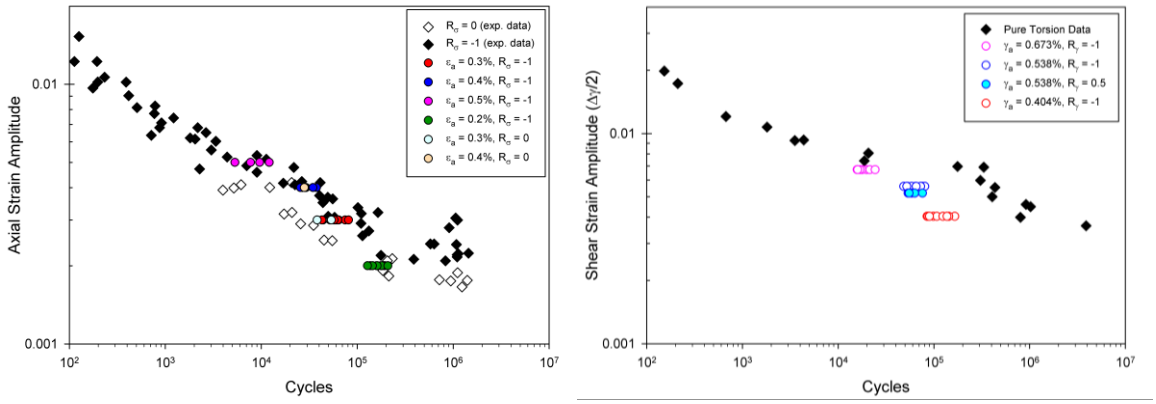

Figure 52. Final calibration of mesoscale crack propagation method as applied to uniaxial (left) and shear (right) loadings compared to experimental data from [80].

For each of the previous implementations of the mesoscale crack growth law, incremental crack advances were considered on a grain by grain level. Grains are divided into "bands" parallel to the slip planes and only those bands adjacent to the current crack are considered for advancing. Crack advancement thus occurs in discrete, grain-by-grain increments whose incremental length is expressed by

$$\Delta a = \sqrt{\frac{V_b}{t_b}} \tag{41}$$

where V_b is the volume of the cracked band and t_b is the thickness of the band. FIPs are computed on a per-slip-system basis with averaging over the band volume. The computation of each slip system FIP^{α} may be found using

$$FIP^{\alpha} = \frac{\Delta\gamma_p^{\alpha}}{2}\left(1 + k\left\langle\frac{\sigma_n^{\alpha}}{\sigma_y}\right\rangle\right) \tag{42}$$

where the slip $\Delta\gamma_p^\alpha$ and the resolved shear stress σ_n^α are now computed for the slip system instead of the total plastic strain tensor. The local MSC growth rate $\frac{da}{dN}$ on slip system α has been expressed as

$$\left.\frac{da}{dN}\right|_{msc}^{\alpha} = \phi\left\langle \beta_i A_{\mathrm{FS}} FIP^{\alpha}(a) - \Delta CTD_{th} \right\rangle \tag{43}$$

where ϕ is the irreversibility constant of 0.35 based on the argument by Xue et al. [120], β_i is an influence coefficient for low misorientation neighbors, A_{FS} is a calibration parameter for the FIP which is a function of the normalized distance a to the next grain boundary, and ΔCTD_{th} is the threshold crack tip displacement for crack propagation. This expression can be integrated analytically to form an expression for the number of cycles N to crack the considered band within a grain. The values c_1 and c_2 are functions of the above variables for brevity and D_{st} is the current band diameter computed by the same process as Equation (41)

$$N = \int_0^1 \frac{dN}{da_i} da_i = \frac{1}{\sqrt{c_1 c_2}} \tanh^{-1}\left(D_{st}\sqrt{\frac{c_2}{c_1}} \right) \tag{44}$$

In order to model cracks and stress redistribution within volume elements of Al 7075-T6, Hennessey applied an isotropic damage method introduced by Castelluccio to this material model within the Abaqus UMAT procedure. By interfacing with the UEXTERNALDB call via the COMMON_BLOCK variables, an array of cracking states is read in from a text file. For more information on this procedure see Hennessey [48]. For damaged elements, the stiffness tensor C is proportionally reduced using the damage value d according to

$$C_d = (1-d)C \tag{45}$$

This damage state variable is allowed to evolve as a function of time and the stress normal σ_n to the crack plane for this element. The value of the damage rate v was selected to maximize numeric stability and ensure damage fully evolves within a single

loading cycle. The damage at a time $t + \Delta t$ for a previous time t and time step Δt may be expressed by the following

$$d_{t+\Delta t} = \begin{cases} \min(0.99, d_t + v\Delta t) & \sigma_n > 0 \\ \max(0, d_t - v\Delta t) & \sigma_n > 0 \end{cases} \tag{46}$$

This method allows the cracked volume to recover stiffness in tension to better model potential crack closure and sliding effects. A maximum damage value $d = 0.99$ is imposed to facilitate FEM convergence and has by shown by Castelluccio [47] to be sufficient for stress redistribution and propagation methods.

5.2: Crack Formation: Incubation and Nucleation

For Al 7075-T6, the total process of crack formation may more accurately be described by the summation of two separate processes: crack incubation and crack nucleation. Crack incubation is the process by which the constituent particles are cracked, providing a site for crack extension into the matrix or nucleation. These two phases of crack growth are closely related and thus will be discussed together in the context of this work. Several investigations to the micromechanisms of fatigue for Al 7075-T6 indicate that the dominant fatigue cracks almost exclusively begin at cracked constituent particles ranging between 1-50 μm and being predominantly Fe-rich Al_7Cu_2Fe. Xue et al. [6] note that all samples incubated cracks at fractured constituent even in the presence of other significant stress concentrations such as an oxide film. These results are consistent with those of Harris and Bozek et al. [10, 11]. The particles tend to be significantly stiffer than the surrounding matrix with a Young's Modulus of approximately 160 GPa, elongated aspect ratios strongly oriented in the rolling direction as well as being broken into multi-particle stringers, and constitute approximately 2% of the alloy by volume [87, 121].

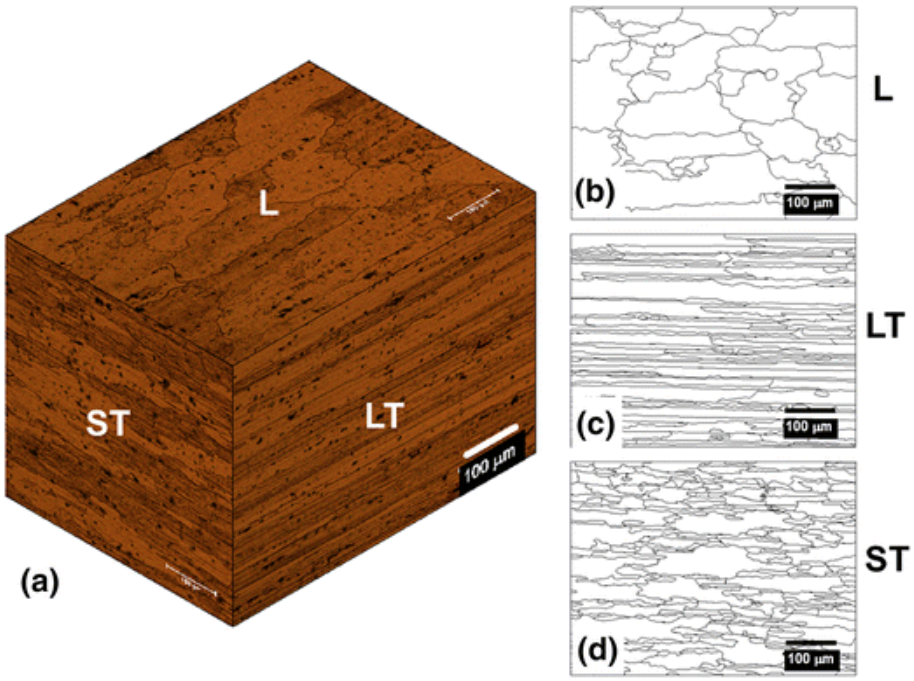

Figure 53. Particle distribution in "stringers" along rolling direction from [122].

In addition to contributing to particle shape and spatial distribution, the rolling process also cracks between 2-7% of particles prior to loading [10, 11]. Particles tend to fracture due to stress concentrations at inherent flaws leading to a crack plane perpendicular to the principal direction. This fracture probability has also shown strong correlation with the particle alignment to the loading direction [11, 123]. Much study has been performed for fracture probabilities and sensitivities as a function of particle and loading properties, however, these explorations have primarily focused on LCF. Since the stresses experienced in HCF are significantly less, and the direct application of previous studies was not possible, the assumption is made for an initial nucleation calibration that in HCF the cracks nucleate at particles cracked during rolling with a crack plane perpendicular to the rolling direction.

Since nucleation life can consume upwards of 80% of specimen life in the HCF regime, a calibration procedure was undertaken similar to that of Hochhalter et al. [44, 120]. To perform this calibration, an isotropic, linear-elastic phase with $E = 160$ GPa

and $\nu = 0.29$ was implemented in the UMAT based on estimated values by [6, 10]. The stiffness reduction method used to model a crack in the crystal plasticity code is also applied to this new particle phase.

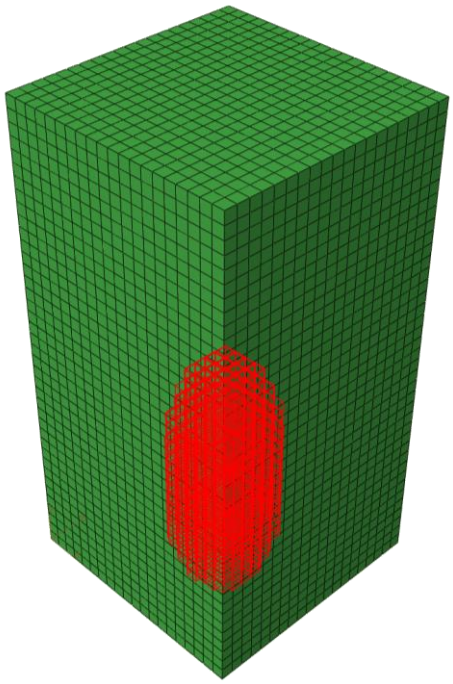

Figure 54. Nucleation calibration mesh with fractured particle.

Crack nucleation simulations isolate a single particle in a single crystal matrix. Five dominant orientations were selected to capture variations due to local grain orientation (shown by some simulations to have a secondary effect) [10, 124]. A relatively small computational volume and periodic boundaries mimic potential short range interaction effects between particles. Nucleation lives for the purposes of calibration are estimated from a series of experiments by Zhao and Jiang [80] under different load conditions. Shear nucleation lives were initially assumed to reflect the same proportion of the total lives from uniaxial tests estimated by Xue et al. [120]. Based on the aforementioned observations regarding particle fracture frequency, especially the limited information available at low amplitudes, it is assumed that this

incubation/nucleation estimate from Xue et al. will potentially also include some of the crack growth life as well.

$$N_{nuc} = 0.92 N_{total}\left(1 - e^{-0.0012 N_{total}}\right) \tag{47}$$

Following the results of a multi-part study conducted by Bozek et al. [10, 44, 45] several different damage parameters were investigated for potential correlation with nucleation lives and incorporation into a reduced fidelity FEM mesh. The following damage parameters are recorded at the crack mouth of the fractured particle for each simulation and the maximum values are used to correlate with fatigue lives.

$$\Gamma^{\alpha} = \int_0^t \left|\dot{\gamma}^{\alpha}\right| dt \tag{48}$$

$$D_1 = \max_{\alpha} \Gamma^{\alpha} \tag{49}$$

$$D_2 = \max_{p} \Gamma^{p} \tag{50}$$

$$D_3 = \Gamma = \sum_{\alpha=1}^{N_s} \Gamma^{\alpha} \tag{51}$$

$$D_4 = \max_{p} \int_0^t \sum_{\alpha=1}^{N_d} \left|\dot{\gamma}_p^{\alpha} \tau_p^{\alpha}\right| dt \tag{52}$$

$$D_5 = \max_{p} \int_0^t \sum_{\alpha=1}^{N_d} \left|\dot{\gamma}_p^{\alpha}\right| \left(1 + k \frac{\left\langle \sigma_n^p \right\rangle}{g_o}\right) dt \tag{53}$$

Nucleation simulations were conducted at 7 different loading conditions across a the range studied by Zhao and Jiang [80]. Four simulations were conducted in fully reversed tension/compression (0.8, 0.5, 0.4, .02%), and three in fully reversed shear (0.8, 0.6, 0.4%). In addition to studying the damage parameters directly, the ratcheting (cyclic accumulation) of each parameter was also studied. This was motivated by the findings of

Hochhalter et al. and the final nucleation calibration reproduced in Equation (54) (See section 1.2.1: for a description of the simulations and explanation of variables).

$$N_{Nuc} = \frac{\left(\frac{\sigma_{\theta\theta}^{max}}{\sigma_{\theta\theta}^{ult}}\right)^{\frac{1}{\alpha}} - D_1^{max}}{\Delta D_1^{max}} + 1 \tag{54}$$

In the findings of the current work, D_3, or the total accumulated slip, is the only parameter found to provide significant correlation to the nucleation estimates. A least squares regression was used to fit a power law relationship between the crack mouth averaged parameter and the average estimated nucleation lives. Initial calibration attempts, coupled with previously estimated MSC growth cycles indicated that using the formulation by Xue et al. to estimate nucleation lives provided a non-conservative total life estimate. Thus, assuming that the number of cycles required to detect the noticeable drop in stress behavior will include some of the crack propagation stage as well as the inherent scatter in fatigue lives, a knockdown factor of 0.5 was applied before arriving at the final calibration presented below. It is likely that the over estimation of the trendline compared to the LCF values are due to the prevalence of multisite crack formation not captured in the present model.

$$N_{nuc} = 0.015 D_3^{-1.8} \tag{55}$$

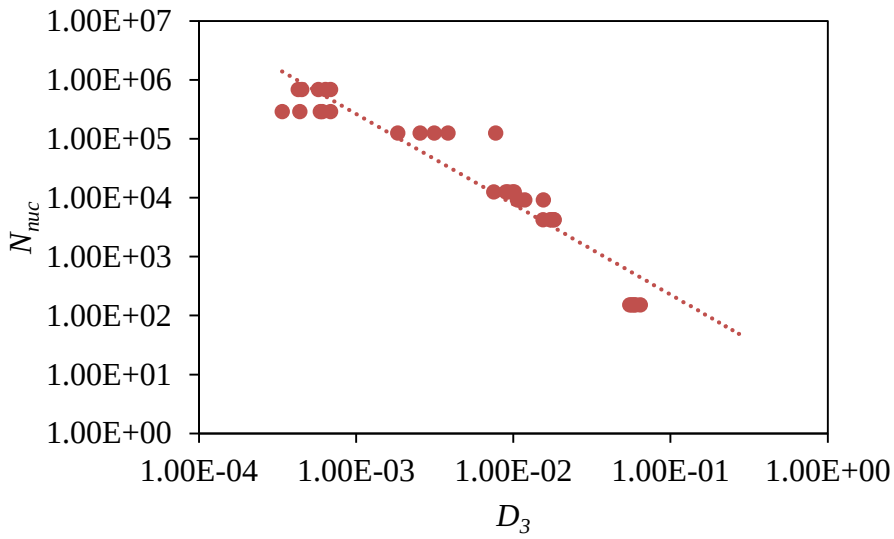

Figure 55. Calibration of estimated nucleation lives to parameter D_3.

In addition to the estimates of nucleation provided by Xue et al., a comparison is also made to an observed particle nucleation life at 0.4% strain claimed by Tokaji et al. [125] to occur at 5,670 cycles. This estimated nucleation life is slightly less than the minimum predicted nucleation life of 6,930 cycles from five distinct orientations.

This calibration indicates that the assumed initial crack plane in the nucleant particle could represent a potential retarding factor for crack nucleation in shear of Al 7075-T6, which to the author's knowledge has not been previously discussed. To verify this initial crack plane and the intrinsic effect on the fatigue lives of the alloy, an additional investigation was performed to study the sensitivity of the various damage parameters to the load condition and crack angle. An ellipsoidal particle aligned in the y-direction with $a = 10\mu$m and $b/a = c/a = 0.5$ is used represent a typical fractured particle within a single crystal matrix, similar to the previous study. Cracks through the center of the particle with angles of 0, 11.25, 22.5, 33.75, and 45° to the rolling direction are applied using the same stiffness reduction technique and again the damage parameters are studied over three simulated loading cycles for representative loads of 0.4% for uniaxial and 0.2% for shear.

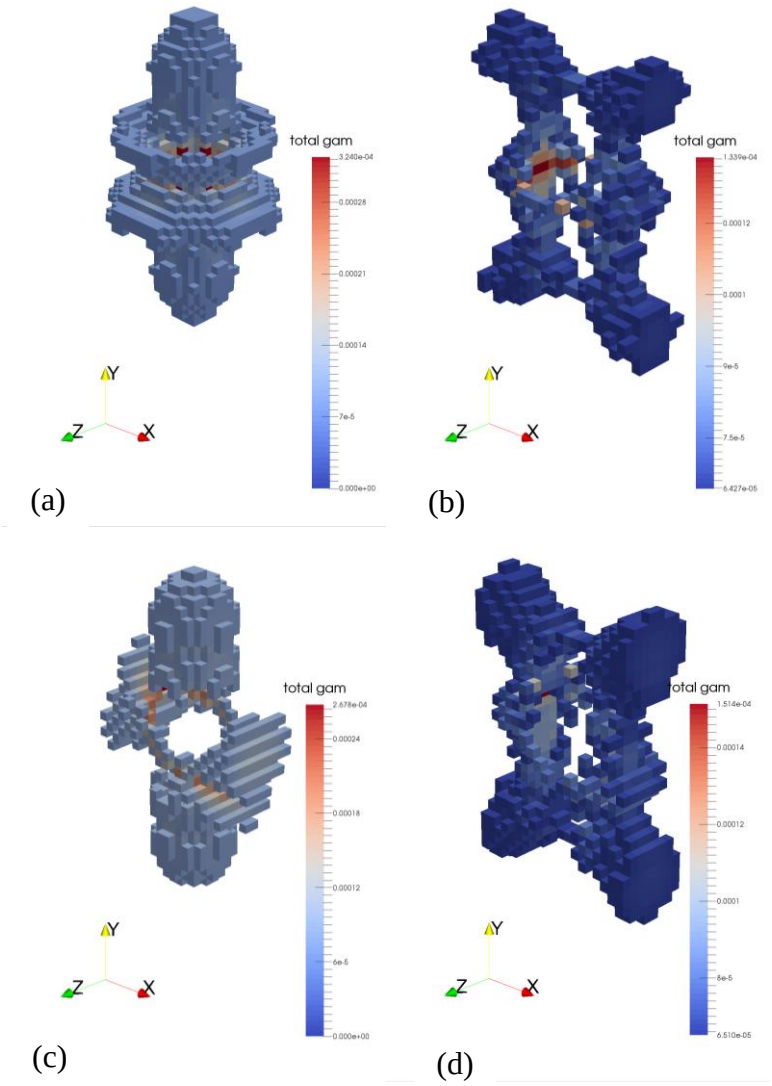

Figure 56. Nucleation parameter fields around the cracked particle for uniaxial loading of 0° crack (a) shear loading of 0° crack (b) uniaxial loading of 45° crack (c) and shear loading of 45° crack (d).

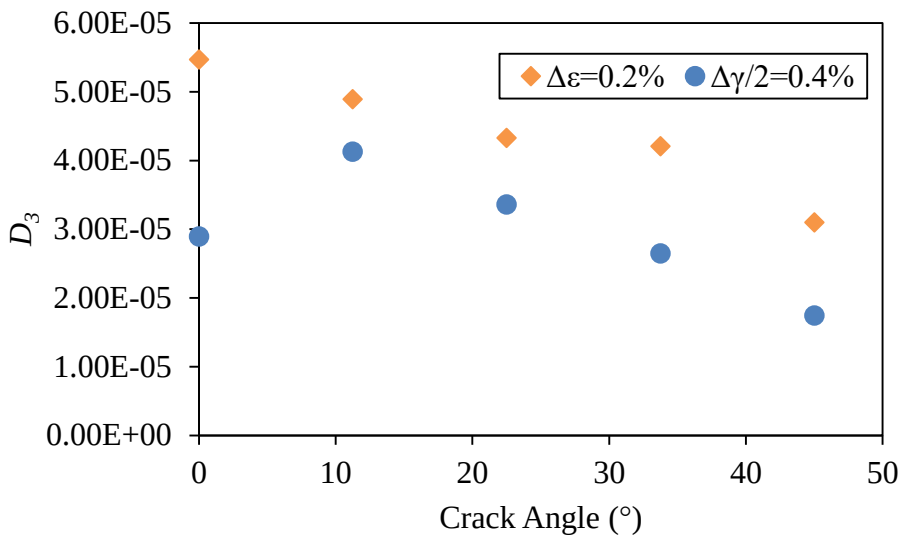

Figure 57. Damage parameters as a function of crack inclination angle for applied shear (a) and uniaxial (b) load conditions.

Both the uniaxial and shear simulations have a strong negative trend for nucleation parameter as a function of crack angle. Both loading conditions show scatter in the nucleation parameter on the order observed for the different crystallographic orientations. This represents a potentially compounding factor for fatigue life scatter, as anticipated by experimental observations by multiple authors [10, 11, 126] with distributions of particle crack angles being centered along principal stress direction. Interestingly, the trend for uniaxial and shear are relatively similar. This conflicts with the initial assumption that the crack orientation from processing provides a mechanism for the retardation of nucleation onset.

It is important to note that these conclusions are not definitive. The voxelated mesh and damaged element approach to crack modeling provides a reasonable estimate but are not appropriate to capture crack sliding friction. The return to initial stiffness when the crack plane is under compression may overestimate the sliding friction of the crack and in turn, underestimate the accumulated slip neighboring the crack mouth.

5.3: Crack Propagation

As in any field attempting to model complex phenomena, assumptions must be made. For HCF, one assumption that is commonly applied is the existence of a single, dominant crack for a given volume instantiation. This is often assumed due to explicit stress raisers or more involved assumptions about nucleation location and interaction distance between propagation cracks. These factors, coupled with the relatively high percentage of total life (~90%) spent in the microstructurally small crack growth regime, indicate that the life-limiting crack will not experience significant interaction effects or crack coalescence during the MSC growth phase [127, 128]. Conversely, high frequency multi-site crack initiation and propagation dominated fatigue lives in LCF limit the application of these assumptions and more complex models must be developed to consider these factors.

Any crack propagation approach must address three core problems to be able to advance the crack in space and thus in simulation time. These three features are common across the mesoscale crack propagation approach of Castelluccio and Hennessey as well as the post-processing radial crack propagation of Musinski [49] and will be addressed for the selected method used in this work. These three core attributes are:

- Crack extension algorithm
- Local crack propagation rate
- Local crack propagation plane

The selection of the base crack extension algorithm will likely inform the approaches selected for the remaining features and will be addressed first. This selection will also determine calibration strategies required, crack growth statistics, and any assumptions that must be made. The extension algorithm devised for this work is similar to that of Musinski in that a perimeter of distributed points are propagated radially outwards with local sensitivity to the crack growth rate and plane. In the chosen approach, however, explicit modelling of the crack is performed during the simulation by

the aforementioned damage application method. Conducting crack extension and explicit modeling during simulation has the benefit of incorporating stress redistribution effects into the following crack propagation steps. Similar methods have been applied for more simplified material models in 3D (e.g. XFEM) as well as with crystal plasticity in 2D [129], and have demonstrated this dependence.

This compares favorably to the implicit application of stress intensification as a post-processing step requiring extensive calibration that may still lack sufficient description of the local microstructure and loading conditions to adequately capture stress redistribution effects. The main drawback is the additional computational time required for each additional stress redistribution step compared to a constant number of steady state cycles simulated for the post-processing application. The same is true, however, for the mesoscale extension algorithm used by Castelluccio and Hennessey, which also must approximate FIP redistribution through the interior of grains. Such a calibration should not be necessary if sufficient mesh density is used.

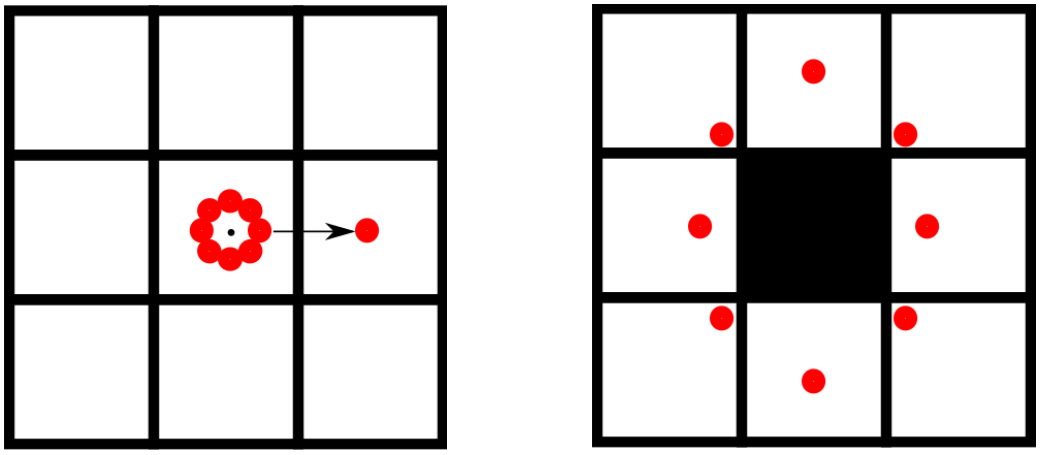

Figure 58. 2D illustration of the point propagation method with initial distribution of points (left) and at a later time (right) with the previously occupied element (black) now being damaged.

With the basic method selected, a detailed pseudocode implementation of the propagation and simulation coupled system is presented in Figure 60. Crack propagation

can only occur after the initial seeding of points in crack plane. This plane must be carefully selected since the propagation direction (Figure 59) is sensitive to crack plane normals approximately parallel to the tangential direction $\mathbf{d\theta}$. The plane in which the propagation points are seeded is selected such that the normal direction is parallel to the eigenvector associated with the maximum principal stress. This selection best approximates the Stage II crack propagation plane. Since a cyclic stress state must be established, at least one loading cycle is necessitated.

Crack propagation occurs using a local coordinate system defined by the crack plane and point seeding location. For each sensing point along the crack perimeter, the radial direction $\mathbf{r}$ and tangential direction $\mathbf{d\theta}$, are known as well as the seeding plane of the crack $\mathbf{n_c}$. Following computation of the intermediate Stage II propagation plane, the propagation direction $\mathbf{p}$ is found by the following

$$\mathbf{p} = \mathbf{d\theta} \times \mathbf{n}_{\text{int}} \tag{56}$$

with the direction corrected to ensure propagation with increasing crack length (away from the crack center). This formulation ensures that the propagation remains radial in nature with deviations in crack height arising from the propagation plane. The propagation rate may then be applied to this local direction along with a number of cycles to determine the final point location.

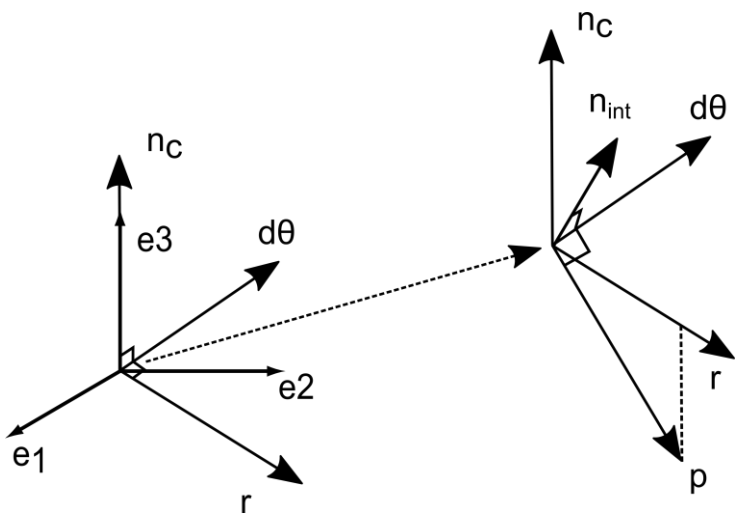

Figure 59. Crack propagation direction p selection from local crack plane normal n_{int} using local coordinate system r, dθ, n_c. Crack plane normal determined by Stage I or Stage II approach.

Algorithm 1 Propagate Crack

$PerimeterElements = GetElements(PointLocations)$
$NeighborWeights = GetNeighborWeights(PointLocations)$
$PropagationRates = GetPropagationRates(PerimeterElements, NeighborWeights)$
$PropagationPlanes = GetPropagationPlanes(PerimeterElements, NeighborWeights)$
$MaxRate = max(PropgationRates)$
$PropagationCycles = d_m/mean(PropagationRates)$
$PropagationIncrement = ElementSidelength/MaxRate$
for each integer $i \in [0, PropagationCycles/PropagationIncrement]$ **do**
    for each $Point$ in $PointLocations$ **do**
        $UpdatePoint(Point, PropagationRates, PropagationPlanes, PropagationIncrement)$
        $UpdateElement(Point)$
        if $IsLost(Point)$ **then**
            $RecoverElement(Point)$
        end if
    end for
end for
Return $PointLocations, PropagationLife$

Figure 60. Point propagation pseudocode for crack extension during simulation.

The crack propagation method is implemented within the same framework as the mesoscale propagation approach by the use of a Python script providing crack information to the UMAT via the UEXTERNALDB. Local stress, strain, and FIP fields are used to inform a single step of the crack propagation method. The new crack geometry is conveyed through an updated *cracked_elem.txt* file with cracked elements

and crack plane normal used to perform damage updates. The cycle is repeated with the newly damaged elements creating stress redistribution and updating the field values to inform the next crack propagation step. This information exchange is illustrated in Figure 61.

Once the nucleation step with crack seeding has occurred the FIP fields inform the crack propagation by Figure 60. The mesoscale propagation distance d_m is the average propagation distance allowed in a single crack step. In a voxelated mesh, this is set to the element sidelength to ensure the perimeter does not expand by more than one element in each direction. In addition, since connectivity information is only directly stored for neighboring elements in the mesh, the outer loop minimizes the possibility of a point becoming "lost" by propagating beyond a neighboring element. In the event of a "lost" point, the entire mesh is searched to find the enclosing element.

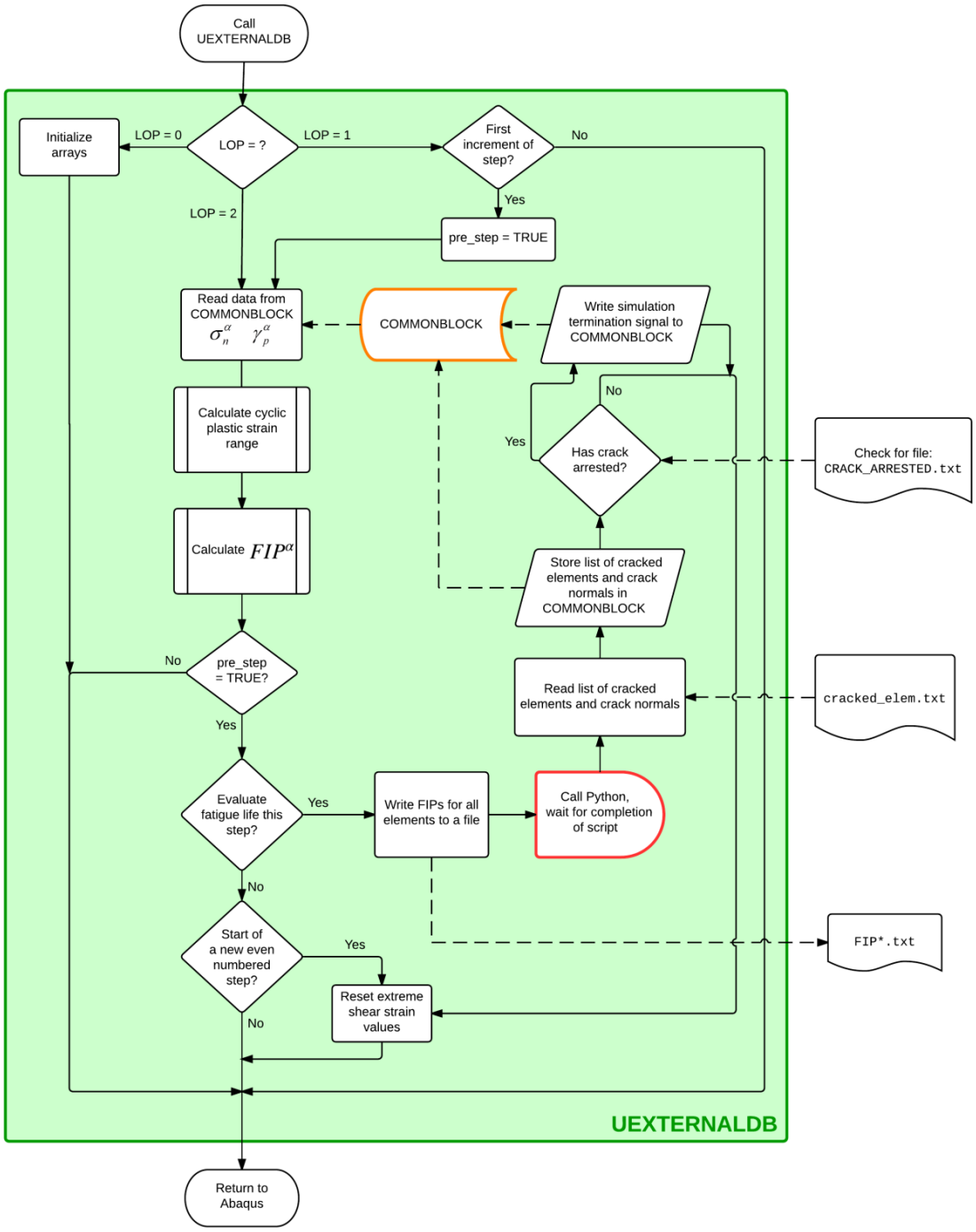

Figure 61. Flowchart of crack propagation simulation information exchange between Python and Abaqus UEXTERNALDB [48].

An additional feature of the Python implementation of the crack propagation method is that simulation states are only required as text files. This allows for the

application to uncracked data sets as a post-processing analysis similar to the method detailed by Hennessey [48]. This is mostly useful for debugging and development as the FIPs are lower without the intensification caused by simulating the crack.

Impetus for selecting an improved propagation method was provided when attempting to obtain crack path statistics by applying the methods of Hennessey to determine geometric properties of Stage II propagation behavior in Al 7075-T6. Since the mesoscale algorithm does not have a true definition of a crack front, various crack shapes were obtained which are not noted in the literature. Often void-like arrangements of fractured grains or large bifurcated paths may be observed. In addition, the incremental crack length shown in equation (41) is not physically representative of the total crack length, as evidenced by the fact that simulated cracks are grown to length of 80 μm within a 50 μm volume. This problem is avoided by explicitly modeling the perimeter of propagating points in the selected method.

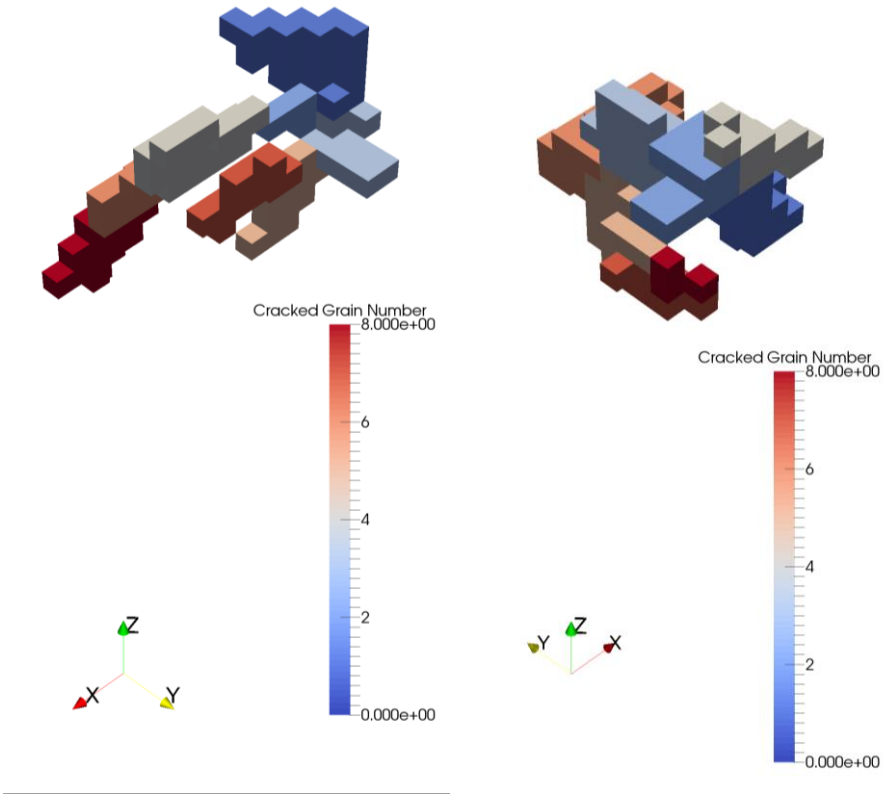

Figure 62. Poorly defined crack propagation paths created by the mesoscale propagation algorithm.

Discussion of the selected method would be remiss without mentioning the negative features of the approach. Since the crack propagation plane and rate are selected locally and the mesh density determines an extension distance, mesh refinement could potentially have a significant impact on propagation simulations. This is especially problematic for the same reason that explicit integration schemes are discouraged for numeric solvers of partial differential equations (PDE). Since the solution varies in space, insufficient meshing density could cause problems typically associated with a stiff PDE such as overshooting and a lack of convergence to true value (crack plane). These concerns must be weighed with the computational efficiency of the model as well, though the mesoscale crack propagation distance may be selected to balance mesh fidelity, stress redistribution, and propagation behavior. In addition, some more advanced crack metrics

such as roughness may be gathered using this method, however a lack of appropriate crystallographic information coupled with experimental data preclude the validation of such statistics.

The second fundamental question to answer is the determination of the local crack propagation rate. Since the selected encapsulating approach attempts to redistribute stresses at a consistent, if not infinitesimal, manner, the method to determine crack propagation rate can be somewhat simplified. Inheriting a model, which can trace its origins to the RR1000 model of Castelluccio, the initial crack growth rate formulation appeared in equation (43) with several extraneous terms. Crack growth rate in RR 1000 is accelerated in grains of larger diameter, in addition to being influenced by low-misorientation neighbors to effectively create super-grain structures, which act to increase crack growth rate further. These effects are incorporated into the crack growth law via the β_i term, which is computed using

$$\beta_i = \frac{1}{d_{gr}^{ref}} \left(D_{st} + \sum_{j}^{n} \omega^j D_{nd}^j \right) \tag{57}$$

In this formulation, d_{gr}^{ref} is the reference grain diameter for calibration, j indexes over neighboring bands with D_{gr}^j being the neighbor band length and $\omega^j = \langle 1 - \frac{\theta_{dis}}{20} \rangle$ is the disorientation factor and D_{st} is the current grain diameter.

Exploration of the literature regarding crack growth rates in Al 7075-T6 does not indicate a strong correlation between crack growth rate and average grain size. Donnelly and Nelson [130] observed no significant impact on grain size relative to crack propagation for rotating specimens and a grain size ratio of 1:4 in the propagation direction. Zurek et al. [131] discovered a secondary influence of grain size on propagation rate, mostly attributed to the development of crack closure and residual stresses near the surface. These effects diminished under decreasing load amplitude and could likely be captured by the propagation through appropriately modeled grains with

the proposed method. Thus, the inclusion of a grain size dependent factor is not deemed necessary. Furthermore, since the subgrain propagation is explicitly modeled, the normalized crack length factor and thus the scaling function for the subgrain $FIP(a)$ is not necessary as well. Finally, the misorientation factor is also assumed to be addressed to a greater extent by the compatibility of grain boundary deformations in the crystal plasticity model.

As previously mentioned, the ΔCTD value has been found to be a fundamental parameter linked to crack growth rate. This fundamental relationship is often used to train additional correlations to account for stress redistribution either in post-processing [49] or over larger grain-sized increments in crack growth [47]. Due to the inherent ability of the crack propagation method to capture some of these influences during the FEM simulation via stress redistribution, only the most fundamental relationship is retained between ΔCTD and FIP. This leads to the following crack growth formulation

$$\left.\frac{da}{dN}\right|_{msc}^{\alpha} = \phi\left\langle A\left(FIP^{\alpha}\right) - \Delta CTD_{th}\right\rangle \tag{58}$$

To better approximate the finite volume over which the crack propagation process takes place, neighbor weights based on relative distance within the mesh and an averaging scheme is used to represent the non-local crack growth. Neighbor weights w_{i+n} found for a sensing point at location $\mathbf{x}_i$ and nearest point at $\mathbf{x}_{i+n}$ are related by the following formula with the d_w value selected to represent a process distance less than one half the average ND grain thickness (12 um).

$$w_{i+n} = \frac{\left\|\mathbf{x}_{i+n} - \mathbf{x}_i\right\|}{d_w} \tag{59}$$

The final feature to be addressed is the selection of the local crack plane. Given the early transition to Stage II crack propagation observed by various sources [8, 132] for Al 7075-T6, it is desirable to capture the behavior of multiple activated slip systems to

describe an intermediate crack propagation direction. Musinski and Hennessey have used such a method for addressing combined crack propagation rates using a weighted averaging scheme where $\mathbf{n}_{INT}$ is the intermediate plane selected as the weighted average from n candidate slip systems with slip plane normals $\mathbf{n}_i$. Here the weights are determined by the crack driving force for each candidate plane FIP_i.

$$\mathbf{n}_{INT} = \frac{\sum_{i=1}^{n} \mathrm{FIP}_i \cdot \mathbf{n}_i}{\sum_{i=1}^{n} \mathrm{FIP}_i} \tag{60}$$

The method has a fundamental geometric flaw, however. Since the Hessian form of the plane may be equally described by $\mathbf{n}$ and $-\mathbf{n}$, two possible intermediate crack planes arise. The representation of slip plane normals may not be known a-priori by the crack propagation algorithm, thus this must be treated in a general sense. A consequence of this indeterminate expression of the intermediate plane is the selected plane may not maximize the crack growth rate. In this case, the propagation would occur across a large misorientation in planes. This is undesirable as observations indicate that crack propagation across large misorientations is highly unfavorable [8, 133]. This problem is created by the indeterminate expression of the plane normal in 3D and is illustrated in Figure 63. Of the two $\mathbf{n}_{INT}$ one clearly reflects a more realistic interpretation of weighted plane averaging process. A formulation is introduced which alleviates this indeterminate nature and ensures the creation maximal propagation planes from the candidate slip planes.

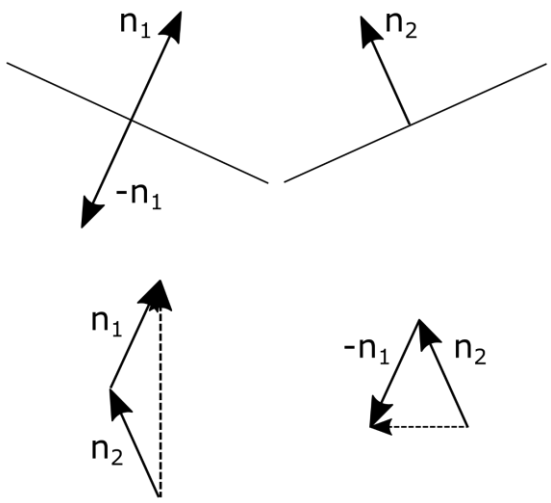

Figure 63. Two possible intermediate crack planes using the weighted normal method caused by the indeterminate direction of the individual crack plane normals.

First, a series of propagation vectors are constructed from the candidate planes and propagation rates and sorted by magnitude

$$\mathbf{V}_i = \frac{da}{dN}_i \mathbf{n}_i, \quad \|\mathbf{V}_1\| \geq \|\mathbf{V}_2\| \geq \cdots \geq \|\mathbf{V}_n\| \tag{61}$$

Working from the highest propagation rate to lowest, the candidate vectors are added to the total propagation vector such that the sum always increases.

$$\mathbf{V}_{INT,i+1} = \mathbf{V}_{INT,i} + \begin{cases} \mathbf{V}_{i+1}, & \mathbf{V}_{INT,i} \bullet \mathbf{V}_{i+1} \geq 0 \\ -\mathbf{V}_{i+1}, & \mathbf{V}_{INT,i} \bullet \mathbf{V}_{i+1} < 0 \end{cases} \tag{62}$$

The intermediate plane normal is extracted as the unit vector parallel to the net propagation vector.

$$\mathbf{n}_{INT} = \frac{\mathbf{V}_{INT,N}}{\|\mathbf{V}_{INT,N}\|} \tag{63}$$

Finally, the effective crack propagation rate as projected onto the selected intermediate plane may be determined by the norm of the final propagation vector.

$$\frac{da}{dN}_{INT} = \|\mathbf{V}_{INT,N}\| \tag{64}$$

Initial application of the new crack propagation method has yielded encouraging results. Several crack propagation paths are reproduced to demonstrate the general behavior of the method. Note that for both shear and uniaxial load conditions, the Stage II crack propagation plane is well preserved in that they both appear to propagation predominantly in the plane of maximum normal stress.

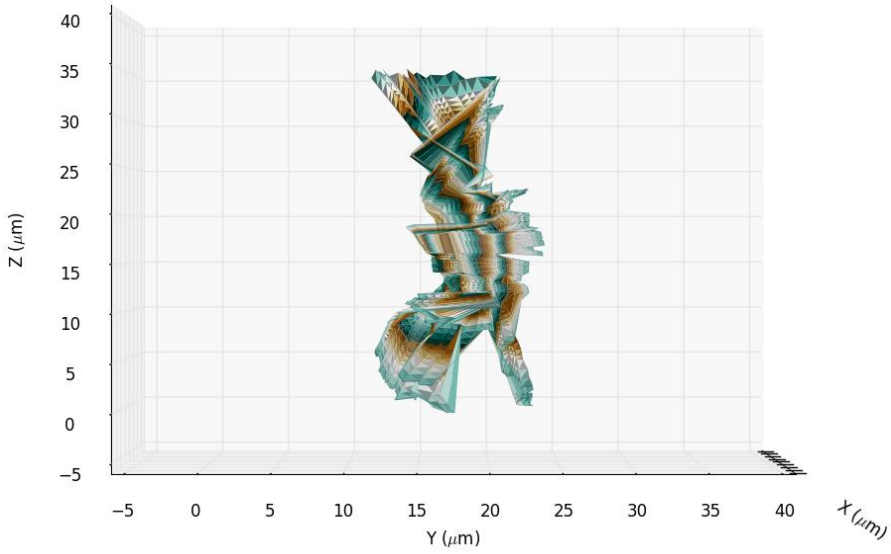

Figure 64. Simulated crack using Stage II point based propagation at 0.4% strain amplitude tension-compression $R_\varepsilon = -1$ in the y-axis. Color-coding indicates iso-life contours.

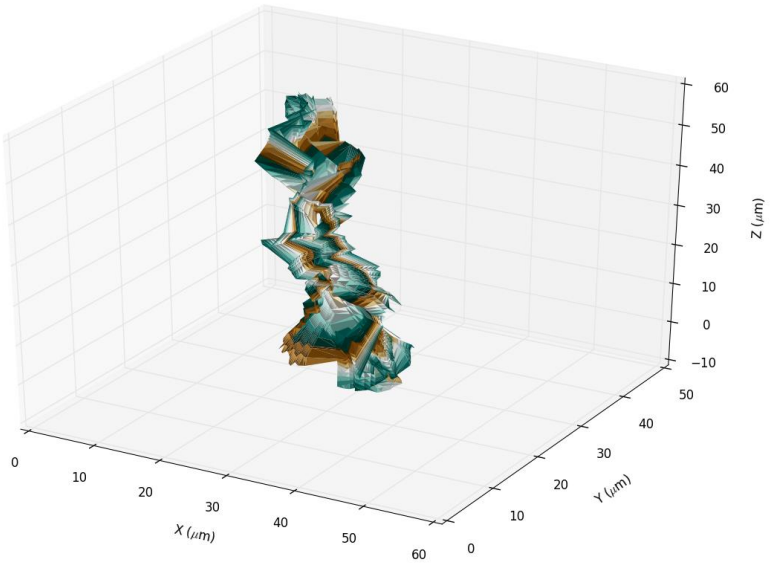

Figure 65. Simulated crack using Stage II point based propagation at 0.4% strain amplitude in XY-shear with $R_{\varepsilon} = -1$. Color-coding indicates iso-life contours.

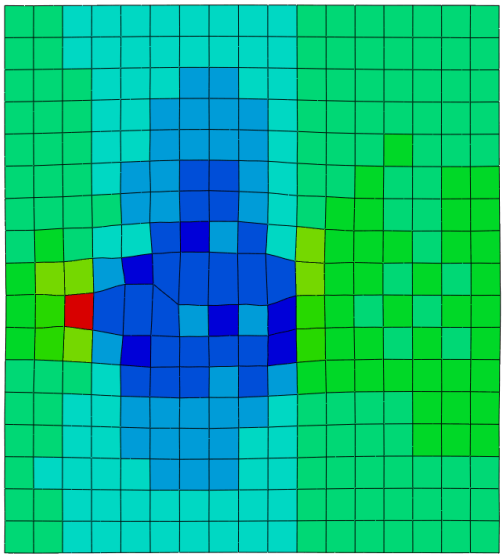

Figure 66. σ_{22} response during crack propagation simulation. Displacements exaggerated to highlight the highly distorted crack elements.

It is apparent that the new crack propagation method significantly improves the physical basis of crack propagation. The new method and accompanying stress

redistribution appear to better capture the Stage II crack behavior. Further exploration of these methods will be performed in later sections.

5.4: Conclusions

In this chapter, a new method for crack propagation was proposed and the implementation explained. This new method combines a radial crack propagation with explicit crack modeling to capture stress redistribution effects. An additional geometric constraint was introduced to handle the construction of an intermediate slip plane in 3D to best match the physics of slip transfer. These combined methods will be calibrated and used to study crack behavior in Al 7075-T6 in the next chapter.

CHAPTER 6: MICROSTRUCTURALLY SMALL FATIGUE CRACK GROWTH MODELING IN AL 7075-T6

6.1: Synthetic Microstructure Representation

Since crystallographic texture and grain morphology have a significant impact on MSC growth, it is desirable to represent the experimental morphology more accurately before attempting to assess fatigue lives that may be dependent upon load orientation and microstructural features. Previously for Al 7075-T6, microstructures were instantiated using a separate code, which constructed equiaxed, randomly textured grains. With the introduction of the material simulation pipeline, it is relatively simple to incorporate additional information into the fatigue simulations of Al 7075-T6.

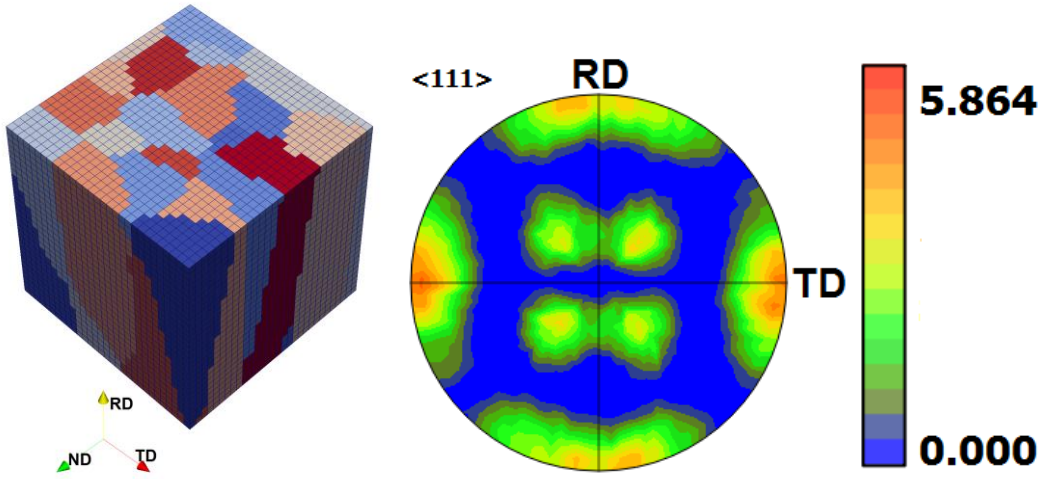

Figure 67. Sample rolled microstructure and associated target pole figure.

Using Dream.3D, a description of the rolled microstructures commonly associated with Al7075-T6 was developed from various experimental observations. Zhao and Jiang [80] note equiaxed grain sizes from 10 μm to 40 μm perpendicular to the rolling direction, with a rolling direction grain size of approximately 70 μm. From these observations as well as those of Turkmen et al. [134], an average grain size of 15 μm was

chosen with an aspect ratio of 7:1:1 for the R:T:N directions respectively. In addition, the pole figures of both Turkmen et al. [134] and Narayanan et al. [135] were used to create a rough approximation of the texture developed in rolled 7075-T6 aluminum. A log-normal grain size distribution was again assumed with a standard deviation of 4 μm. Dream.3D was used to create simulated microstructures with an axis orientation function aligning the a-axis of the ellipsoidal grain to the rolling direction of the simulated volume with a noise factor to represent imperfectly aligned grains. Uniaxial simulations are typically loaded in the RD to match experiments performed by Zhao and Jiang [80] and others which impose load along the RD. Misorientation and neighbor size distribution were assumed to reflect statistical averages as calculated by Dream.3D given a lack of experimental observations readily available in the literature. A sample microstructure is depicted in Figure 67.

6.2: FIP Intensification under Varied Load Conditions Due to Stringer Distribution

In addition to the reformulation of the nucleation simulation, additional parameters were investigated to ascertain the impact on the difference in observed fatigue lives between the uniaxial and shear load conditions. Given the consistent application of uniaxial loads applied to the RD and the highly anisotropic distribution of constituent particle stringers in the material, it was hypothesized that these distributions may contribute an accelerative growth factor for uniaxial loading that is not reflected in the present propagation calibration.

To accurately represent the spatial distribution of particles in the alloy, a neighborhood optimization routine developed by David Turner of the Kalidindi group at Georgia Tech was used. The functionality of this tool is described in depth in [136], however the core functionality is to use information from three orthogonal planes to optimize a microstructure instantiation to match individual pixel (microstructure

function) neighborhood values. Microstructure scans from Rollet et al. [87] were used to represent the particle distribution along the RD-ND, RD-TD, and TD-ND planes.

Since the reconstruction is a volumetric region, the 2-point statistics are likewise volumetric. For comparison the 2-point statistics of the exemplar images, 2D slices of the 3D statistics are taken in the RD-TD plane. The set of statistics on a plane through the center of the 3D space of 2-point statistics represent correlations between locations whose spatial locations differ only within the plane, and do not have any displacement in the remaining dimension. This allows direct comparison of the microstructure scans and reconstruction. Figure 68 compares the auto-correlation of the particle phase along the rolling direction (x-direction of the reconstruction) for 10 reconstructions and 6 exemplar scans.

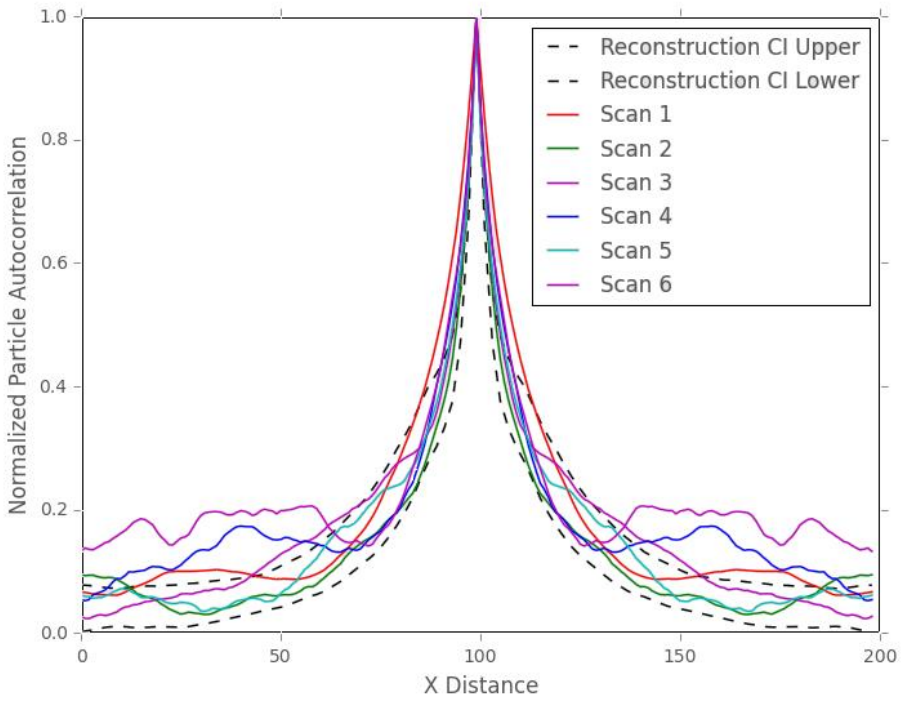

Figure 68. Validation of the particle stringer reconstruction using 2-point statistics. Note that confidence bounds capture the majority of the sampled microstructure scans from varied sources [11, 87]. First neighbor effects are well captured in the 74-124 region.

A crystal plasticity simulation of the 200x200x200 element reconstruction generated would be intractable with the computational resources available. In addition, the stress states are expected to be dominated by the relatively high stiffness contrast (~2) between the particle and matrix phases. Material Knowledge System methods (MKS) have demonstrated successful application to material systems with this range of elastic modulus contrast [72]. Ongoing research is being performed to investigate calibrations of higher order statistics to perform localization of non-linear phenomena and higher contrast materials. These models have significant additional complexity and require significantly larger amounts of data to calibrate. Since the behavior of interest occurs primarily in the HCF regime with relatively small strains, a simpler form of localization will be applied treating the material as linear elastic [72].

Influence coefficients were calibrated for all six components of the strain tensor using 21^3 element delta microstructures (single particle phase at the center of the matrix phase). Following validation of the method as applied to five random microstructures of the same size, the influence coefficients were padded to allow for prediction of the full 200^3 reconstruction volume.

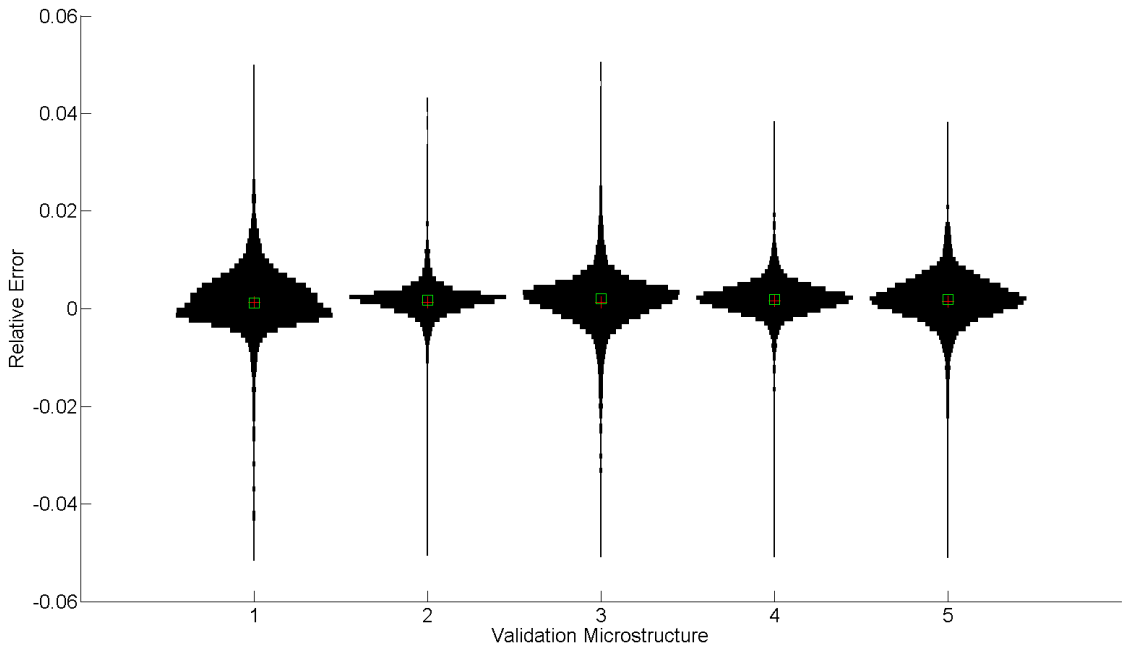

Figure 69. Relative errors of MKS prediction compared to crystal plasticity simulation of ε_{22} (loading direction) for each element in five validation microstructures of size 21x21x21.

A simple isotropic hardening law is applied to fit the small amounts of plasticity that develops in HCF. The von-Mises stress is used to interpolate the expected plastic strain, from which the Fatemi-Socie FIP is calculated on an element by element basis. The total distribution of FIP values may then be used as a comparative measure of the anisotropic constituent stringers impact on the fatigue life of the alloy.

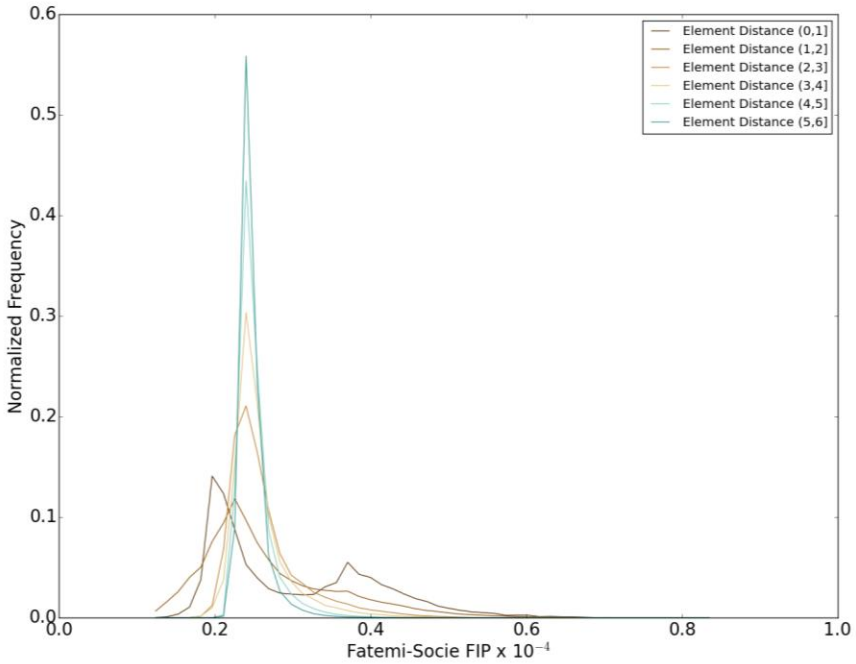

Figure 70. FS FIP intensification near particle stringers under uniaxial loading of 0.2%.

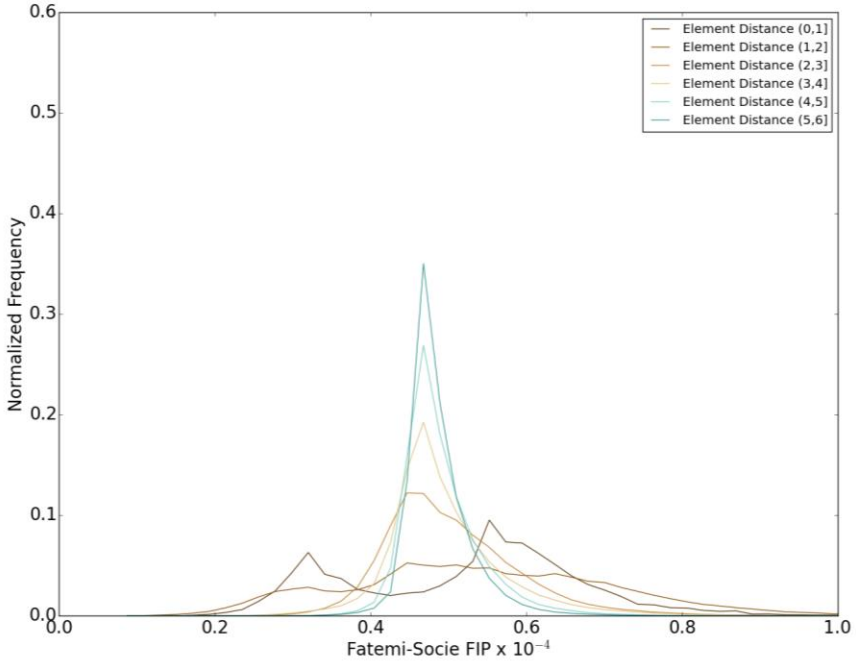

Figure 71. FS FIP intensification near particle stringers under shear loading of 0.4%.

As anticipated, the particle presence produces an intensification effect in both loading conditions. As the distance from the particle increases, the FIP distribution condenses to a far-field impulse function (omitted for clarity). Note the presence of secondary peaks for both the uniaxial and shear load conditions. These peaks indicate the different intensification levels produced by the particle stringers. For uniaxial loading the ratio is ~1.5x while for shear the ratio is closer to 1.25x. Unfortunately, while the anisotropic particle distribution appears to produce a stronger intensification effect for uniaxial loading when compared to the shear load case, the effect is still relatively mild compared to the overall shift in fatigue life distributions between the two loading conditions. While it would be possible to introduce a knockdown of fatigue lives based on extracting an intensification value from the MKS simulation of an imposed load condition and the mean free path of particles along the crack path, the overall effect should be negligible and is ignored for the remainder of the simulations presented in this work.

6.3: Fatigue Calibration

Once the appropriate level of model detail is determined, calibration, sensitivity analysis, and predictions can be performed using the desired model form. As a summary, the current propagation model in Al 7075-T6 will consider nucleation at previously cracked particles and propagation through a crystal plasticity model calibrated to the homogenized response. Explicitly modeled particles will not be considered during the propagation step as this would require significant additional complexity and computational costs, while initial investigations indicate that the overall effect is likely negligible.

Since the nucleation calibration was linked with the nucleation parameter selection, the last remaining step is the calibration of the propagation parameters. The current model only has a single free parameter, thus a calibration similar to the method

utilized by Hennessey is performed. A crack propagation rate of $2.14\text{x}10^{-3}$ μm/cycle is used based on the observations by Tokaji et al. [132] for cracks growing under $R_\varepsilon = -1$ and $\sigma_{max} = 270$ MPa. A fully reversed strain controlled loading of 0.4% amplitude is used to match the experimental loading. Five calibration microstructures were used and the resulting average propagation FIP value found to be $2.5\text{x}10^{-4}$. This value is combined with the constants of calibration $\phi = 0.35$ (Xue et al. [120] and McDowell et al. [128]) and $\Delta CTD_{th} = 2.86\text{x}10^{-4}$μm, the Burgers vector for pure FCC Al [120]. Solving for the fatigue coefficient yields $A = 25.6$ μm.

Following the calibration of both the nucleation and propagation laws, the prediction of total fatigue lives can be compared to experimental data. Once again, the extensive work of Zhao and Jiang [80] provides a large dataset, produced by consistently applied methodology, with which to compare the recalibrated fatigue lives. For these macroscopic experiments, fatigue lives are reported as the number of cycles until specimen failure (in two pieces), while simulation fatigue lives are estimated using a single model propagating a crack to 60 μm as per Hennessey [48].

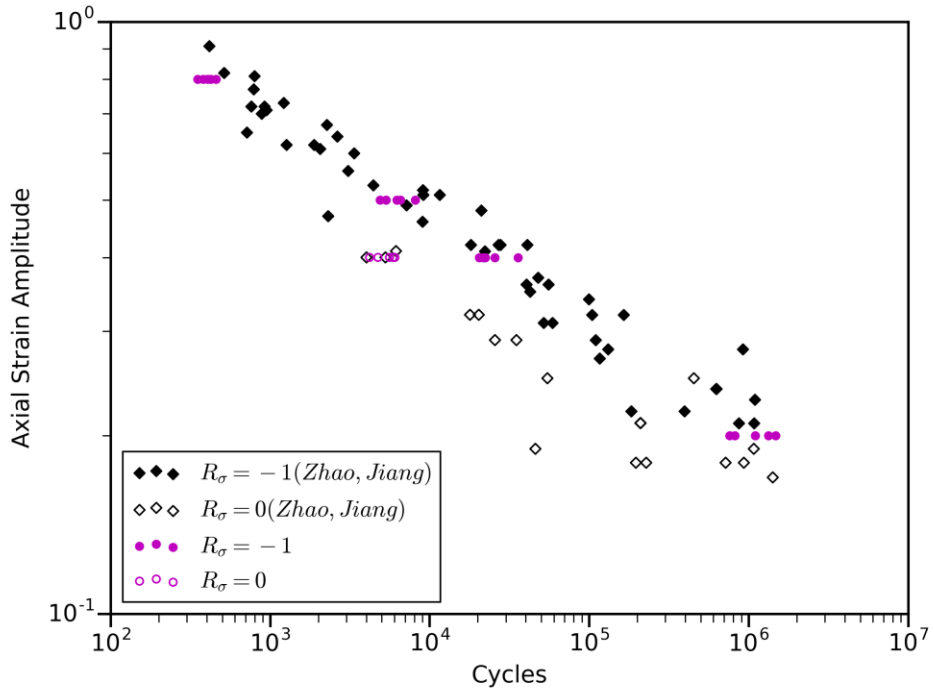

Figure 72. Comparison of uniaxial fatigue lives as predicted from simulation and observed by Zhao and Jiang [80].

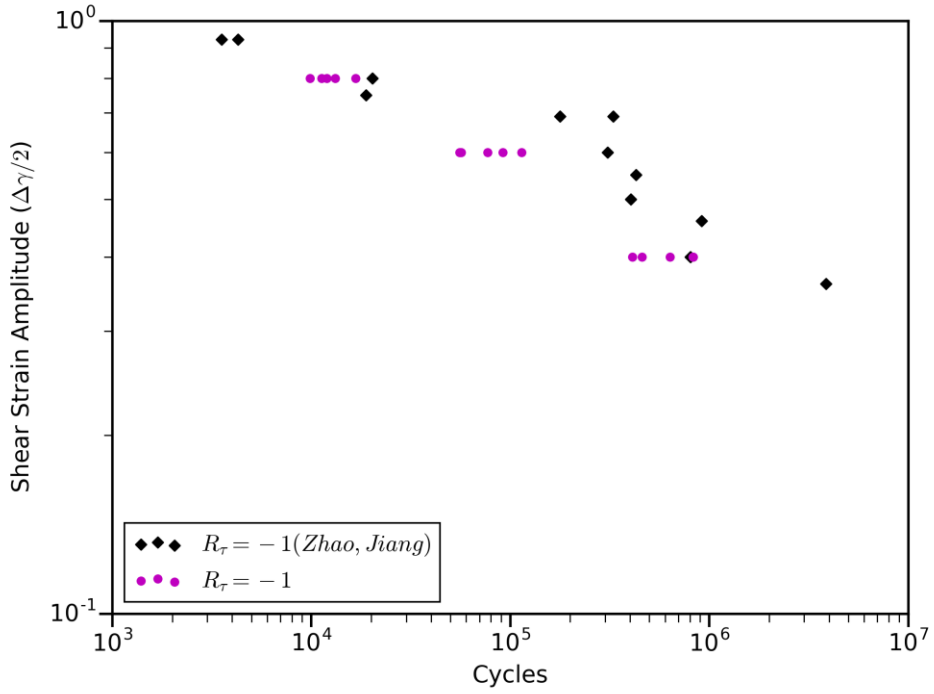

Figure 73. Comparison of shear fatigue lives as predicted from simulation and observed by Zhao and Jiang [80].

It is evident that, following the introduction of the nucleation simulations and a new propagation model, fatigue life predictions in uniaxial and shear loading conditions are well fit to the experimental data. The previously conservative estimates of shear fatigue lives are now the same order of magnitude as those observed experimentally. In addition, the uniaxial predictions appear to reflect both average response as well as the fatigue scatter associated with the data. It also appears that the introduction of the nucleation simulation provides a potential explanatory mechanism for the difference in fatigue lives under $R_\sigma = 0$ loadings. The estimated simulation lives for these loadings are in good agreement with the mean and scatter of the experimental fatigue lives.

6.4: Fatigue Life Sensitivities

Computational models always present a tradeoff between fidelity and computational intensity. For FEM simulations, the computational cost may be considered in terms of wall time (actual simulation time to completion) or the CPU-time (adjusted by number of CPUs), associated with the simulation. With a constant material model, an increased number of elements (or higher order elements) will produce a greater ability to capture gradient effects on the interior of the simulated volume. Increased mesh refinement in fatigue simulation can lead to greater resolution of crack paths, improved crack closure, stress redistribution, and eventual convergence of simulation properties. Specific issues relevant to the crack nucleation and propagation will be discussed separately, with additional discussion on methods to reduce computational costs while retaining good agreement with higher resolution models.

Nucleation simulations involve a single particle embedded in the Al 7075-T6 matrix. Because of the relative size of these features (grain size typically exceeds particle size by an order of magnitude) only a few grains are required at most to represent the local state. Such a volume does neglect the nearest neighbor affects such as grain

misorientation, however for cracked particles, it can be assumed that the crack drives the notch root deformation to a much larger extent. Reduced mesh density simulations of 10x20x10 elements were compared to the initial calibration simulations of 20x40x20. The relative error is presented for each load condition and grain orientation.

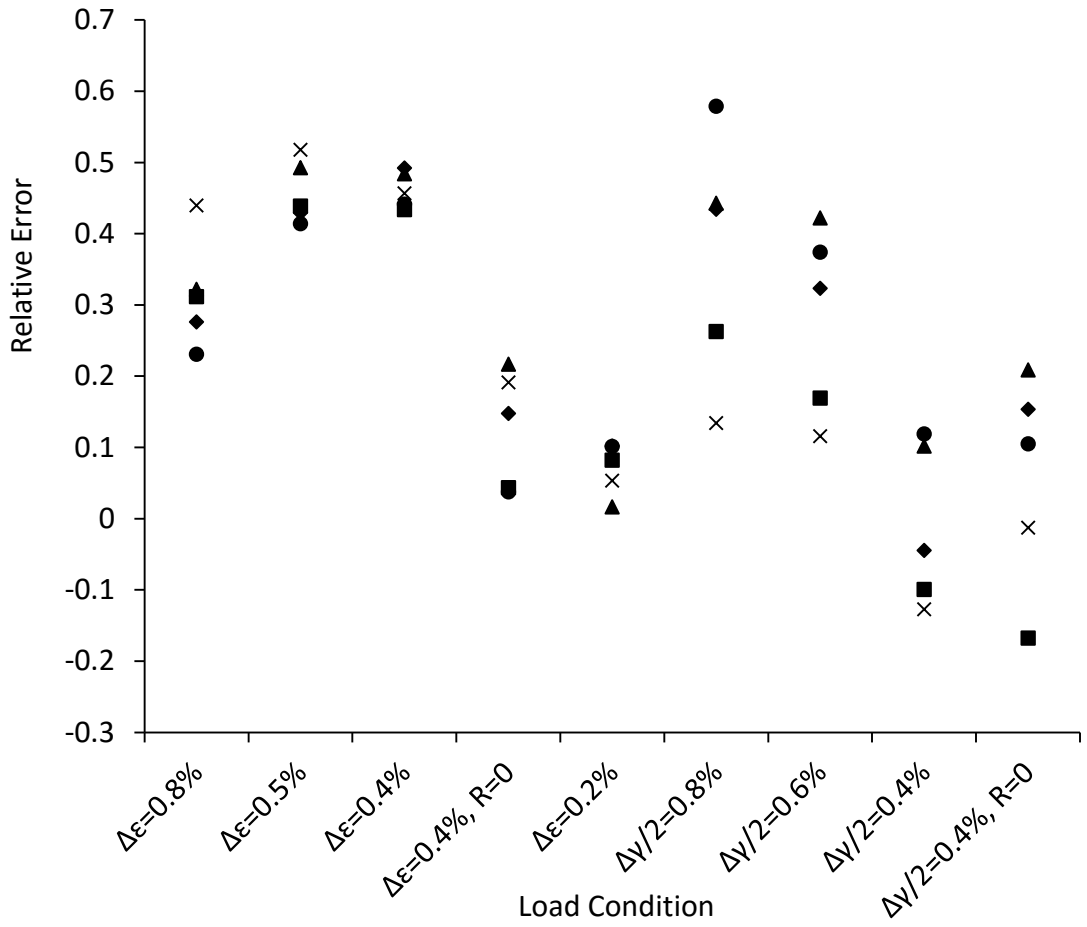

Figure 74. Relative difference in $\overline{D_3}$ for five random orientations and nine calibration load conditions.

It is apparent that a reduced fidelity model introduces significant bias into the results. All but three of the 45 simulations had lower values in the low resolution SVE simulations. It is hypothesized that the voxelated nature of the mesh leads to a smaller

sampling of the possible stress states relative to the crystallographic orientations. This is caused by the voxelated nature of both meshes and thus the smaller mesh contains fewer samples. Assuming a constant distribution of values around the crack perimeter, there will be higher variance in the smaller sample size. In addition, the maximum value was reduced by an average of 65% in the smaller mesh.

While the results indicate that the nucleation simulations are indeed sensitive to the choice in mesh size for all considered loading conditions, the relative error in life predictions is significantly smaller. This is influenced by the fact that the nucleation simulations with larger relative errors are at the LCF where propagation dominates the predicted lives. While the intermediate fatigue lives are still overpredicted by a significant margin when compared to the initial calibration with the higher SVE resolution, these lives are still within the experimental data scatter.

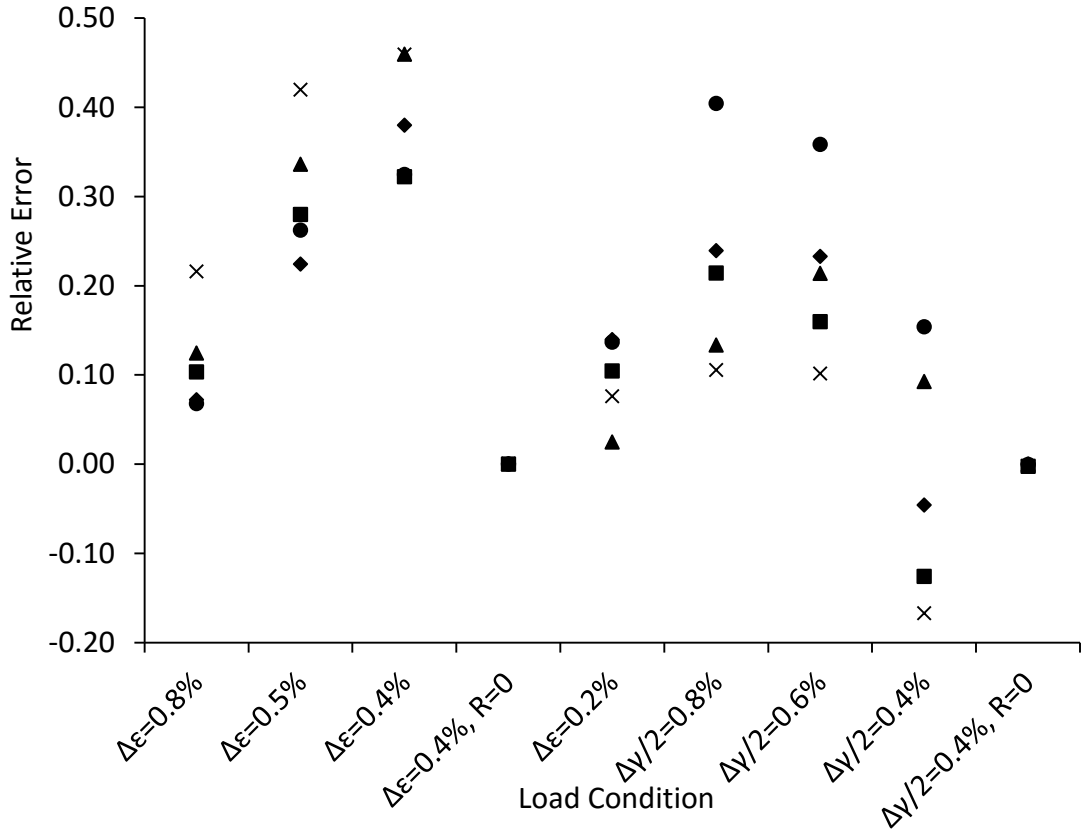

Figure 75. Relative difference in total predicted fatigue lives for five random orientations and nine calibration load conditions.

While the relatively high sensitivity of nucleation has been well established, the overall sensitivity is acceptable when compared to experimental data. The lower fidelity model is thus considered appropriate for the construction of a Γ-plane requiring hundreds of simulations. See the section entitled Multiaxial Fatigue: Gamma Plane Case Study for further information. Further reduction in model fidelity is not desirable, given the already large concessions in accuracy and precision. In addition, the lower fidelity models represent only 1.5 CPU-hours of computational time and four elements across the particle diameter.

Similar mesh sensitivity is worth considering in the context of the propagation approach developed for this material system. To isolate the effects of mesh resolution on the crack propagation results, five microstructures were simulated with varying levels of subsampling such that propagation occurs in a nominally similar FIP field. The total volume remains constant with a sidelength of 30 μm. For the observed microstructures, the crack growth rates are quite similar to the higher fidelity meshes. The crack length remains constant for some of the simulations after the points propagate outside of the volume. Proximity to the volume boundary also has a negative effect on the crack growth rate, one that will be addressed with the addition of elastic elements to model a larger volume for propagation without significant additional computation.

The mesoscale propagation distance is typically linked to the mesh resolution to take advantage of stress redistribution and local variations in crack plane. This variable was also studied, with the results for a single microstructure highlighted in Figure 77. It is evident that while differences in the mesoscale distance may not affect the initial crack propagation rate, they can change the sensitivity to local microstructure. For several of the intermediate values ($d_m = 3{,}4$ μm), the larger distance propagated before stress

redistribution does not accurately reflect the change in crack propagation rate when crossing the grain boundary ($a = 22$ µm). For this reason, d_m is currently linked to the element sidelength for voxelated meshes.

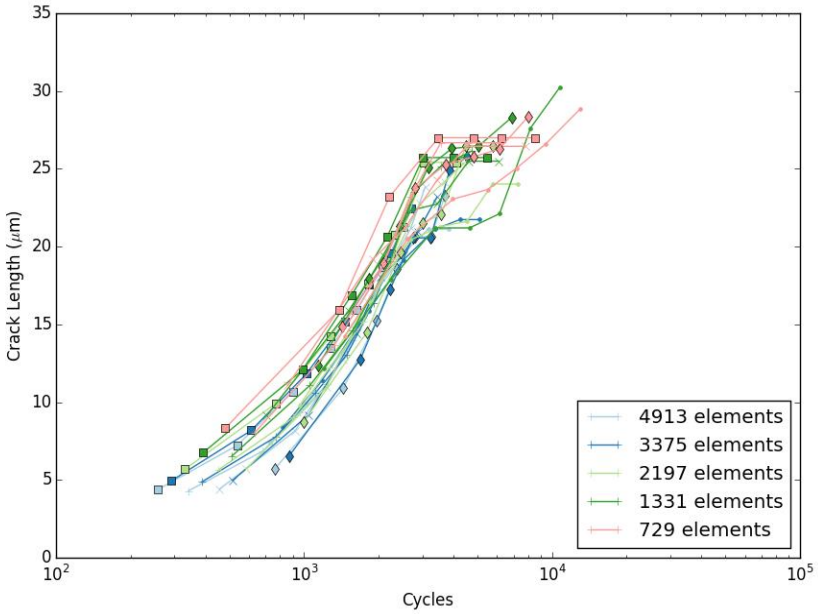

Figure 76. Crack propagation sensitivity to mesh resolution for five microstructures.

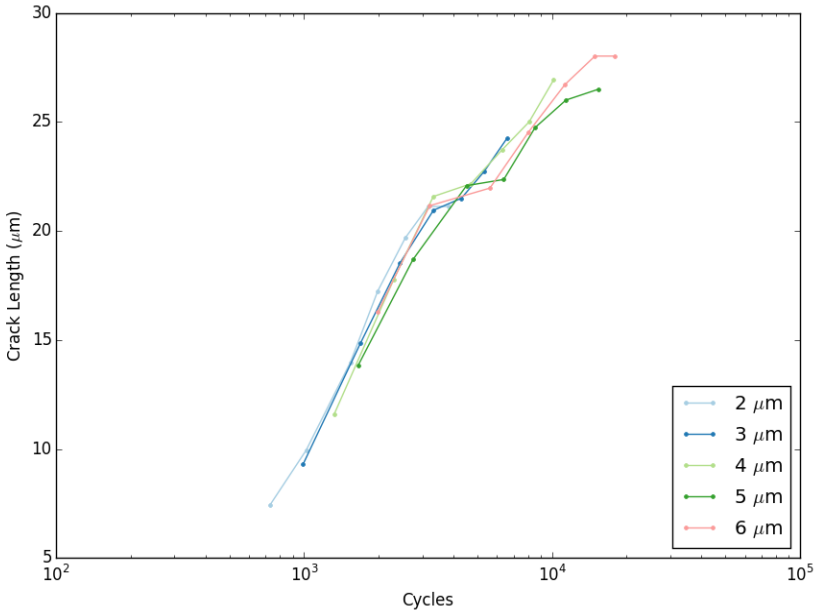

Figure 77. Crack propagation sensitivity to choice of mesoscale propagation distance.

In addition to mesh resolution, FIP intensification (for cracks of same length and microstructure) will be a function of the total percentage of the simulation volume cracked. This has been solved analytically for penny-cracks in a semi-infinite medium, however brief justification of the use of a larger bounding volume to appropriately model the stress intensification is provided in Table 6. As mentioned previously, the automated simulation pipeline supports basic Abaqus material definitions outside of the defined crystal plasticity region. This allows for a reduction of the simulation cost while preserving the crack propagation metrics relative to a large volume with crystal plasticity in the entire region. Five validation microstructures were examined across the loading amplitudes studied in this work and the results are presented in Figure 78. The elastic material definition was chosen to reflect the bulk properties of Al 7075-T6 with $E = 70$ GPa and $\nu = 0.345$. In addition to changing the crack propagation value by less than 5% the replacement of the far field region with elastic elements reduces the runtime by an average of 40%.

Table 6. Crack propagation metrics in crystal plasticity, crystal plasticity with elastic padding, and a smaller crystal plasticity volume for two crack sizes. Cracks modeled with the elastic stiffness degradation method.

Crack Size (μm)	Total Sidelength (μm)	Crystal Plasticity Region (μm)	$FIP_{p=2}$	$FIP_{p=1}$	D_3
20	92	92	2.67E-03	2.94E-03	1.05E-03
20	92	44	2.71E-03	2.96E-03	1.05E-03
20	44	44	1.36E-03	1.40E-03	6.17E-04
12	92	92	7.45E-04	3.76E-03	1.11E-03
12	92	44	7.39E-04	3.66E-03	1.09E-03
12	44	44	6.20E-04	3.00E-03	9.07E-04

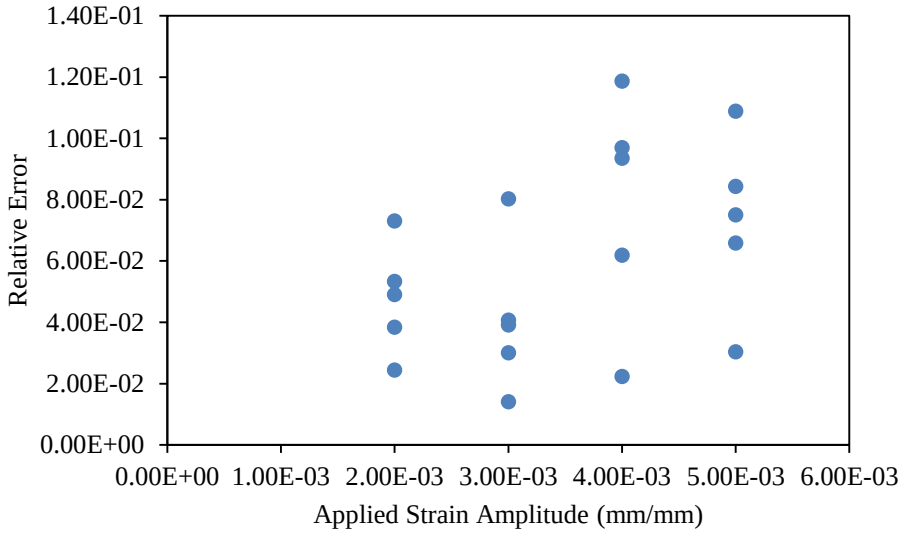

Figure 78. Comparison of crack propagation values ($FIP_{p=1}$) between partially elastic and full crystal plasticity simulations for varying loads.

6.5: Stage II Propagation Analysis

In addition to the sensitivities of the established propagation and nucleation methods, fundamental material behavior and influence on model behavior can be established. Of particular interest to Al 7075-T6 crack propagation is the activation of additional slip systems under load. Since the crack propagation algorithm constructs an intermediate plane from the weighted average (correcting for propagation direction) between two or more slip systems, it is desirable to quantify this behavior especially with regards to applied load. Six representative loads were studied with three microstructures each and the distribution of sensed FIPs was sampled along the crack front for each simulation. This yields a sampling of ~100 elements for each load condition. The relative slip system activation is studied across all slip planes, all slip systems, and the selected two propagation slip systems. Slip planes are the most concise to represent visually, requiring only three series on each chart. In addition, the slip system contains a

significant amount of redundant information as the three slip systems on each octahedral slip plane inherently decompose the total slip (and thus the total FIP) for each. For this reason, only the propagation and slip plane plots will be presented here.

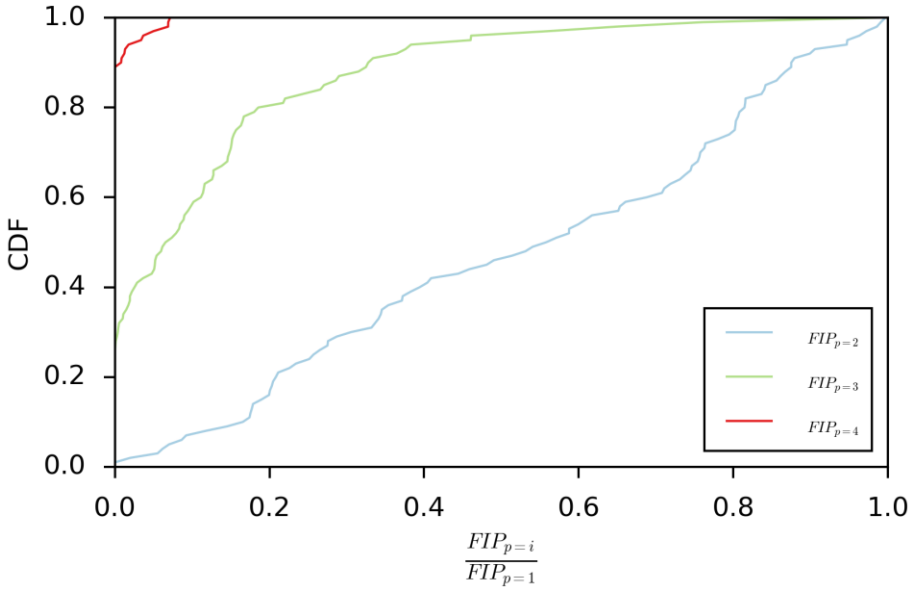

Figure 79. Slip plane ratios for three microstructures under $\varepsilon_a = 0.2\%$ and $R_\varepsilon = -1$ tension/compression.

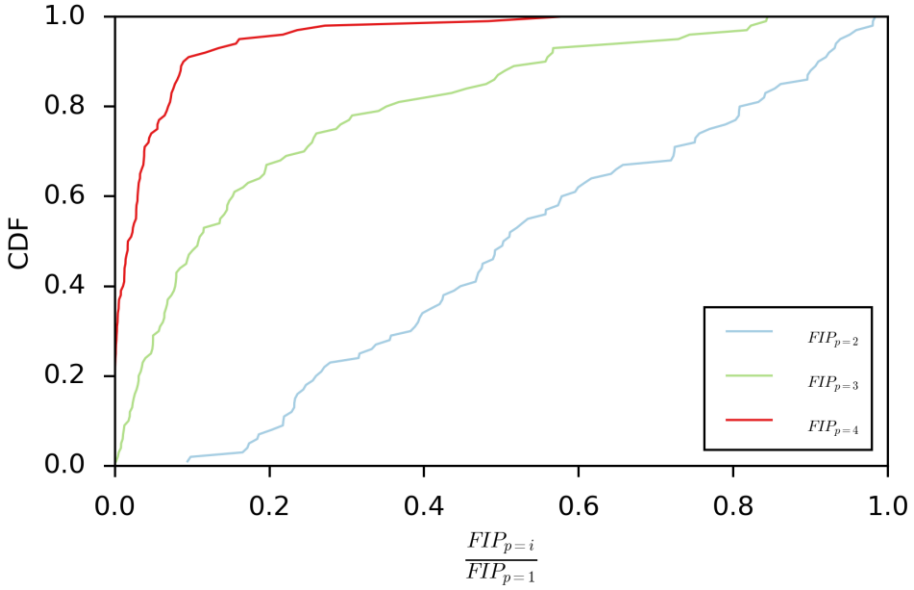

Figure 80. Slip plane ratios for three microstructures under $\varepsilon_a = 0.5\%$ and $R_\varepsilon = -1$ tension/compression.

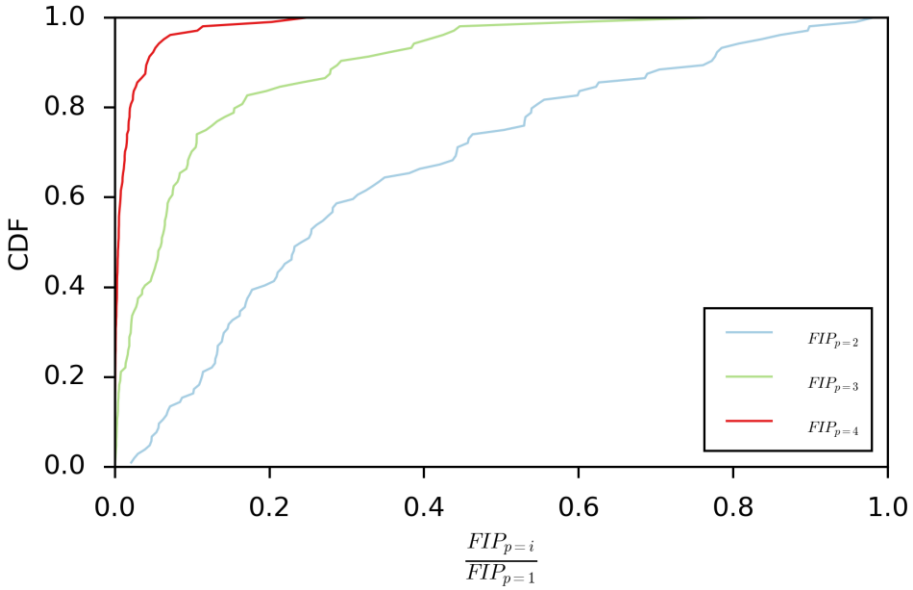

Figure 81. Slip plane ratios for three microstructures under $\varepsilon_a = 0.8\%$ and $R_\varepsilon = -1$ tension/compression.

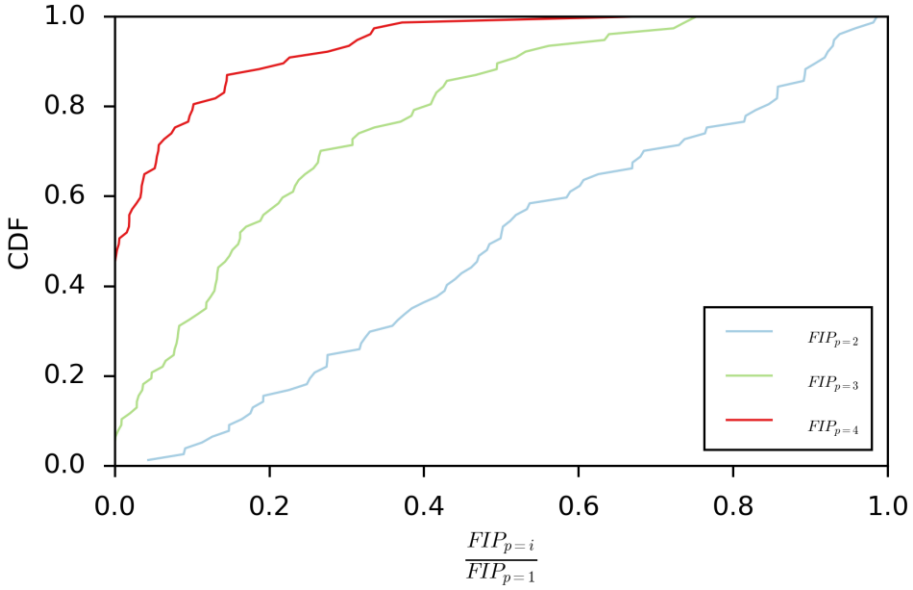

Figure 82. Slip plane ratios for three microstructures under $\gamma_a = 0.4\%$ and $R_\varepsilon = -1$ simple shear.

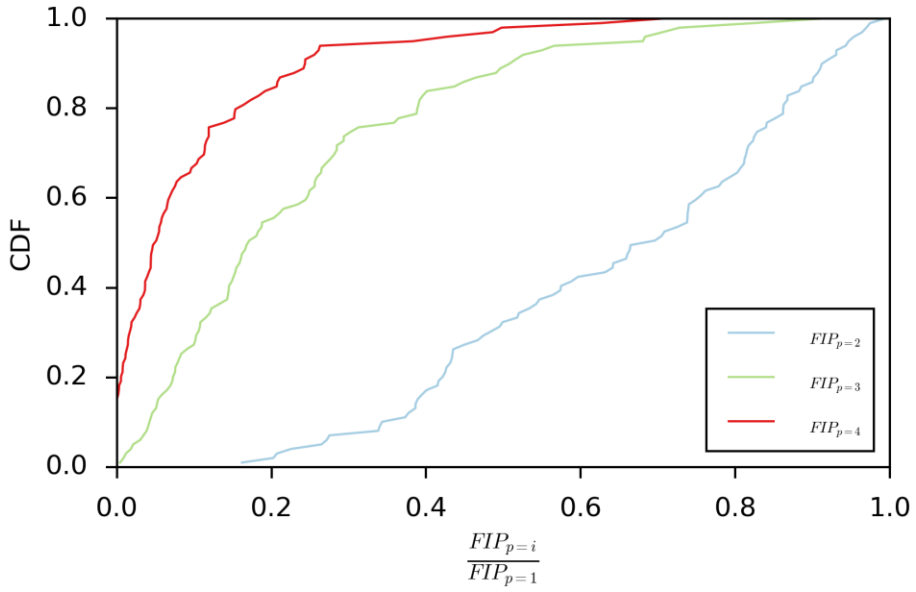

Figure 83. Slip plane ratios for three microstructures under $\gamma_a = 0.6\%$ and $R_\varepsilon = -1$ simple shear.

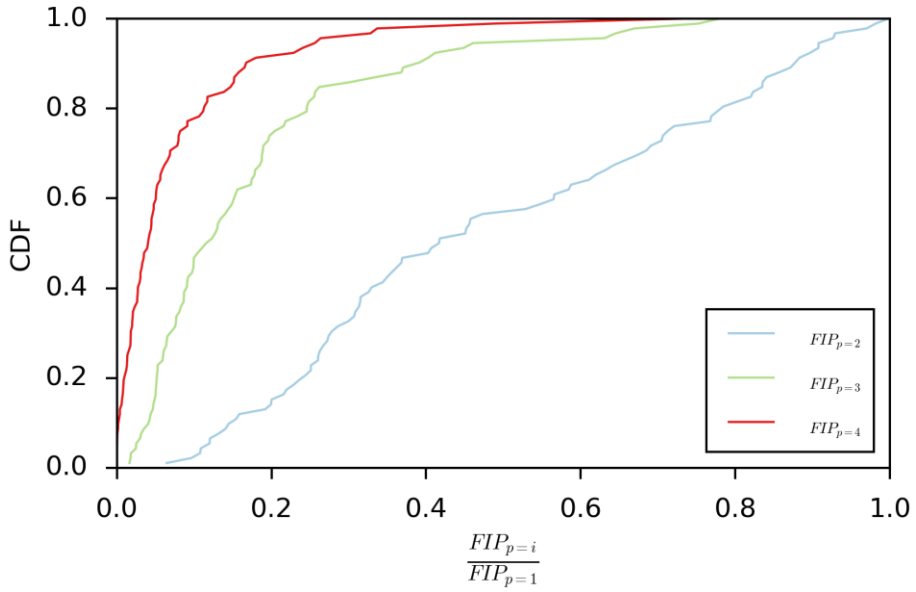

Figure 84. Slip plane ratios for three microstructures under $\gamma_a = 0.8\%$ and $R_\varepsilon = -1$ simple shear.

Neither the shear nor uniaxial loading condition demonstrates a consistent pattern for the shift in slip plane FIP ratios with increasing strain. The uniaxial propagation slip

system ratio, however, demonstrates a clear trend of decreasing FIP ratios with increasing applied load. This is consistent with previous results explored by Hennessey using the mesoscale crack propagation algorithm. This observation indicates that propagation more similar to Stage I (single dominant slip system) is occurring with higher imposed loads, which is counterintuitive and may indicate a need for further material model recalibration focused on multiple slip system activation and the effects on crack propagation.

In addition to the quantification of FIP ratios, a qualitative assessment of the choice of slip systems to average may also be considered. Both Musinski and Hennessey have selected the two highest FIP slip systems which occur on different planes to average the crack growth. As demonstrated previously, however, there is a non-negligible activation of the third slip plane which could shift the selected crack path. This is investigated by applying the crack propagation method to a static FIP field (not considering damaged elements, and thus stress redistribution) and observing the constructed crack path. Crack propagation was reevaluated in several microstructures with Figure 85 and Figure 86 being representative samples of the crack propagation variations.

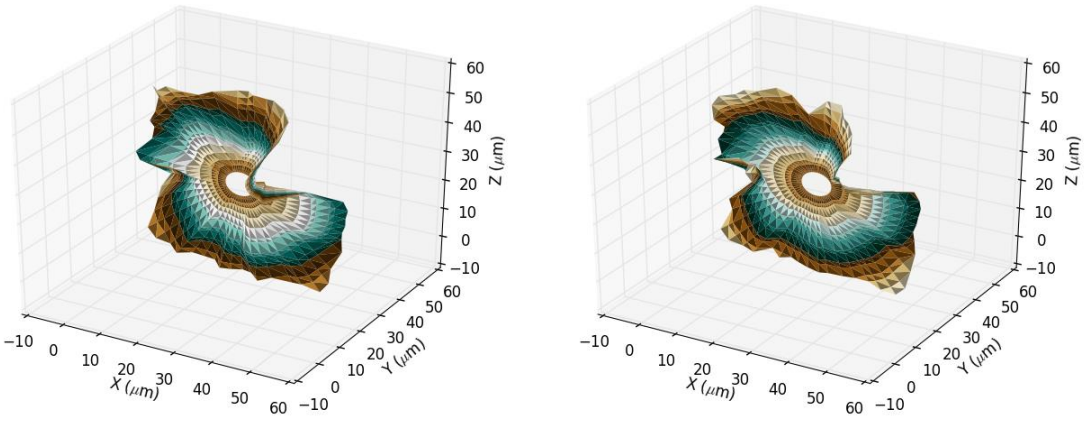

Figure 85. Crack propagation comparison using two (left) and four (right) active slip planes under $\boldsymbol{\varepsilon_a = 0.4\%}$ and $\boldsymbol{R_\varepsilon = -1}$ tension/compression in the y-axis.

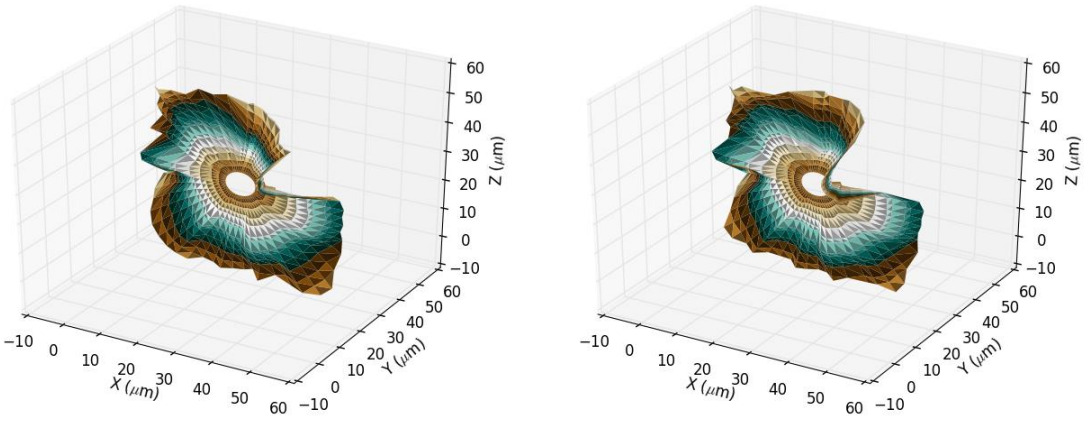

Figure 86. Crack propagation comparison using two maximally active slip systems (left) and two maximally active slip planes (right) under $\varepsilon_a = 0.4\%$ and $R_\varepsilon = -1$ tension/compression in the y-axis.

It is evident that the crack propagation remains relatively constant across the conditions studied. The substitution for total slip plane FIPs for the slip system FIPs produces an entirely negligible change in the crack propagation. Likewise, the use of the additional slip systems appears to produce a slightly more planar crack, though the effect is overall minimal. It is unclear at this point as well, whether the inclusion of additional slip systems is realistic or not. Such conclusions would likely require additional experimental data consisting of crack surface measurements and local crystallographic orientation for comparison with simulated results.

6.6: Multiaxial Fatigue: Gamma Plane Case Study

Substantial value is added by microstructure-sensitive computational fatigue approaches such as that developed here in terms of predicting the effects of combined stress state in fatigue over the full range of conceivable stress states. This is obviously intractable to pursue with physical experiments, which instead serve to validate regions of predicted behavior (e.g. uniaxial, shear, biaxial).

The Gamma Plane (Γ-plane) is a construct of Miller and Brown [34] that describes iso-life contours for general multiaxial surface strain states of the form

$$\frac{\varepsilon_1 - \varepsilon_3}{2} = f\left(\frac{\varepsilon_1 + \varepsilon_3}{2}\right) \tag{65}$$

where ordered principal strains $\varepsilon_1 \geq \varepsilon_2 \geq \varepsilon_3$ are used to describe macroscopic strain (i.e., polycrystalline aggregate) response. The bounds of the wedge depend on the Poisson ratio at a given loading, thus for the purposes of presenting a comparative, non-distorted Γ-plane, the ordered principal plastic strains $\varepsilon_1^p \geq \varepsilon_2^p \geq \varepsilon_3^p$ will be used. For the construction of the Γ-plane, the biaxial loadings are divided into two cases, those for which the maximum cyclic plastic shear strain range involves planes that extrude and intrude relative to the free surface (Case B), considered by Brown and Miller to drive cracks into the bulk, and those for which the maximum plastic shear strain range is parallel to the surface of the volume (Case A).

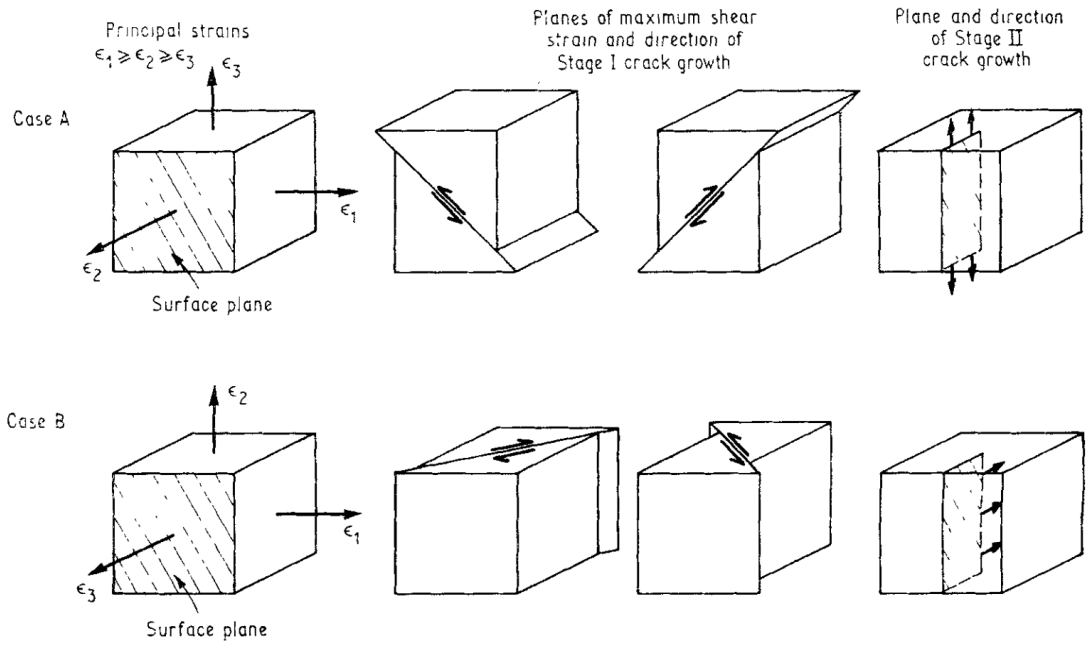

Figure 87. Planes of maximum shear and crack growth directions from bulk strains [34].

For the initial construction of a Γ-plane, the mesoscale algorithm constructed and calibrated by Hennessey is used. Since this approach is only tractable to approximately 100 μm, the definition of specimen life will be the number of cycles required to reach a

crack length of 60 μm. This is consistent with the fatigue lives presented by Hennessey [48] and with the knowledge that MSC consumes a large portion of the fatigue life for this material [120]. In the case of macroscopic failure, a definition of failure to specimen in two pieces or, for strain controlled cases, a specific reduction in stiffness may be used to define failure [137].

Since the parameter of interest, fatigue lives, is not analytically formulated, an integration for iso-life contours cannot be directly constructed. Instead, discretely sampled points must be relied upon to construct the underlying response surface, from which the iso-life contours may be extracted. The methodology for extracting the response surface is consistent with the SVE simulations strategies discussed earlier in this work. In addition to the non-representative nature of the volumes for fatigue, it is desirable to further reduce computational time expended for reconstructing the entire surface. This requires both a reduced simulation volume and mesh density and ultimately introduces variation in the plastic strain (response coordinate) and crack growth (response value) for the same applied nominal strain.

It would be beneficial if one of these uncertainties could be eliminated for the purposes of response surface construction. An assumption was made that the plastic strains would vary significantly less than the inherent variability of fatigue. Since these relative uncertainties are not known a priori, the assumption was verified upon the conclusion of the simulation DOE. Indeed, over the load amplitudes studied, the principal plastic strain values have a mean coefficient of variation of 4% and a maximum coefficient of variation of 15% for any nominal applied load. The simplification in the form of scatter in the data allows for the use of a powerful interpolation package in the form of the Scikit-learn [138] Gaussian Process Regression (GPR) package. GPR is variously referred to as Kriging in other works. This method has the benefit of explicitly capturing uncertainty in the sampled space using “nuggets” with the following formulation.

$$\text{nugget}_i = \left[\frac{\sigma_i}{y_i}\right]^2 \tag{66}$$

where σ_i is the standard deviation of the i^{th} average response, y_i.

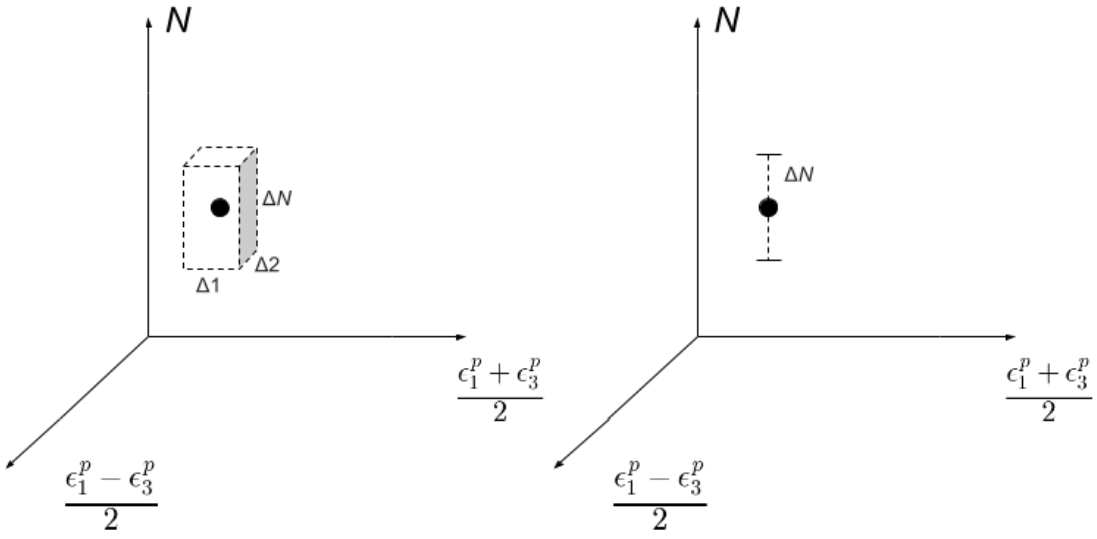

Figure 88. Comparison of true variability and condensed variability for the construction of a fatigue response surface.

Each shear direction (Case-A or Case-B) is simulated at multiple points by varying the biaxial load ratio and the load intensity. Each sample point consists of the same three microstructure instantiations to capture some of the variability inherent in fatigue. A response surface is then fit to each of the Case A and Case B conditions and each response surface is used to plot constant endurance contours. Both contours are then combined into a single plot. The response surface methodology used is known as Kriging or Gaussian Process Regression and is fit using the average of the simulated endurance for each sampled load condition. The Scikit-learn package [139] was used to incorporate uncertainty into the response surface and not strictly conform to the average response recorded. A further description of the algorithms used and their performance may be found online and in the cited paper [139, 140].

Load conditions for these conditions were applied to the RD-TD plane, with the remaining faces allowed to deform freely. Calculation of the Γ-plane was conducted with simulations of SVE size 40 μm and mesh size of 5 μm. Such a volume is justified in the work of Hennessey [48], and additional verification by the author. Reduction of computational time is particularly desirable due to the multitude of load conditions required to construct a realistic response surface. This particular construction required 450 simulations to sample the relatively limited range desired. This task is not tractable if each simulation requires hundreds of CPU-hours, but becomes feasible when each simulation requires the ~5 CPU-hours of the reduced fidelity mesh.

Several interesting features may be observed from the constructed plot. Even at the small simulated volumes studied and with a crack propagation algorithm calibrated to limited macroscopic fatigue data, the differences in loading effects between Case A and Case B loading are apparent. In addition, the shape of the iso-life contours are not constant at varying levels of plastic deformation, nor is the shape that of equal endurance independent of biaxiality ratio. Both features demonstrate the importance of a calibrated crystal plasticity model to capturing the varied loading and their impacts on fatigue indicator parameters used in the mesoscale model. It is especially interesting to note that the Case B contours have the opposite curvature when compared to those predicted by McDowll and Berard [32] using an integration of the macroscopic FS FIP. This is likely due to the implementation of discrete nucleation and propagation portions of the mesoscale fatigue model. The Case A contours are within the predicted shape and relative position when compared to the McDowell and Berard integrations.

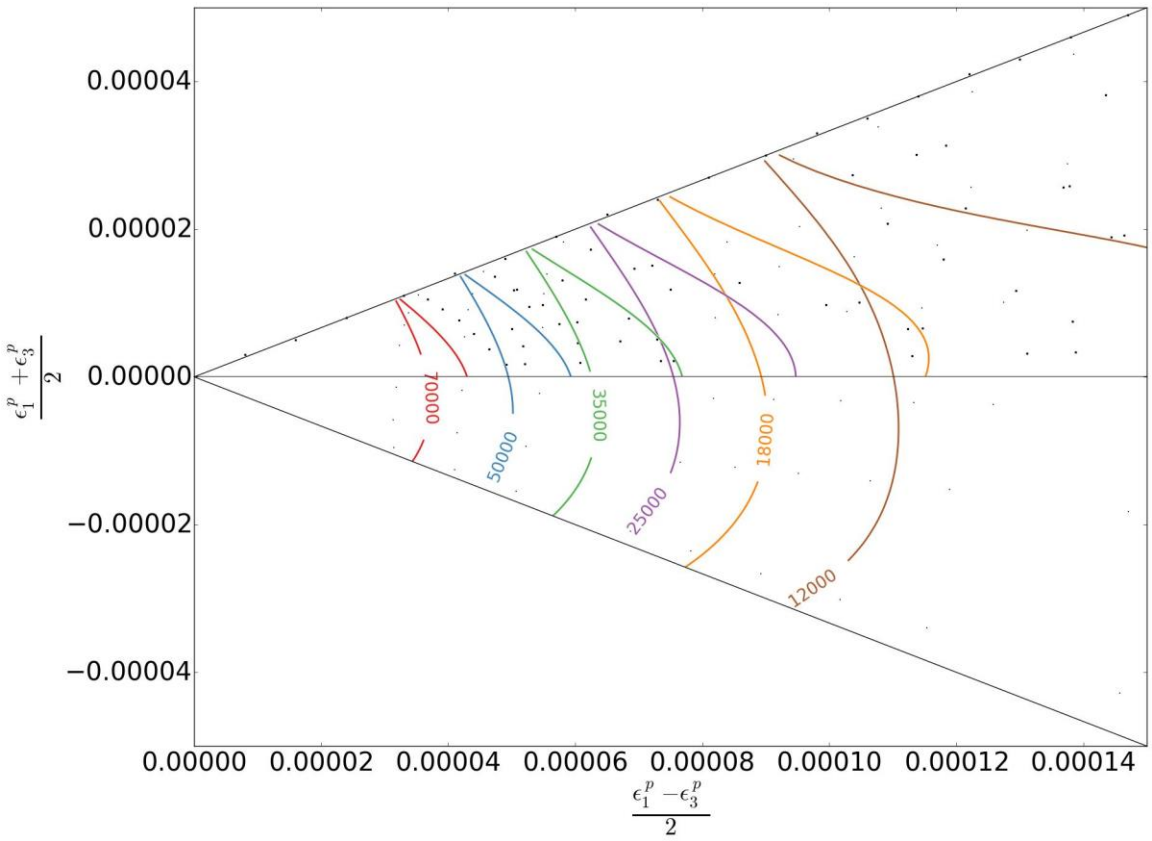

Figure 89. Γ-plane for 7075-T6 Al depicting iso-life contours based on response surface fitting to previously calibrated model. Squares are sampled loadings for Case A, points are the sampled loadings for the Case B. The unlabeled portion of the same color contour is the Case A branch.

While performing additional simulations to resolve the upper right corner of the response surface it was observed that the chosen SVE size (40 μm) is no longer a good approximation of an RVE when examining the bulk plastic strain response. Variations of the plastic strain ranges $\frac{\varepsilon_1^p - \varepsilon_3^p}{2}$ and $\frac{\varepsilon_1^p + \varepsilon_3^p}{2}$ from multiple SVEs as compared to a single SVE prediction of these responses begin to vary greater than 10%. Later creation of Γ-planes from recalibrated models should account for this by utilizing a larger simulated volume (RVE of average plastic strain) at higher applied loadings.

A necessary feature of the current construction of Γ-planes has been the imposition of continuity of the life contours from Case A to Case B. Since GPR is only

intended to interpolate response values, the upper boundary between Case A and Case B contains additional uncertainty since no sample points lie exactly on this boundary. In order to rectify this, the response surface for Case A is fed the predicted life values on the upper boundary from the Case B surface (found to have less uncertainty along this boundary). These points are visible as small boxes on the upper boundary in Figure 89. In addition, to ensure the coincidence of contours, $\text{nugget}_i = 0$ for each of these predicted points. This restricts the interpolation function of Case A to pass exactly through the mean life prediction from the Case B response surface at these points.

An additional observation on the construction of the Γ-planes involves the limitations of the linear nature of the construct. Since the bounding wedge is dependent upon the Poisson Ratio and the axes reflect the plastic strain values, a linear scale is desired to maintain a logical shape for interpreting the biaxial loading ratios. This conflicts with a potential desire to observe the variation in multiaxial fatigue lives at vastly different strain ranges. To preserve the linear nature of Figure 89 and other Γ-planes it is advised that if a large range of imposed strains is to be studied, that multiple planes are constructed and used to view the different ranges of fatigue lives.

Following the successful application of the Γ-plane construct to the previously calibrated, mesoscale fatigue algorithm, an application of the calibrated nucleation and perimeter propagation fatigue algorithm presented in this work is also reproduced. Given the success of the previous representative fatigue simulations, similar parameter selection was utilized with the reduced volumes for the newer propagation method justified in the previous sections. Propagation volumes of 55 μm sidelength with 11 elements per side were selected and reduced nucleation mesh of 10x20x10 elements and a volume of 10x20x10 μm were used. To couple the two simulations necessary to express the fatigue life, the subsampling method was applied to the propagation microstructure and the cracked particle inserted in the center of the volume. While the pipeline has the capability to support particle orientation variation and crack inclination, for the purposes of this

exploration, a constant particle orientation in the RD and crack plane normal to the RD are used.

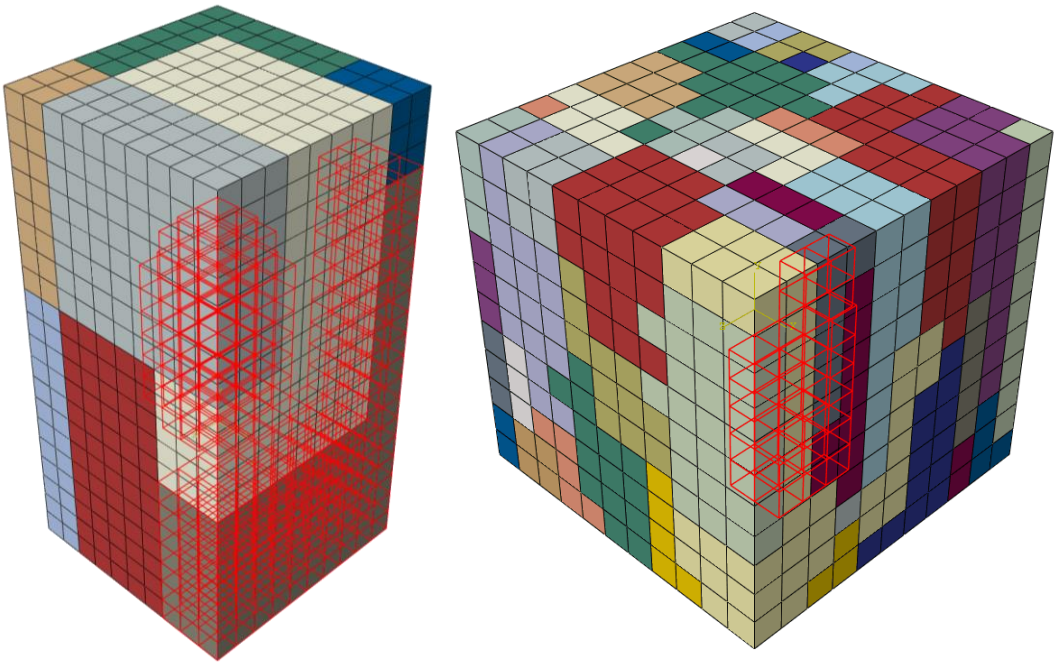

Figure 90. Nucleation mesh (left) constructed by subsampling the propagation microstructure (right) and inserting a cracked particle. Grain 50 is highlighted in both meshes along with the particle in the nucleation mesh.

Again, a constant set of microstructures (four) was selected to represent some of the inherent fatigue variability. Loading conditions were once again confined to a region $\varepsilon_a \in [0.3\%, 0.5\%]$ and ratios of principal surface strains $\boldsymbol{\xi} \in [-1,1]$ to construct the response surface. This second Γ-plane has demonstrably different behavior than the first. Most especially it is noted that the $\boldsymbol{\xi} = -1$ (x-axis, Case A) have shifted significantly to the right. This is entirely expected due to the new calibration and improved predictive capabilities in shear loading. Additionally, the new calibration shifted the Case B contours to the right for the longer life contours. This reflects the change from being a relatively conservative life prediction in VHCF to one more reflective of the experimental scatter.

The distortions in the Case B contours may have several causes. Because the explicit particles used to predict nucleation are coarsely represented in the voxelated mesh, crack mouth displacements may not be accurately captured, resulting in the oscillating contours. In addition, the relatively coarse sampling of the Γ-plane space may lead to fluctuations in the sampled function, although fitting parameters were selected to minimize this. Overall, the Γ-plane reflects the predictive capabilities of the model to describe fatigue responses in a repeatable manner across a wide variety of loading conditions infeasible for experimental observations. This Γ-plane also reflects the more accurate description of the material system, as explained previously. Crystallographic texture can contribute significantly to fatigue lives and is a potential factor in explaining the difference in observed response surface shape. The anisotropy of any FIP response would directly contribute to a change of shape in the iso-life contours.

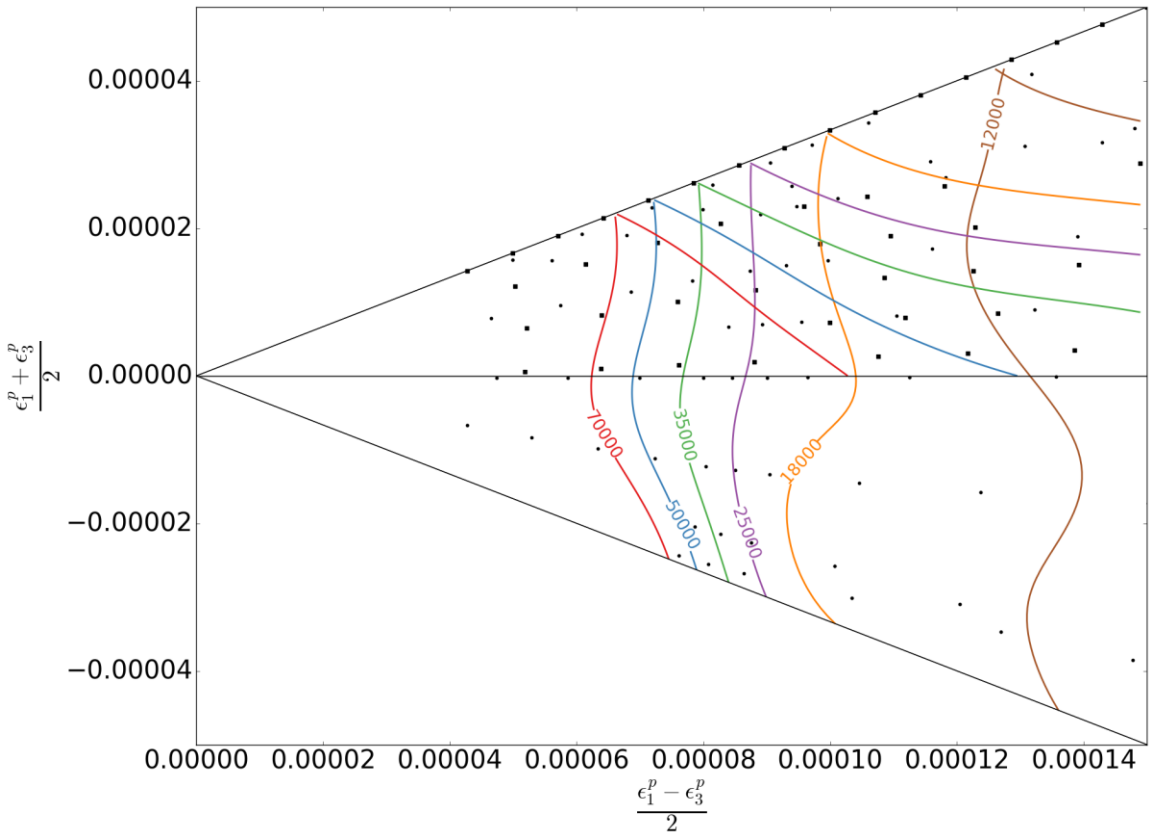

Figure 91. Γ-plane for 7075-T6 Al depicting iso-life contours based on response surface fitting to currently calibrated model. Squares are sampled loadings for Case A, points are the sampled loadings for the Case B. The unlabeled portion of the same color contour is the Case A branch.

6.7: Conclusions

In this chapter, multiple improvements to the calibration of Al 7075-T6 fatigue model were demonstrated. Particle stringers were investigated, and eventually dismissed, as a primary cause of the discrepancy in shear fatigue lives. Calibration of the fatigue model was performed with the new propagation method and more realistic synthetic microstructures. Sensitivities to various simulation parameters were investigated for this new model. While the nucleation model was determined to be highly sensitive to mesh refinement, the propagation method is found to be relatively insensitive to mesh refinement and selection of mesoscopic propagation distance over the ranges

investigated. Stage II FIP ratios were also studied in the context of the newer propagation approach. Results are not as drastic as those observed by Hennessey, but the anticipated trend of increasing FIP ratios under increased load was not observed for the range of loads studied. Finally, the new nucleation and propagation approaches were used to construct a Γ-plane and compare to the Γ-plane constructed from the calibrated mesoscale fatigue model of Hennessey. The two surfaces indicate significantly differently multiaxial fatigue responses for the same material, highlighting the importance of the selection of fatigue modeling approaches. Both of these surfaces may be useful in predicting Al 7075-T6 fatigue responses for loading conditions not reported in the literature.

CHAPTER 7: CONCLUSIONS AND DIRECTIONS FOR FUTURE RESEARCH

7.1: Summary

This work presents the results of the application of a newly developed automated simulation pipeline for crystal plasticity models to several different problems in fatigue. A scripting environment with support for many common features in crystal plasticity simulations was introduced with the intent of reducing the time and effort required by individuals to specialize code to particular problems. The automation framework was presented to utilize many of these individual functions to prepare, simulate, and analyze large quantities of crystal plasticity simulations for the purposes of fatigue analysis. The framework of the pipeline and scripting environment were provided to encourage future researchers to contribute to the consistent application and development of standards for crystal plasticity simulations.

This pipeline was used to simulate and evaluate the sensitivities of the extreme value distribution framework for comparing fatigue resistance as a function of simulation parameters. Since the extreme FIPs from individual SVE instantiations consistently converge to Gumbel distributions, responses were evaluated in the form of the Gumbel distribution parameters. Traditionally, averaging methods have been used to reduce mesh sensitivity and provide a more realistic interpretation of extreme values arising in fatigue, so values were averaged for individual grains, grain equivalent volumes, and cubic volumes. The current method SVE maximum construction of extreme value distributions was demonstrated to be highly sensitive to the simulation parameters selected, regardless of the averaging scheme chosen. Traditional statistical methods were found to be unable to compensate for the differences in Gumbel parameters for meshes ranging in size from

12^3 to 49^3. These observations were consistent across two materials (Ti64 and IN100) as well as two load amplitudes relative to the yield strain ($\varepsilon_a = 0.35\varepsilon_y$ and $\varepsilon_a = 0.7\varepsilon_y$).

To investigate the cause of these statistical anomalies, the underlying distribution of FIPs was studied for simulations of reduced integration elements (C3D8R). While the KS test rejected the notion that FIP distributions for the same material and load condition (different mesh configurations) were randomly sampled from the same distribution at a 99% confidence level, the nominal behavior of the FIPs including the FIP tails is remarkably similar. Further quantification of the behavior of the tails of FIPs discovered that for the load conditions (fully reversed shear and tension/compression) and materials (Al 7075-T6, IN100, and Ti64) considered, the tail behavior was adequately described by the three-parameter Gamma distribution. Since the Gamma distribution falls within the domain of attraction for the Gumbel distribution, this explains earlier observations about the convergence of the SVE extreme values converging to a Gumbel distribution. While FIP values from a single integration point are well behaved, averaging schemes significantly change the observed distribution of FIPs. These changes are not consistent across all simulation parameters and invalidate several statistical assumptions relating to the independently drawn samples from an underlying distribution.

A new method was proposed to characterize and compare fatigue resistance in standardized way. Monte Carlo samplings of the FIP experimental CDFs and Gamma distribution tails were performed to construct Gumbel distributions. The distribution parameters exhibited no significant correlation to SVE parameter selection. Characterizing the tails in a consistent manner allowed for extrapolation of FIP distributions at higher return periods, as well as a reduction in data dimensionality. This reduction in dimensionality coupled with characterization of FIP behavior has potential implications for future material design methods.

In addition, the automated simulation pipeline was utilized to investigate fatigue crack formation and growth in the Al 7075-T6 material system. A parameter based on the

total accumulated slip averaged over the crack mouth of the nucleant particle was demonstrated to explain the differences in fatigue lives for samples experiencing uniaxial loadings compared to shear loadings. This nucleation parameter was also found to provide a potential explanatory mechanism for the effect of mean strain on the fatigue lives of Al 7075-T6. Stage II crack propagation was reevaluated following the development of a new propagation method. Geometrical considerations were highlighted in the development of this model to improve fundamental adherence to material behavior and increase model fidelity by removing ambiguity in the determination of the intermediate crack propagation plane. This crack propagation method was found to be relatively insensitive for mesh refinement for comparisons of total crack length. This result was anticipated following the analysis that the volumetric FIP distribution was found to be relatively mesh insensitive and the FS FIP is used as a surrogate measure for the crack propagation rate.

The new fatigue model was coupled with improved reconstruction morphology and crystallographic texture and calibrated to more accurately match experimental specimens of Al 7075-T6. Multiaxial fatigue simulations were conducted to construct Γ-Plane sections for a previous fatigue crack growth model, and the newly introduced model with the explicit consideration of crack nucleation at particles and a point propagation model for fatigue crack growth. It was demonstrated that significant differences in fatigue life estimation of the multiaxial response surface arise based on the differences in model form, even when calibrated to the same data. These fatigue model forms may lead to significant differences in design conclusions drawn from newly predicted loading conditions.

7.2: Directions for Future Research

It is desired that the most important contribution of this work is the transparency of the data and tools utilized within. With the development of the automated material

simulation pipeline, verification and improvements to the methodology presented in the work may occur at a more rapid pace. With this normal obstacle of research reduced, contributions to the pipeline should improve data generation and analysis rates within the material simulation community. Significant work can still be performed to expand the functionality of the pipeline, especially when considering different microstructure instantiation tools such as 2-point statistics optimization routines and other, more specialized, software. Additionally, improvements to the meshing capabilities such as the ability to produce smooth grain boundary meshes will allow free meshing routines to construct meshes that more efficiently capture complex morphologies such as smaller particles embedded in a coarser grain matrix. A final desired improvement is the incorporation of more flexible post-processing methods to handle data from simulations utilizing linear or quadratic elements.

The data generated from these simulations should also be discussed to provide a standard means of storing useful information, which may be shared between individual researchers and organizations. Small, local databases as well as large, remote databases may be useful to address scaling beyond the current organized folder structure that, while simple to visualize and interact with via file manager applications, can provide complications with traceability and significantly reduce access time and portability of data. Standardized schema can be developed internally and externally using SQL databases. With data stored in a standardized, flexible format, a greater degree of automation can be achieved utilizing these datasets. This organization should also be extended to software developed as well. Sufficient safeguards must be developed to ensure that insufficient knowledge of crystal plasticity simulations does not lead to incorrect data generation.

While FIP distributions were observed for a variety of loading conditions, crystal plasticity models, and textures, further research into the general applicability of the Gamma distribution tail characterization is desirable. Statistical and physical

investigation into the introduction of biases caused by sampling and ensemble of SVE instead of a single RVE would be of great value to quantifying the uncertainty for the total FIP distribution. Previously developed marked correlation functions or higher order spatial statistics and principal component analysis could be applied to understand the characteristics that shift the constructed FIP distributions. Quantifying uncertainty associated with sampling the FIP distribution may be utilized in scenarios requiring robust designs. These studies can help to reduce the computational effort required to simulate vast regions of feasible microstructures as well as standardize the data necessary to facilitate the construction of databases of explored material designs.

Implementation of improved nucleation and propagation models in Python scripts that are decoupled from the UMAT should facilitate more rapid adoption of crack propagation simulations and more rapid study of crack driving forces across various material models. These scripts can be further generalized to study Stage II propagation at a more fundamental level in simulated microstructures. Additional simulations should be performed to study the effect of stress redistribution during crack advance, grain boundary slip transfer and various flow rules and internal state variable evolution models. Comparing these results with existing and newly acquired experimental data could provide significant additional insight into the processes of microstructurally small crack growth.

As has been alluded to numerous times throughout this thesis, the improvements made to crystal plasticity fatigue simulations by this work have potential applications in material design processes. In addition to the work presented in this thesis, significant progress has been made to provide an open source implementation of the Inductive Design Exploration Method (IDEM) [141] which will enable the more rapid application of robust design principles to materials development. This framework provides the ability to address design challenges commonly occurring in materials design while incorpating Type 1, Type 2, and Type 3 model uncertainty. The incorporation of the automated

material simulation pipeline, improved crack propagation method, and Al 7075-T6 nucleation simulations could provide future avenues for materials design projects associated with this material system, however future work must also address and quantify the sources of uncertainty at each stage of simulation.

APPENDIX A

Reference File Formats

Several file types are read and written by many different parts of the automated material simulation pipeline as well as miscellaneous scripts and applications used across the McDowell group. While the author has attempted to consolidate these interfaces into cross-functional modules, redundant code will always exist. The following contains a documentation of the various file types and data formats used by the new modules and several legacy codes. Files with a numeric link to a specific instantiation will be denoted using the number sign #. During execution of simulations, some of these files may have the identifying number stripped and later appended to retain compatibility during simulation, but reintroduce traceability upon completion. Formatting for each line will use Python print formatting to be explicit.

- Common_block_Alv02.txt
    - Linked by compiler for UMAT and UEXTERNALDB of Al 7075-T6
    - Fortran variable declarations and allocations
- CRACK_ARRESTED_#.txt
    - Read by UEXETERNALDB of Al 7075-T6 to indicate completion of crack propagation as signaled by Python
    - Empty text file
- cracked_elem_#.txt
    - Written by Python crack propagation or meshing.py to determine current cracked elements and planes
    - Space separated file of format “%d %f %f %f” of element number, x, y, and z respectively to define crack plane for damaged elements
- CrackGrowth_py_#.txt
    - Written by Python crack propagation and read by post_process.py
    - Space separated file of format “%f %f” for cycles and length respectively

- d_gr_nd_#.txt
    - Contributions to band length from low misorientation neighbors
    - Deprecated
- Definitions.txt
    - Written by simulation.py and linked by compiler for UEXTERNALDB of Al 7075-T6
    - Defines all fatigue and material constants for UEXTERNALDB
    - eval_life_array() – loading steps at which crack extension will be evaluated and cracked elements updated prior to the application of load
- El_pos_#.txt
    - Written by meshing.py and read by various scripts
    - Space separated file of format "Elem%d %f %f %f" for element number, x, y, z coordinates of the centroid of the element
- Element_Volume_#.txt
    - Written by meshing.py
    - "%f" element volume in mm^3 for each element
- FIP_MSC#_el_#.txt
    - Written by UEXTERNALDB and read by Python crack propagation
    - Space separated file of format "%d %d %d %f" for element number, slip system number, grain number, and FS-FIP
- FIP_Nuc_el_#.txt
    - Written by UEXTERNALDB and read by Python crack propagation
    - Space separated file of format "%d %d %d %f %d " for element number, slip system number, grain number, FS-FIP, and number of elements in the band
- Geom_Def_#.txt
    - Written by meshing.py and linked by compiler for UEXTERNALDB of Al 7075-T6
    - Defines a number of geometry related values such as number of elements
- Grains_#.txt
    - Written by meshing.py and read by various scripts

    - Comma separated file of format "%f, %f, %f" for grain volume, ϕ_1, Φ, and ϕ_2 as defined by Bunge-Euler angles in radians
- Neighbors_el_#.txt
    - Written by meshing.py and read by various scripts
    - Comma separated file of format "%d, %d, …, %d"
    - Each row contains the numbers of the neighboring elements with 0 indicating no neighbor
    - Considers all elements sharing a single vertex or more
- trial_elem_grains_#.txt
    - Written and read by microstructure.py
    - First line is ex,ey,ez(,x,y,z) – parentheses optional
    - Second line is of format "%d,%d,%d(,%f,%f,%f)" for number of x, y, and z elements and optionally the x, y, and z geometry size
    - Following lines are the grain number $\in [1, n]$ for each element in Fortran numbering order (meaning flattened list with 3D indices increasing fastest in the first index)
- trial_EulerAngles_#.txt
    - Written and read by microstructure.py
    - First line is number of grains
    - Two lines of headers
    - Space separated file of format "%d %f %f %f" for grain number starting at 1, ϕ_1, Φ, and ϕ_2 as defined by Bunge-Euler angles in degrees
- trial_Phases_#.txt
    - Written and read by microstructure.py
    - First line is "Grain Phase"
    - Following lines are grain phase integers $\in [1, n]$

APPENDIX B

Table 7. Ti64 responses for nine configurations at $\varepsilon_a = 0.35\varepsilon_y$.

Config.	c_σ	$\mu_{element}$	$\sigma_{element}$	$c_{\mu_{element}}$	$c_{\sigma_{element}}$	μ_{grain}	σ_{grain}	$c_{\mu_{grain}}$	$c_{\sigma_{grain}}$
1	2.53E-02	1.09E-15	7.44E-16	1.62E-01	1.60E-01	1.74E-16	1.35E-16	1.85E-01	1.54E-01
2	2.49E-02	1.65E-15	1.19E-15	1.72E-01	1.58E-01	1.71E-16	1.04E-16	1.45E-01	1.63E-01
3	2.44E-02	2.73E-15	2.35E-15	2.06E-01	1.45E-01	3.23E-16	3.42E-16	2.53E-01	1.48E-01
4	2.09E-02	3.15E-15	2.75E-15	2.08E-01	1.53E-01	6.56E-16	9.73E-16	3.55E-01	1.38E-01
5	2.07E-02	4.33E-15	3.45E-15	1.90E-01	1.56E-01	3.38E-16	3.04E-16	2.14E-01	1.42E-01
6	2.07E-02	8.39E-15	7.06E-15	2.01E-01	1.49E-01	3.45E-16	2.62E-16	1.81E-01	1.48E-01
7	2.06E-02	3.67E-15	2.37E-15	1.54E-01	1.56E-01	4.21E-16	3.73E-16	2.12E-01	1.46E-01
8	2.07E-02	4.21E-15	2.17E-15	1.23E-01	1.58E-01	3.60E-16	2.86E-16	1.90E-01	1.49E-01
9	2.07E-02	1.27E-14	9.77E-15	1.83E-01	1.49E-01	4.25E-16	3.99E-16	2.24E-01	1.43E-01

Table 8. Ti64 responses for nine configurations at $\varepsilon_a = 0.35\varepsilon_y$ cont.

Config.	μ_{cube}	σ_{cube}	$c_{\mu_{cube}}$	$c_{\sigma_{cube}}$	μ_{kernel}	σ_{kernel}	$c_{\mu_{kernel}}$	$c_{\sigma_{kernel}}$
1	3.30E-16	2.54E-16	1.84E-01	1.56E-01	1.35E-16	1.08E-16	1.90E-01	1.53E-01
2	5.14E-16	3.92E-16	1.82E-01	1.57E-01	1.29E-16	9.49E-17	1.76E-01	1.58E-01
3	9.15E-16	9.29E-16	2.43E-01	1.41E-01	1.26E-16	1.19E-16	2.25E-01	1.41E-01
4	8.34E-16	8.55E-16	2.45E-01	1.45E-01	3.49E-16	3.39E-16	2.32E-01	1.47E-01
5	9.80E-16	7.01E-16	1.71E-01	1.54E-01	2.51E-16	1.59E-16	1.51E-01	1.62E-01
6	2.20E-15	1.74E-15	1.89E-01	1.52E-01	2.32E-16	1.77E-16	1.82E-01	1.46E-01
7	1.06E-15	7.39E-16	1.66E-01	1.56E-01	4.49E-16	2.99E-16	1.59E-01	1.61E-01
8	1.27E-15	7.48E-16	1.40E-01	1.58E-01	3.57E-16	2.30E-16	1.54E-01	1.56E-01
9	3.50E-15	2.27E-15	1.54E-01	1.56E-01	4.61E-16	2.88E-16	1.49E-01	1.62E-01

Table 9. Ti64 responses for nine configurations at $\varepsilon_a = 0.7\varepsilon_y$.

Config.	c_σ	$\mu_{element}$	$\sigma_{element}$	$c_{\mu_{element}}$	$c_{\sigma_{element}}$	μ_{grain}	σ_{grain}	$c_{\mu_{grain}}$	$c_{\sigma_{grain}}$
1	4.41E-02	2.52E-06	1.56E-06	1.48E-01	1.60E-01	8.41E-07	6.23E-07	1.77E-01	1.46E-01
2	3.80E-02	2.83E-06	1.46E-06	1.23E-01	1.58E-01	8.31E-07	6.36E-07	1.83E-01	1.39E-01
3	3.77E-02	3.82E-06	1.74E-06	1.08E-01	1.67E-01	7.68E-07	4.10E-07	1.27E-01	1.49E-01
4	3.24E-02	3.92E-06	1.50E-06	9.08E-02	1.66E-01	1.18E-06	7.52E-07	1.52E-01	1.48E-01
5	2.95E-02	6.21E-06	3.01E-06	1.16E-01	1.47E-01	1.74E-06	1.49E-06	2.04E-01	1.40E-01
6	2.98E-02	7.20E-05	1.12E-04	3.71E-01	1.40E-01	1.36E-06	8.39E-07	1.47E-01	1.46E-01
7	2.06E-02	5.83E-06	1.89E-06	7.73E-02	1.60E-01	1.02E-06	3.48E-07	8.09E-02	1.56E-01
8	2.07E-02	6.30E-06	1.73E-06	6.52E-02	1.63E-01	9.12E-07	2.17E-07	5.66E-02	1.68E-01
9	2.06E-02	4.14E-05	6.50E-05	3.76E-01	1.37E-01	9.59E-07	1.80E-07	4.46E-02	1.70E-01

Table 10. Ti64 responses for nine configurations at $\varepsilon_a = 0.7\varepsilon_y$ cont.

Config.	μ_{cube}	σ_{cube}	$c_{\mu_{cube}}$	$c_{\sigma_{cube}}$	μ_{kernel}	σ_{kernel}	$c_{\mu_{kernel}}$	$c_{\sigma_{kernel}}$
1	9.50E-07	5.18E-07	1.30E-01	1.66E-01	4.40E-07	2.52E-07	1.36E-01	1.62E-01
2	1.13E-06	4.79E-07	1.01E-01	1.73E-01	3.92E-07	1.78E-07	1.08E-01	1.66E-01
3	1.68E-06	8.68E-07	1.23E-01	1.67E-01	4.37E-07	2.73E-07	1.49E-01	1.53E-01
4	1.50E-06	5.97E-07	9.46E-02	1.60E-01	6.98E-07	2.51E-07	8.56E-02	1.63E-01
5	2.72E-06	1.77E-06	1.56E-01	1.44E-01	7.59E-07	3.79E-07	1.19E-01	1.51E-01
6	1.49E-05	2.12E-05	3.41E-01	1.39E-01	1.43E-06	1.58E-06	2.65E-01	1.39E-01
7	2.24E-06	6.81E-07	7.22E-02	1.61E-01	9.76E-07	3.56E-07	8.68E-02	1.55E-01
8	2.57E-06	6.55E-07	6.05E-02	1.68E-01	8.93E-07	2.42E-07	6.44E-02	1.74E-01
9	7.68E-06	7.95E-06	2.48E-01	1.38E-01	1.13E-06	5.63E-07	1.19E-01	1.46E-01

Table 11. IN100 responses for nine configurations at $\varepsilon_a = 0.35\varepsilon_y$.

Config.	c_σ	$\mu_{element}$	$\sigma_{element}$	$c_{\mu_{element}}$	$c_{\sigma_{element}}$	μ_{grain}	σ_{grain}	$c_{\mu_{grain}}$	$c_{\sigma_{grain}}$
1	6.56E-02	2.06E-08	5.90E-09	6.78E-02	1.72E-01	5.15E-09	2.21E-09	1.02E-01	1.50E-01
2	9.09E-02	2.65E-08	1.23E-08	1.11E-01	1.58E-01	5.25E-09	2.30E-09	1.04E-01	1.52E-01
3	7.55E-02	2.79E-08	9.77E-09	8.30E-02	1.77E-01	5.09E-09	1.92E-09	8.97E-02	1.68E-01
4	4.65E-02	2.63E-08	5.87E-09	5.29E-02	1.71E-01	6.88E-09	3.22E-09	1.12E-01	1.42E-01
5	1.74E-02	2.79E-08	1.31E-08	1.12E-01	1.55E-01	4.71E-09	1.58E-09	7.93E-02	1.68E-01
6	6.41E-02	2.30E-08	1.14E-08	1.18E-01	1.58E-01	3.70E-09	2.26E-09	1.46E-01	1.50E-01
7	4.12E-02	2.69E-08	1.18E-08	1.04E-01	1.59E-01	6.51E-09	2.54E-09	9.29E-02	1.63E-01
8	1.53E-02	2.48E-08	1.03E-08	9.87E-02	1.73E-01	4.43E-09	2.55E-09	1.37E-01	1.61E-01
9	4.70E-02	3.39E-08	3.37E-08	2.38E-01	1.43E-01	2.47E-09	8.11E-10	7.83E-02	1.59E-01

Table 12. IN100 responses for nine configurations at $\varepsilon_a = 0.35\varepsilon_y$ cont.

Config.	μ_{cube}	σ_{cube}	$c_{\mu_{cube}}$	$c_{\sigma_{cube}}$	μ_{kernel}	σ_{kernel}	$c_{\mu_{kernel}}$	$c_{\sigma_{kernel}}$
1	7.96E-09	3.29E-09	9.86E-02	1.50E-01	4.39E-09	1.74E-09	9.47E-02	1.50E-01
2	1.07E-08	4.34E-09	9.65E-02	1.61E-01	4.66E-09	1.37E-09	6.98E-02	1.72E-01
3	1.21E-08	4.11E-09	8.08E-02	1.77E-01	4.10E-09	1.24E-09	7.19E-02	1.78E-01
4	9.66E-09	1.94E-09	4.74E-02	1.67E-01	5.14E-09	9.14E-10	4.18E-02	1.80E-01
5	9.57E-09	2.73E-09	6.75E-02	1.73E-01	4.13E-09	1.23E-09	7.03E-02	1.72E-01
6	8.18E-09	3.31E-09	9.63E-02	1.63E-01	2.85E-09	1.36E-09	1.14E-01	1.60E-01
7	1.05E-08	5.20E-09	1.18E-01	1.49E-01	5.66E-09	2.38E-09	1.00E-01	1.55E-01
8	8.96E-09	4.20E-09	1.12E-01	1.66E-01	3.70E-09	1.82E-09	1.17E-01	1.66E-01
9	9.18E-09	6.31E-09	1.64E-01	1.49E-01	2.44E-09	1.01E-09	9.93E-02	1.52E-01

Table 13. IN100 responses for nine configurations at $\varepsilon_a = 0.7\varepsilon_y$.

Config.	c_σ	$\mu_{element}$	$\sigma_{element}$	$c_{\mu_{element}}$	$c_{\sigma_{element}}$	μ_{grain}	σ_{grain}	$c_{\mu_{grain}}$	$c_{\sigma_{grain}}$
1	6.19E-02	3.11E-03	6.17E-04	4.72E-02	1.66E-01	1.33E-03	4.99E-04	8.92E-02	1.54E-01
2	6.31E-02	3.38E-03	6.27E-04	4.51E-02	1.71E-01	1.37E-03	6.75E-04	1.20E-01	1.58E-01
3	6.18E-02	3.56E-03	7.05E-04	4.70E-02	1.59E-01	1.45E-03	5.63E-04	9.23E-02	1.62E-01
4	5.69E-02	3.31E-03	6.51E-04	4.67E-02	1.62E-01	1.45E-03	6.93E-04	1.14E-01	1.50E-01
5	3.99E-02	3.50E-03	4.58E-04	3.18E-02	1.70E-01	1.54E-03	8.13E-04	1.29E-01	1.60E-01
6	6.85E-02	3.73E-03	5.36E-04	4.61E-02	2.26E-01	1.38E-03	5.35E-04	1.25E-01	2.13E-01
7	5.58E-02	3.78E-03	6.83E-04	4.63E-02	1.94E-01	8.99E-04	2.38E-04	6.78E-02	1.99E-01
8	3.35E-02	4.54E-03	7.29E-04	4.94E-02	2.11E-01	9.97E-04	3.33E-04	1.03E-01	2.08E-01
9	6.09E-02	4.68E-03	7.75E-04	4.69E-02	1.95E-01	8.69E-04	2.30E-04	7.47E-02	2.07E-01

Table 14. IN100 responses for nine configurations at $\varepsilon_a = 0.7\varepsilon_y$ cont.

Config.	μ_{cube}	σ_{cube}	$c_{\mu_{cube}}$	$c_{\sigma_{cube}}$	μ_{kernel}	σ_{kernel}	$c_{\mu_{kernel}}$	$c_{\sigma_{kernel}}$
1	1.34E-03	5.56E-04	9.89E-02	1.48E-01	5.69E-04	1.86E-04	7.78E-02	1.60E-01
2	1.60E-03	4.70E-04	7.15E-02	1.70E-01	5.08E-04	1.57E-04	7.54E-02	1.74E-01
3	1.85E-03	5.30E-04	6.83E-02	1.58E-01	5.14E-04	1.92E-04	8.91E-02	1.56E-01
4	1.35E-03	4.59E-04	8.12E-02	1.52E-01	5.99E-04	2.13E-04	8.46E-02	1.53E-01
5	1.67E-03	3.13E-04	4.55E-02	1.88E-01	5.68E-04	1.24E-04	5.29E-02	1.82E-01
6	1.88E-03	3.48E-04	5.94E-02	2.31E-01	5.10E-04	1.04E-04	6.50E-02	2.59E-01
7	1.78E-03	4.84E-04	6.99E-02	1.80E-01	8.21E-04	2.25E-04	7.05E-02	1.88E-01
8	2.41E-03	4.64E-04	5.90E-02	2.28E-01	9.13E-04	2.66E-04	8.93E-02	2.22E-01
9	2.45E-03	5.20E-04	6.01E-02	1.91E-01	7.92E-04	1.75E-04	6.23E-02	2.21E-01

APPENDIX C

Table 15. Gamma distribution fits to 99.9% FIP tails for nine configurations of Ti64 at $\varepsilon_a = 0.35\varepsilon_y$.

Config.	α	μ_g	σ_g	R^2
1	7.09E-01	6.38E-16	7.70E-16	9.32E-01
2	7.42E-01	6.38E-16	8.98E-16	9.83E-01
3	6.04E-01	6.22E-16	1.10E-15	9.66E-01
4	6.20E-01	5.50E-16	1.20E-15	9.14E-01
5	6.11E-01	5.19E-16	1.21E-15	9.67E-01
6	7.20E-01	6.03E-16	1.12E-15	9.74E-01
7	7.13E-01	4.58E-16	8.98E-16	9.77E-01
8	7.56E-01	4.78E-16	8.11E-16	9.88E-01
9	6.32E-01	5.23E-16	1.33E-15	9.76E-01

Table 16. Gamma distribution fits to 99.9% FIP tails for nine configurations of Ti64 at $\varepsilon_a = 0.7\varepsilon_y$.

Config.	α	μ_g	σ_g	R^2
1	8.84E-01	1.57E-06	9.59E-07	9.89E-01
2	7.65E-01	1.35E-06	9.79E-07	9.94E-01
3	8.87E-01	1.48E-06	9.91E-07	9.96E-01
4	8.09E-01	1.30E-06	9.96E-07	9.97E-01
5	8.00E-01	1.55E-06	1.23E-06	9.92E-01
6	5.46E-01	1.53E-06	2.82E-06	9.20E-01
7	7.99E-01	1.42E-06	1.08E-06	9.95E-01
8	8.00E-01	1.45E-06	1.09E-06	9.97E-01
9	7.33E-01	1.50E-06	1.38E-06	9.89E-01

Table 17. Gamma distribution fits to 99.9% FIP tails for nine configurations of IN100 at $\boldsymbol{\varepsilon_a = 0.35\varepsilon_y}$.

Config.	α	μ_g	σ_g	R^2
1	8.99E-01	1.39E-08	5.21E-09	9.83E-01
2	7.69E-01	1.44E-08	7.06E-09	9.74E-01
3	8.00E-01	1.42E-08	6.14E-09	9.95E-01
4	9.17E-01	1.43E-08	4.81E-09	9.94E-01
5	8.00E-01	1.20E-08	5.69E-09	9.95E-01
6	9.23E-01	9.27E-09	3.92E-09	9.96E-01
7	8.70E-01	1.29E-08	5.44E-09	9.95E-01
8	8.00E-01	1.02E-08	4.98E-09	9.97E-01
9	8.00E-01	5.76E-09	3.66E-09	9.82E-01

Table 18. Gamma distribution fits to 99.9% FIP tails for nine configurations of IN100 at $\boldsymbol{\varepsilon_a = 0.7\varepsilon_y}$.

Config.	α	μ_g	σ_g	R^2
1	1.10E+00	2.43E-03	4.19E-04	9.87E-01
2	9.58E-01	2.50E-03	4.46E-04	9.92E-01
3	9.72E-01	2.49E-03	5.10E-04	9.94E-01
4	9.37E-01	2.20E-03	4.47E-04	9.94E-01
5	1.03E+00	2.26E-03	4.17E-04	9.98E-01
6	1.16E+00	2.21E-03	3.97E-04	9.97E-01
7	9.39E-01	2.31E-03	5.27E-04	9.95E-01
8	9.63E-01	2.43E-03	5.96E-04	9.94E-01
9	9.50E-01	2.41E-03	5.73E-04	9.96E-01

Table 19. Gamma distribution fits to 99.9% FIP tails for four textures of Ti64 at $\boldsymbol{\varepsilon_a = 0.75\varepsilon_y}$.

Texture	α	μ_g	σ_g	R^2
Basal	9.36E-01	6.21E-07	2.41E-07	9.97E-01
Transverse	8.00E-01	8.90E-07	4.27E-07	9.97E-01
Random	8.00E-01	1.13E-06	5.02E-07	9.95E-01
Actual	9.59E-01	3.08E-06	1.28E-06	9.99E-01

REFERENCES

1. Reed, R.P., J.H. Smith, and B.W. Christ, *Economic Effects of Fracture in the United States. Part 1. a Synopsis of the September 30, 1982 Report to Nbs by Battelle Columbus Laboratories (No. DOE/ER/10741-T1-Pt.1; NBS-SP-647-1)*. 1983: Washington, DC.

2. Wöhler, A., *Versuche über die Festigkeit der Eisenbahnwagenachsen.* Zeitschrift für Bauwesen, 1860. **10**: p. 160-161.

3. Basquin, O. *The exponential law of endurance tests*. in *Proc. Astm*. 1910.

4. McDowell, D.L., *Basic issues in the mechanics of high cycle fatigue.* International Journal of Fracture, 1996. **80**: p. 103-145.

5. McClung, R., et al., *Analysis of small crack behavior for airframe applications.* 1994.

6. Xue, Y., et al., *Micromechanisms of multistage fatigue crack growth in a high-strength aluminum alloy.* Acta Materialia, 2007. **55**(6): p. 1975-1984.

7. Weiland, H., et al., *Microstructural aspects of crack nucleation during cyclic loading of AA7075-T651.* Engineering Fracture Mechanics, 2009. **76**(5): p. 709-714.

8. Lankford, J., *The growth of small fatigue cracks in 7075–T6 aluminum.* Fatigue & Fracture of Engineering Materials & Structures, 1982. **5**(3): p. 233-248.

9. Payne, J., et al., *Observations of fatigue crack initiation in 7075-T651.* International Journal of Fatigue, 2010. **32**(2): p. 247-255.

10. Bozek, J., et al., *A geometric approach to modeling microstructurally small fatigue crack formation: I. Probabilistic simulation of constituent particle cracking in AA 7075-T651.* Modelling and Simulation in Materials Science and Engineering, 2008. **16**(6): p. 065007.

11. Harris, J.J., *Particle cracking damage evolution in 7075 wrought aluminum alloy under monotonic and cyclic loading conditions*, in *Materials Science and Engineering*. 2005, Georgia Institute of Technology.

12. Burns, J.T., J.M. Larsen, and R.P. Gangloff, *Effect of initiation feature on microstructure-scale fatigue crack propagation in Al–Zn–Mg–Cu.* International journal of fatigue, 2012. **42**: p. 104-121.

13. Li, P., N. Marchand, and B. Ilschner, *Crack initiation mechanisms in low cycle fatigue of aluminium alloy 7075 T6.* Materials Science and Engineering: A, 1989. **119**: p. 41-50.

14. Musinski, W.D. and D.L. McDowell, *Microstructure-sensitive probabilistic modeling of HCF crack initiation and early crack growth in Ni-base superalloy IN100 notched components.* International Journal of Fatigue, 2012. **37**: p. 41-53.

15. Miller, K., *The short crack problem.* Fatigue & Fracture of Engineering Materials & Structures, 1982. **5**(3): p. 223-232.

16. Stock, S., *Recent advances in X-ray microtomography applied to materials.* International Materials Reviews, 2008. **53**(3): p. 129-181.

17. Akiniwa, Y., K. Tanaka, and E. Matsui, *Statistical characteristics of propagation of small fatigue cracks in smooth specimens of aluminium alloy 2024-T3.* Materials Science and Engineering: A, 1988. **104**: p. 105-115.

18. McDowell, D., *Multiaxial fatigue strength.* ASM Handbook, 1996: p. 263-273.

19. Socie, D., *Critical plane approaches for multiaxial fatigue damage assessment*, in *Advances in multiaxial fatigue*. 1993, ASTM International.

20. Künkler, B., et al., *Modelling of short crack propagation–Transition from stage I to stage II.* Engineering Fracture Mechanics, 2008. **75**(3): p. 715-725.

21. Johnston, S., et al., *Three-dimensional finite element simulations of microstructurally small fatigue crack growth in 7075 aluminium*

alloy. Fatigue & Fracture of Engineering Materials & Structures, 2006. **29**(8): p. 597-605.

22. Khor, K., et al., *High resolution X-ray tomography of micromechanisms of fatigue crack closure.* Scripta materialia, 2006. **55**(1): p. 47-50.

23. Li, X., *Micromechanical model of stage I to stage II crack growth transition for aluminium alloys.* Theoretical and applied fracture mechanics, 1996. **24**(3): p. 217-231.

24. Neumann, P., *1. New experiments concerning the slip processes at propagating fatigue crack. 2. The geometry of slip processes at a propagating fatigue crack*. 1974.

25. Neumann, P., *Coarse slip model of fatigue.* Acta metallurgica, 1969. **17**(9): p. 1219-1225.

26. Stanzl-Tschegg, S. and H. Mayer, *Fatigue and fatigue crack growth of aluminium alloys at very high numbers of cycles.* International Journal of Fatigue, 2001. **23**: p. 231-237.

27. Coffin, L. *The problem of thermal stress fatigue in austenitic steels at elevated temperatures*. in *Symposium on Effect of Cyclic Heating and Stressing on Metals at Elevated Temperatures*. 1954. ASTM International.

28. Manson, S., *Strain controlled low cycle fatigue of metals.* NASA Technical Note, 1954. **2933**: p. 2933.

29. Wang, Q., et al., *Technical note High-cycle fatigue crack initiation and propagation behaviour of high-strength sprin steel wires.* Fatigue & Fracture of Engineering Materials & Structures, 1999. **22**(8): p. 673-677.

30. Christ, H.-J., et al., *Propagation behaviour of microstructural short fatigue cracks in the high-cycle fatigue regime.* Computational Materials Science, 2009. **46**(3): p. 561-565.

31. Chan, K., J. Lankford, and D. Davidson, *A comparison of crack-tip field parameters for large and small fatigue cracks.* Jurnal of Engineering Materials and Technology JULY, 1986. **108**: p. 207.

32. McDowell, D.L. and J.Y. Berard, *A δJ-BASED APPROACH TO BIAXIAL FATIGUE.* Fatigue & Fracture of Engineering Materials & Structures, 1992. **15**(8): p. 719-741.

33. Socie, D. and G. Marquis, *Multiaxial fatigue.* Warrendale, PA: Society of Automotive Engineers, 1999. 502, 1999.

34. Brown, M. and K. Miller, *A theory for fatigue failure under multiaxial stress-strain conditions.* Proceedings of the Institution of Mechanical Engineers, 1973. **187**(1): p. 745-755.

35. Fatemi, A. and D.F. Socie, *A Critical Plane Approach to Multiaxial Fatigue Damage Including out-of-Phase Loading.* Fatigue & Fracture of Engineering Materials & Structures, 1988. **11**(3): p. 149-165.

36. McDowell, D.L., *Simulation-based strategies for microstructure-sensitive fatigue modeling.* Materials Science and Engineering: A, 2007. **468**: p. 4-14.

37. McDowell, D. and F. Dunne, *Microstructure-sensitive computational modeling of fatigue crack formation.* International journal of fatigue, 2010. **32**(9): p. 1521-1542.

38. Przybyla, C., et al., *Microstructure-sensitive modeling of high cycle fatigue.* International Journal of Fatigue, 2010. **32**(3): p. 512-525.

39. Przybyla, C.P. and D.L. McDowell, *Simulated microstructure-sensitive extreme value probabilities for high cycle fatigue of duplex Ti-6Al-4V.* International Journal of Plasticity, 2011. **27**: p. 1871-1895.

40. Castelluccio, G.M. and D.L. McDowell, *A mesoscale approach for growth of 3D microstructurally small fatigue cracks in polycrystals.* International Journal of Damage Mechanics, 2014. **23**(6): p. 791-818.

41. Tanaka, K. and T. Mura, *A dislocation model for fatigue crack initiation.* Journal of Applied Mechanics, 1981. **48**(1): p. 97-103.

42. Chan, K.S., *A microstructure-based fatigue-crack-initiation model.* Metallurgical and Materials Transactions A, 2003. **34**(1): p. 43-58.

43. Shenoy, M., J. Zhang, and D. McDowell, *Estimating fatigue sensitivity to polycrystalline Ni-base superalloy microstructures using*

a computational approach. Fatigue & Fracture of Engineering Materials & Structures, 2007. **30**(10): p. 889-904.

44. Hochhalter, J., et al., *A geometric approach to modeling microstructurally small fatigue crack formation: II. Physically based modeling of microstructure-dependent slip localization and actuation of the crack nucleation mechanism in AA 7075-T651.* Modelling and Simulation in Materials Science and Engineering, 2010. **18**(4): p. 045004.

45. Hochhalter, J., et al., *A geometric approach to modeling microstructurally small fatigue crack formation: III. Development of a semi-empirical model for nucleation.* Modelling and Simulation in Materials Science and Engineering, 2011. **19**(3): p. 035008.

46. Castelluccio, G.M. and D.L. McDowell, *Assessment of small fatigue crack growth driving forces in single crystals with and without slip bands.* International journal of fracture, 2012. **176**(1): p. 49-64.

47. Castelluccio, G.M. and D.L. McDowell, *Mesoscale modeling of microstructurally small fatigue cracks in metallic polycrystals.* Materials Science and Engineering: A, 2014. **598**: p. 34-55.

48. Hennessey, C., *Modeling microstructurally small crack growth in Al 7075-T6*, in *Mechanical Engineering*. 2015, Georgia Institute of Technology.

49. Musinski, W.D., *Modeling the effects of shot-peened residual stresses and inclusions on microstructure-sensitive fatigue of NI-base superalloy components*, in *George W. Woodruff School of Mechanical Engineering*. 2014, Georgia Institute of Technology.

50. Rovinelli, A., R.A. Lebensohn, and M.D. Sangid, *Influence of microstructure variability on short crack behavior through postulated micromechanical short crack driving force metrics.* Engineering Fracture Mechanics, 2015. **138**: p. 265-288.

51. Dowling, N. and J. Begley, *Fatigue crack growth during gross plasticity and the J-integral*, in *Mechanics of crack growth*. 1976, ASTM International.

52. Cisilino, A. and M. Aliabadi, *Three-dimensional boundary element analysis of fatigue crack growth in linear and non-linear fracture problems.* Engineering Fracture Mechanics, 1999. **63**(6): p. 713-733.

53. Pugno, N., et al., *A generalized Paris' law for fatigue crack growth.* Journal of the Mechanics and Physics of Solids, 2006. **54**(7): p. 1333-1349.

54. Beretta, S., A. Ghidini, and F. Lombardo, *Fracture mechanics and scale effects in the fatigue of railway axles.* Engineering fracture mechanics, 2005. **72**(2): p. 195-208.

55. Paris, P.C., M.P. Gomez, and W.E. Anderson, *A rational analytic theory of fatigue.* The trend in engineering, 1961. **13**(1): p. 9-14.

56. McDowell, D.L., *A perspective on trends in multiscale plasticity.* International Journal of Plasticity, 2010. **26**(9): p. 1280-1309.

57. McGinty, R. and D. McDowell, *A semi-implicit integration scheme for rate independent finite crystal plasticity.* International Journal of Plasticity, 2006. **22**(6): p. 996-1025.

58. McGinty, R.D. and D.L. McDowell, *Application of multiscale crystal plasticity models to forming limit diagrams.* Journal of engineering materials and technology, 2004. **126**(3): p. 285-291.

59. Diard, O., et al., *Evaluation of finite element based analysis of 3D multicrystalline aggregates plasticity: Application to crystal plasticity model identification and the study of stress and strain fields near grain boundaries.* International Journal of Plasticity, 2005. **21**(4): p. 691-722.

60. Przybyla, C.P. and D.L. McDowell, *Microstructure-sensitive extreme value probabilities for high cycle fatigue of Ni-base superalloy IN100.* International Journal of Plasticity, 2010. **26**: p. 372-394.

61. Dixit, P.M.D., U.S., *Plasticity: Fundamentals and Applications*. 2014: CRC Press.

62. Bilby, B., L. Gardner, and A. Stroh, *Continuous distributions of dislocations and the theory of plasticity.* IXe Congrès International de Mécanique Appliquée, III. Bruxelles, Berlgique, 1957: p. 35-44.

63. Lee, E.H., *Elastic-plastic deformation at finite strains.* Journal of Applied Mechanics, 1969. **36**(1): p. 1-6.

64. Przybyla, C.P., *Microstructure-sensitive extreme value probabilities of fatigue in advanced engineering alloys*, in *PhD Thesis*. 2010, Georgia Institute of Technology: Atlanta, GA, USA.

65. Asaro, R.J., *Micromechanics of Crystals and Polycrystals.* Advances in Applied Mechanics, 1983. **23**: p. 1-115.

66. Soh, A.K., *Development of special multi-material elements.* International journal of solids and structures, 2000. **37**(6): p. 899-918.

67. Barbe, F., et al., *Intergranular and intragranular behavior of polycrystalline aggregates. Part 1: FE model.* International journal of plasticity, 2001. **17**(4): p. 513-536.

68. Heripre, E., et al., *Coupling between experimental measurements and polycrystal finite element calculations for micromechanical study of metallic materials.* International Journal of Plasticity, 2007. **23**(9): p. 1512-1539.

69. Adams, B.L., X.C. Gao, and S.R. Kalidindi, *Finite approximations to the second-order properties closure in single phase polycrystals.* Acta Materialia, 2005. **53**(13): p. 3563-3577.

70. Niezgoda, S.R., et al., *Optimized structure based representative volume element sets reflecting the ensemble-averaged 2-point statistics.* Acta Materialia, 2010. **58**(13): p. 4432-4445.

71. Niezgoda, S., D. Fullwood, and S. Kalidindi, *Delineation of the space of 2-point correlations in a composite material system.* Acta Materialia, 2008. **56**(18): p. 5285-5292.

72. Binci, M., D. Fullwood, and S.R. Kalidindi, *A new spectral framework for establishing localization relationships for elastic behavior of composites and their calibration to finite-element models.* Acta Materialia, 2008. **56**(10): p. 2272-2282.

73. Torquato, S., *Random heterogeneous materials: microstructure and macroscopic properties*. Vol. 16. 2013: Springer Science & Business Media.

74. Hill, R., *Elastic properties of reinforced solids: some theoretical principles.* Journal of the Mechanics and Physics of Solids, 1963. **11**(5): p. 357-372.

75. Lacy, T.E., D.L. McDowell, and R. Talreja, *Gradient concepts for evolution of damage.* Mechanics of Materials, 1999. **31**(12): p. 831-860.

76. Gitman, I., H. Askes, and L. Sluys, *Representative volume: existence and size determination.* Engineering fracture mechanics, 2007. **74**(16): p. 2518-2534.

77. Ostoja-Starzewski, M., *Material spatial randomness: From statistical to representative volume element.* Probabilistic engineering mechanics, 2006. **21**(2): p. 112-132.

78. Trias, D., et al., *Determination of the critical size of a statistical representative volume element (SRVE) for carbon reinforced polymers.* Acta Materialia, 2006. **54**(13): p. 3471-3484.

79. Przybyla, C.P., et al., *Microstructure-sensitive HCF and VHCF simulations.* International Journal of Fatigue, 2013. **57**: p. 9-27.

80. Zhao, T. and Y. Jiang, *Fatigue of 7075-T651 aluminum alloy.* International Journal of Fatigue, 2008. **30**(5): p. 834-849.

81. Li, Y., et al., *CAutoCSD-evolutionary search and optimisation enabled computer automated control system design.* International Journal of Automation and Computing, 2004. **1**(1): p. 76-88.

82. Kamentsky, L. and C. Liu, *Computer-automated design of multifont print recognition logic.* IBM Journal of Research and Development, 1963. **7**(1): p. 2-13.

83. Brncick, M., *Computer automated design and computer automated manufacture.* Physical medicine and rehabilitation clinics of North America, 2000. **11**(3): p. 701-713.

84. Holdren, J.P., *Materials genome initiative for global competitiveness.* National Science and Technology Council OSTP. Washington, USA, 2011.

85. Jain, A., et al., *Commentary: The Materials Project: A materials genome approach to accelerating materials innovation.* Apl Materials, 2013. **1**(1): p. 011002.

86. Van Rossum, G. and F.L. Drake Jr, *Python tutorial*. 1995: Centrum voor Wiskunde en Informatica Amsterdam, The Netherlands.

87. Rollett, A.D., R. Campman, and D. Saylor, *Three dimensional microstructures: statistical analysis of second phase particles in AA7075-T651.* Materials science forum, 2006. **519**: p. 1-10.

88. Uchic, M.D., *3-D microstructural characterization: Methods, analysis, and applications.* JOM Journal of the Minerals, Metals and Materials Society, 2006. **58**(12): p. 24-24.

89. Groeber, M., et al., *A framework for automated analysis and simulation of 3d polycrystalline microstructures.: Part 1: Statistical characterization.* Acta Materialia, 2008. **56**(6): p. 1257-1273.

90. Agnew, S., M. Yoo, and C. Tome, *Application of texture simulation to understanding mechanical behavior of Mg and solid solution alloys containing Li or Y.* Acta Materialia, 2001. **49**(20): p. 4277-4289.

91. Van Der Walt, S., S.C. Colbert, and G. Varoquaux, *The NumPy array: a structure for efficient numerical computation.* Computing in Science & Engineering, 2011. **13**(2): p. 22-30.

92. Groeber, M.A. and M.A. Jackson, *DREAM. 3D: a digital representation environment for the analysis of microstructure in 3D.* Integrating Materials and Manufacturing Innovation, 2014. **3**(1): p. 1-17.

93. Groeber, M., et al., *A framework for automated analysis and simulation of 3D polycrystalline microstructures. Part 2: Synthetic structure generation.* Acta Materialia, 2008. **56**(6): p. 1274-1287.

94. Rowenhorst, D., et al., *Tutorial: Consistent Representations of and Conversions Between 3D Rotations.*

95. *Abaqus Unified FEA*. 2015, Dassault Systemes.

96. Xia, Z., Y. Zhang, and F. Ellyin, *A unified periodical boundary conditions for representative volume elements of composites and*

applications. International Journal of Solids and Structures, 2003. **40**(8): p. 1907-1921.

97. Nguyen, V.-D., et al., *Imposing periodic boundary condition on arbitrary meshes by polynomial interpolation.* Computational Materials Science, 2012. **55**: p. 390-406.

98. Paramiko, *Native Python SSHv2 protocol library*. 2013.

99. Freudenthal, A.M. and E. Gumbel. *On the statistical interpretation of fatigue tests*. in *Proceedings of the Royal Society of London A: Mathematical, Physical and Engineering Sciences*. 1953. The Royal Society.

100. Evans, A., *The role of inclusions in the fracture of ceramic materials.* Journal of Materials Science, 1974. **9**(7): p. 1145-1152.

101. Castillo, E., et al., *A fatigue model with local sensitivity analysis.* Fatigue & Fracture of Engineering Materials & Structures, 2007. **30**(2): p. 149-168.

102. Murakami, Y., S. Kodama, and S. Konuma, *Quantitative evaluation of effects of non-metallic inclusions on fatigue strength of high strength steels. I: Basic fatigue mechanism and evaluation of correlation between the fatigue fracture stress and the size and location of non-metallic inclusions.* International Journal of Fatigue, 1989. **11**(5): p. 291-298.

103. DeBartolo, E. and B. Hillberry, *A model of initial flaw sizes in aluminum alloys.* International Journal of Fatigue, 2001. **23**: p. 79-86.

104. Beretta, S., C. Anderson, and Y. Murakami, *Extreme value models for the assessment of steels containing multiple types of inclusion.* Acta materialia, 2006. **54**(8): p. 2277-2289.

105. Marines, I., X. Bin, and C. Bathias, *An understanding of very high cycle fatigue of metals.* International Journal of fatigue, 2003. **25**(9): p. 1101-1107.

106. Gumbel, E., *Statistics of extremes. 1958.* Columbia Univ. press, New York, 1958.

107. Haldar, A. and S. Mahadevan, *Probability, Reliability and Statistical Methods in Engineering Design*. 2000, New York: John Wiley and Sons, Inc.

108. Przybyla, C.P. and D.L. McDowell, *Microstructure-sensitive extreme-value probabilities of high-cycle fatigue for surface vs. subsurface crack formation in duplex Ti-6Al-4V.* Acta Materialia, 2012. **60**: p. 293-305.

109. *MATLAB 2016a*. 2016, The MathWorks, Inc.: Natick, Massachusetts, United States.

110. Castelluccio, G.M. and D.L. McDowell, *Microstructure and mesh sensitivities of mesoscale surrogate driving force measures for transgranular fatigue cracks in polycrystals.* Materials Science and Engineering: A, 2015. **639**: p. 626-639.

111. Ostoja-Starzewski, M., P. Sheng, and I. Jasiuk, *Influence of random geometry on effective properties and damage formation in composite materials.* Journal of engineering materials and technology, 1994. **116**(3): p. 384-391.

112. Ostoja-Starzewski, M. and M.C. Wang, *Linear elasticity of planar Delaunay networks: random field characterization of effective moduli.* Acta Mechanica, 1989. **80**(1-2): p. 61-80.

113. Smith, B., D. Shih, and D. McDowell, *Cyclic Plasticity Experiments and Polycrystal Plasticity Modeling of Three Distinct Ti Alloy Microstructures.* International Journal of Plasticity, 2013.

114. Picek, J. and J. Dienstbier, *Tests for Gumbel domain of attraction based on regression quantiles.*

115. Wormsen, A., et al., *Non-local stress approach for fatigue assessment based on weakest-link theory and statistics of extremes.* Fatigue & Fracture of Engineering Materials & Structures, 2007. **30**(12): p. 1214-1227.

116. Yin, X., et al., *Statistical volume element method for predicting microstructure–constitutive property relations.* Computer methods in applied mechanics and engineering, 2008. **197**(43): p. 3516-3529.

117. Moriarty, P.J., W. Holley, and C.P. Butterfield, *Extrapolation of extreme and fatigue loads using probabilistic methods*. 2004: National Renewable Energy Laboratory.

118. Davis, J.R. and J.R. Davis, *Aluminum and aluminum alloys*. 1993: ASM international.

119. Ohno, N. and J.D. Wang, *Kinematic hardening rules with critical state of dynamic recovery, Part I: Formulation and basic features for ratchetting behavior*. International Journal of Plasticity, 1993. **9**: p. 375-390.

120. Xue, Y., et al., *Microstructure-based multistage fatigue modeling of aluminum alloy 7075-T651*. Engineering Fracture Mechanics, 2007. **74**(17): p. 2810-2823.

121. Singh, S.S., et al., *3D microstructural characterization and mechanical properties of constituent particles in Al 7075 alloys using X-ray synchrotron tomography and nanoindentation*. Journal of Alloys and Compounds, 2014. **602**: p. 163-174.

122. Alatorre, N., et al., *Tensile properties and fusion zone hardening for gmaw and miea welds of a 7075-T651 aluminum alloy*. Acta Metallurgica Sinica (English Letters), 2014. **27**(4): p. 694-704.

123. Kung, C. and M. Fine, *Fatigue crack initiation and microcrack growth in 2024-T4 and 2124-T4 aluminum alloys.* Metallurgical Transactions A, 1979. **10**(5): p. 603-610.

124. Wang, L., et al., *Three-dimensional finite element analysis using crystal plasticity for a parameter study of fatigue crack incubation in a 7075 aluminum alloy*. International Journal of Fatigue, 2009. **31**(4): p. 659-667.

125. Tokaji, K., T. Ogawa, and Y. Kameyama, *THE EFFECTS OF STRESS RATIO ON THE GROWTH BEHAVIOUR OF SMALL FATIGUE CRACKS IN AN ALUMINUM ALLOY 7075-T6 (WITH SPECIAL INTEREST IN STAGE I CRACK GROWTH).* Fatigue & Fracture of Engineering Materials & Structures, 1990. **13**(4): p. 411-421.

126. Lee, S.G., *Particle cracking and rotation during plastic deformation of 7075 aluminum alloy*. Metals and Materials International, 2009. **15**(4): p. 591-596.

127. Fedelich, B., *A stochastic theory for the problem of multiple surface crack coalescence*. International Journal of Fracture, 1998. **91**(1): p. 23-45.

128. McDowell, D., et al., *Microstructure-based fatigue modeling of cast A356-T6 alloy*. Engineering Fracture Mechanics, 2003. **70**(1): p. 49-80.

129. Künkler, B., et al. *4476-SHORT CRACK PROPAGATION IN DUPLEX STEEL–MODELLING AND EXPERIMENTAL VERIFICATION*. in *ICF11, Italy 2005*. 2013.

130. Donnelly, E. and D. Nelson, *A study of small crack growth in aluminum alloy 7075-T6.* International journal of fatigue, 2002. **24**(11): p. 1175-1189.

131. Zurek, A., M. James, and W. Morris, *The effect of grain size on fatigue growth of short cracks.* Metallurgical Transactions A, 1983. **14**(8): p. 1697-1705.

132. Tokaji, K., T. Ogawa, and Y. Kameyama, *The effects of stress ratio on the growth behavior of small fatigue cracks in aluminum alloy 7075-T6 (with special interest in stage I crack growth).* Fatigue & Fracture of Engineering Materials & Structures, 1990. **13**(4): p. 411-421.

133. Zhai, T., A. Wilkinson, and J. Martin, *A crystallographic mechanism for fatigue crack propagation through grain boundaries.* Acta materialia, 2000. **48**(20): p. 4917-4927.

134. Turkmen, H.S., et al., *On the mechanical behaviour of AA 7075-T6 during cyclic loading.* International Journal of fatigue, 2003. **25**(4): p. 267-281.

135. Ramesh Narayanan, P., et al. *Evolution of Crystallographic Texture in Cold Rolled Al-Zn-Mg Alloys Used in Space Applications*. in *Materials Science Forum*. 2012. Trans Tech Publ.

136. Turner, D.M. and S.R. Kalidindi, *Statistical construction of 3-D microstructures from 2-D exemplars collected on oblique sections.* Acta Materialia, 2016. **102**: p. 136-148.

137. Bannantine, J.C., J; Handrock, J., *Fundamentals of Metal Fatigue Analysis*. 1990, Englewood Cliffs, New Jersey 07632: Prentice Hall.

138. Pedregosa, F., et al., *Scikit-learn: Machine Learning in Python.* Journal of Machine Learning Research, 2011. **12**: p. 2825-2830.

139. Fabian Pedregosa, G.V., Alexandre Gramfort, Vincent Michel, Bertrand Thirion, Olivier Grisel, Mathieu Blondel, Peter Prettenhofer, Ron Weiss, Vincent Dubourg, Jake Vanderplas, Alexandre Passos, David Cournapeau, Matthieu Brucher, Matthieu Perrot, Édouard Duchesnay, *Scikit-learn: Machine Learning in Python.* JMLR, 2011. **12**: p. 2825-2830.

140. Butzke, J. and S. Bargmann, *Thermomechanical modelling of polysynthetically twinned TiAl crystals.* Philosophical Magazine, 2015. **95**(24): p. 2607-2626.

141. Choi, H.-J., et al. *An inductive design exploration method for the integrated design of multi-scale materials and products*. in *ASME 2005 International Design Engineering Technical Conferences and Computers and Information in Engineering Conference*. 2005. American Society of Mechanical Engineers.